

## ABSTRACT

Title of Dissertation: NOVEL APPROACHES TO CONTROL  
SURFACE REACTIONS IN PLASMA  
ETCHING OF ELECTRONIC MATERIALS

Chen Li, Doctor of Philosophy, 2019

Dissertation directed by: Professor Gottlieb S. Oehrlein, Department of  
Physics, Department of Material Science and  
Engineering and Institute  
for Research in Electronics and Applied Physics

Advanced semiconductor manufacturing requires precise plasma etching control for patterning complex semiconductor device structures. Pattern transfer into dielectric materials is one of the most frequently performed operation and traditionally done using continuous wave (CW) plasma etching processes based on fluorocarbon (FC) chemistries. Such etching methods are facing challenges when the critical dimension (CD) approach 10 nm. Issues include low materials etching selectivity, surface damage, roughness, and poor etching profile control. In this work, various aspects of low temperature plasma-based etching approaches are tailored for optimal plasma etching performance, including novel gaseous precursors for better control of gas phase and surface processes, tailoring the relative importance of radicals and ion bombardment at surface by sequential processes, and a new way to input energy to surfaces to stimulate etching reactions. We systematically studied the impact of molecular structure parameters of hydrofluorocarbon (HFC) precursors on plasma deposition of fluorocarbon (FC) and material

etching performance. The HFC chemical composition and molecular structure such as ring structure, C=C, C≡C, C-O, C-H and degree of unsaturation have dramatic impacts on FC surface polymerization and material etching performance. Further, we report a new atomic layer etching (ALE) technique which temporally separates chemical reactant supply to a surface from ion bombardment induced etching. By this ALE method, the ion bombardment energy can be reduced to ensure low substrate damage and extremely high etching selectivity of two materials. Finally, we developed a hollow cathode electron beam etching system to reduce the energy and momentum input on the material surface by utilizing an electron-radical synergy effect. This present work has unveiled highly promising elements of a new roadmap of next generation semiconductor etching approaches and is expected to impact multiple areas of nanoscience and technology, including plasma etching of post-silicon materials. The use of specially selected gaseous precursor chemistry, temporal separation of radical exposure and energy-induced etching, and finally using electron bombardment for activation of surface etching, challenge our current understanding of semiconductor plasma processing and presents an important step forward in terms of the further industrial development of these approaches.

NOVEL APPROACHES TO CONTROL SURFACE REACTIONS IN PLASMA ETCHING  
OF ELECTRONIC MATERIALS

by

Chen Li

Dissertation submitted to the Faculty of the Graduate School of the  
University of Maryland, College Park, in partial fulfillment  
of the requirements for the degree of  
Doctor of Philosophy  
2019

Advisory Committee:

Professor Gottlieb S. Oehrlein, Chair  
Professor Steven Anlage  
Professor William Dorland  
Professor Derek Boyd  
Professor Thomas Antonsen

© Copyright by  
Chen Li  
2019

## Acknowledgements

It is a long time to the end of the PhD studies. First, I would like to thank my advisor, Prof. Gottlieb Oehrlein for the constant patience, guidance, and encouragement through my PhD period. Those help is crucial to this thesis. I would like to thank you for developing my creative thinking and scientific research ability. I also thank for the great opportunities to interact with scientists in academia and industry.

I would like to thank my dissertation committee for showing interest in my work and reading my dissertation. Prof. Anlage, Prof. Dorland, Prof. Boyd, and Prof. Antonsen – Thank you.

Also, I would like to thank my collaborators at Air Liquide, Lam Research, IBM, Global Foundries, and Carl Zeiss. The projects work together were always promising and challenging. Special thanks to Prof. Valery Godyak, who is always patient to explain the basis of the probe measurement problems.

Thank you to my current and former laboratory colleagues and friends – Dr. Nick Fox-Lyon, Dr. Elliot Bartis, Dr. Dominik Metzler, Dr. Andrew Knoll, Dr. Pingshan Luan, Adam Pranda, Kang-Yi Lin, and Yudong Li. Thank you for the help for complete my research and being my closest friends.

I would like to thank my parents, who always are supportive and patient. I will always be grateful for the educational foundation you provided.

## Table of Contents

Acknowledgements.....	ii
List of Tables .....	v
List of Figures.....	vi
Chapter 1: Introduction.....	1
1.1 Advanced Semiconductor Device Processing .....	1
1.2 Collaborative Research.....	4
1.3 Plasma Processing.....	5
1.4 Brief Description of Materials Used.....	8
1.5. Characterization Techniques.....	8
Ellipsometry.....	9
X-ray Photoelectron Spectroscopy (XPS) .....	9
Optical emission spectrometer.....	10
Langmuir Probe .....	10
1.6 Thesis Outline.....	10
Chapter 2: Impact of Hydrofluorocarbon Molecular Structure Parameters on Plasma Etching of Ultra-Low-K Dielectric.....	13
2.1 INTRODUCTION .....	16
2.1 EXPERIMENT .....	17
2.1.1 Description of material and precursor gases.....	17
2.1.2 The dual frequency capacitively coupled plasma reactor and processing conditions .	19
2.1.3 Surface and Optical Characterizations.....	21
2.2 RESULTS AND DISCUSSION.....	22
2.2.1 Correlations of CF <sub>2</sub> emission, fluorocarbon deposition rate, and surface chemistry of hydrofluorocarbon based plasma.....	22
2.2.2 BDII etching rate and selectivity dependence of precursor.....	34
2.2.3 Low-k sidewall O <sub>2</sub> protection dependence of Precursor.....	38
2.3 SUMMARY AND CONCLUSIONS .....	41
ACKNOWLEDGMENTS .....	42
Chapter 3: Fluorocarbon Based Atomic Layer Etching of Si <sub>3</sub> N <sub>4</sub> and Etching Selectivity of SiO <sub>2</sub> over Si <sub>3</sub> N <sub>4</sub> .....	43
3.1 INTRODUCTION .....	45
3.2 EXPERIMENTAL.....	46
3.3 RESULTS AND DISCUSSION.....	49
3.3.1 Continuous wave (CW) plasma etching and ellipsometry optical model of Si <sub>3</sub> N <sub>4</sub> stack sample.....	49
3.3.2 Si <sub>3</sub> N <sub>4</sub> ALE in FC depleted condition.....	51
3.3.3 SiO <sub>2</sub> to Si <sub>3</sub> N <sub>4</sub> selectivity optimization by FC accumulated conditions.....	54
3.3.4 Surface chemistry evaluation.....	68
3.4 SUMMARY AND CONCLUSIONS .....	78
ACKNOWLEDGMENTS .....	79
Chapter 4: Hollow Cathode Plasma Electron Beam Secondary Plasma Production and Etching of Si <sub>3</sub> N <sub>4</sub> and Polycrystalline Si.....	80
4.1 INTRODUCTION .....	82

4.2 EXPERIMENTAL .....	85
4.3 RESULTS AND DISCUSSION .....	89
4.3.1 Parametric studies of hollow cathode EB source.....	89
4.3.2 Langmuir probe measurement of hollow cathode EB .....	93
4.3.3 Characterization of the combination of remote plasma radical source together with hollow cathode electron beam source .....	101
4.4 SUMMARY AND CONCLUSIONS .....	105
ACKNOWLEDGMENTS .....	106
Chapter 5: Investigation of Hollow Cathode Plasma Electron Beam Etching of Si <sub>3</sub> N <sub>4</sub> .....	107
5.1 INTRODUCTION .....	109
5.2 EXPERIMENTAL .....	110
5.3 RESULTS AND DISCUSSION .....	112
5.3.1 Impact of precursor composition on remote plasma etching.....	112
5.3.2 Hollow cathode plasma-electron beam induced etching .....	117
5.3.3 Discharge current, pressure, distance impacts on HC EB enhanced Si <sub>3</sub> N <sub>4</sub> etching...	121
5.4 Process conditions suitable for EB controlled Si <sub>3</sub> N <sub>4</sub> etching.....	125
5.5 SUMMARY AND CONCLUSIONS .....	128
ACKNOWLEDGMENTS .....	129
Chapter 6: Conclusions and Future work.....	131
References.....	135

## List of Tables

Table 1.1: Organization of collaborations in this dissertation

Table 2.1: Precursor gas chemical structures,  $\text{CF}_2$  fraction in gas structure, and degree of unsaturation (DU) for the precursors studied in this work.

Table 2.2: Bond Energies

## List of Figures

FIG. 2.1 (Color online) Overview of FC deposition process. Precursor weak bonds will preferentially break and provide sites for polymerization. On the other hand, energetic ions will be accelerated and bombard on FC surface, inducing etching and damage to FC film structure.

FIG. 2.2 (Color online)  $\text{CF}_2$  optical emission and deposited film surface  $\text{CF}_2$  intensity vs.  $\text{CF}_2$  fraction ( $\text{CF}_2$  number /C number) in gas structure. Isomer pairs are in the color of red, green, and blue.  $\text{CF}_2$  emission intensity has good correlation to gas structure, while the surface  $\text{CF}_2$  is not.

FIG. 2.3 (Color online) High resolution C 1s XPS spectra of deposited film of  $\text{C}_4\text{F}_6$  isomers with differential spectra (panel a). Peak assignments are indicated at the top of the spectra. Precursor gas structures are shown at panel b. With ion bombardment, crosslinking degree is high for the deposited film. Surface chemistry has a weak memory from the gas structure.

FIG. 2.4 (Color online)  $\text{CF}_2$  optical emission and deposited film surface  $\text{CF}_2$  intensity vs. deposition rate. High deposition rate gas minimizes ion bombardment modification of the surface. Precursor gases with different deposition rate is separated by degree of unsaturation ( $\text{DU} = \text{Ring} + \text{C}=\text{C} + 2 \times \text{C}\equiv\text{C}$ ). Isomer pairs are in the color of red, green, and blue.

FIG. 2.5 (Color online) Surface  $\text{CF}_2$  vs. normalized product of deposition rate (DR) and  $\text{CF}_2$  fraction in precursor. No  $\text{CF}_2$  gases can also have  $\text{CF}_2$  bond on the surface.

FIG. 2.6 (Color online) Correlation between deposition rate and deposited FC film crosslinking degree and F/C ratio, characterized by XPS C1s high resolution scan ( $\text{Crosslink} = \text{C-C} \% + \text{C-CF}_x \% + \text{C-F} \%$ ,  $\text{F/C} = \text{C-F} \% + 2*\text{C-F}_2 \% + 3*\text{C-F}_3 \%$ , each peak intensity percentage is calculated by total carbon area). Hydrogen containing gases show strongly interaction with F, leaving a low F/C and highly crosslinked film.

FIG. 2.7 (Color online) Selected precursor deposition rate dependence of logarithm of gas phase  $\text{CF}_2$  optical emission intensity.

FIG. 2.8 (Color online) Deposition rate vs. precursor gas available dangling bond number after low binding energy bonds broken. Gas structures are shown next to the data.

FIG. 2.9 (Color online) BDII and aC etch rate vs. precursor deposition rate. High deposition rate precursor shows low etch rate.

FIG. 2.10 (Color online) BDII etch rate and BDII/aC selectivity vs. precursor reduced F/C ratio. Low reduced F/C ratio gases show high selectivity.

FIG. 2.11 (Color online) BDII ER (perpendicular bar), BDII/aC selectivity (horizontal bar), and the product of ER and selectivity (rectangular area) are shown in the precursor property (reduced F/C vs. DR) map.

FIG. 2.12 (Color online) *In situ* ellipsometric measurements of BDII simulated sidewall modification with: a)  $\text{O}_2$  plasma, b)  $\text{Ar}/\text{cC}_4\text{F}_8/\text{O}_2$  plasma, and c)  $\text{Ar}/\text{C}_4\text{F}_6\_DB/\text{O}_2$  plasma. Ellipsometric models with different refractive indices are also shown.

FIG. 2.13 (Color online) Delta changed of simulated BDII sidewall ellipsometry data at 600 s vs. precursor deposition rate.

FIG. 3.1 (Color online) Experimental sequence schematic for FC based ALE. The ALE experiment was conducting with a continuous Ar plasma and repeating ALE cycles. One ALE cycle includes an unbiased deposition step and a low energy ion bombardment etching step. A short precursor injection occurs at the beginning of each deposition step. The injection time was varied in order to achieve the desired FC deposition thickness. The duration of the etching step is referred to as etching step length.

FIG. 3.2 (Color online) Exemplary ellipsometry trajectory for a  $\text{Si}_3\text{N}_4$  stack sample, using an Ar/ $\text{C}_4\text{F}_8$  CW plasma etch. Colored, dashed lines show the optical model simulation.

FIG. 3.3 (Color online) Thickness changes of  $\text{Si}_3\text{N}_4$  and  $\text{SiO}_2$  during a single cycle for a 4 Å FC deposition, 25 eV maximum ion energy and 40 s etching step length. The precursor pulse is injected at the beginning of the deposition step. Twelve seconds after the pulse ends, the bias potential is applied marking the beginning of the etching step. Etch rates reduce during etching step due to FC depletion.

FIG. 3.4 (Color online) (a) Thickness etched per cycle for  $\text{Si}_3\text{N}_4$  and  $\text{SiO}_2$  as a function of maximum ion energy and FC thickness. (b)  $\text{SiO}_2$  to  $\text{Si}_3\text{N}_4$  selectivity, calculated by the thickness etched ratio in one cycle. In FC depleted conditions (25 and 30 eV), a higher maximum ion energy and thicker FC thickness enables more material etching. In FC accumulation conditions (20 eV), a thicker FC film reduces  $\text{Si}_3\text{N}_4$  etching, while  $\text{SiO}_2$  etching is enhanced.

FIG. 3.5 (Color online) Schematics illustrating (a) FC depleted conditions, which allows  $\text{Si}_3\text{N}_4$  to  $\text{SiO}_2$  etching selectivity, and (b) FC accumulation conditions, in which  $\text{SiO}_2$  to  $\text{Si}_3\text{N}_4$  etching selectivity can be achieved.

FIG. 3.6 (Color online) Maximum ion energy impact on  $\text{Si}_3\text{N}_4$  ALE behaviors. (a) *in-situ* ellipsometry trajectory in Delta-Psi space. Maximum ion energy of 20 eV condition shows a strong deviation from  $\text{Si}_3\text{N}_4$  simulation line, which can be explained by FC accumulation on top of  $\text{Si}_3\text{N}_4$  surface. (b) Thickness changes of  $\text{Si}_3\text{N}_4$  during a single cycle for two maximum ion energies.

FIG. 3.7 (Color online) Etching step length impact on SiO<sub>2</sub> and Si<sub>3</sub>N<sub>4</sub> ALE using 25 eV maximum ion energy and 4 Å FC deposited per cycle by C<sub>4</sub>F<sub>8</sub>. The dependence of etching step length on (a) initial and final etch rates during one cycle, (b) thickness etched per cycle, and (c) SiO<sub>2</sub> to Si<sub>3</sub>N<sub>4</sub> selectivity, calculated by the thickness etched ratio in one cycle, is shown.

FIG. 3.8. (Color online) FC thickness impact on SiO<sub>2</sub> and Si<sub>3</sub>N<sub>4</sub> ALE in the condition of 35 eV maximum ion energy and 20 s ESL using C<sub>4</sub>F<sub>8</sub>. (a) Initial and final ERs during one cycle. (b) Thickness etched per cycle. (c) SiO<sub>2</sub> to Si<sub>3</sub>N<sub>4</sub> selectivity, calculated by the thickness etched ratio in one cycle.

FIG. 3.9. (Color online) *In-situ* ellipsometry trajectory in Delta-Psi space for the condition of 35 eV maximum ion energy and 20 s ESL, with different thicknesses of deposited FC layer achieved by changing the C<sub>4</sub>F<sub>8</sub> pulse time from 1.6 s to 2.3 s. The Ar/CF<sub>4</sub> CW plasma etching trajectory is shown for reference of a sample without FC. In the case of 11.5 Å FC deposited per cycle, etching slows down at the SiO<sub>2</sub>-Si<sub>3</sub>N<sub>4</sub> interface and a FC film starts accumulating.

FIG. 3.10. (Color online) C<sub>4</sub>F<sub>8</sub> and CHF<sub>3</sub> comparison on SiO<sub>2</sub> to Si<sub>3</sub>N<sub>4</sub> ALE selectivity for FC depleted conditions and accumulation conditions.

FIG. 3.11. (Color online) ALE cycle averaged etch yield as a function of fluorine per incident ion averaged over the same cycle for (a) C<sub>4</sub>F<sub>8</sub> and (b) CHF<sub>3</sub> precursor gases in the condition of 20 to 35 eV ion energies, 20 to 60 s ESLs, and 2 to 11 Å FC film thicknesses. FC accumulation conditions are marked, and shown with a low cycle averaged etch yield in high F/Ar<sup>+</sup> region.

FIG. 3.12. (Color online) 90° Si<sub>3</sub>N<sub>4</sub> XPS of Si2p (a), C1s (b), N1s (c), O1s (d) and F1s (e) spectra scanned at the end of deposition step with 25 eV maximum ion energy, 40 s ESL and 4 Å FC deposited per cycle by C<sub>4</sub>F<sub>8</sub>. The deconvolution is shown for each spectrum. The areas for each moiety are kept consistent across all spectra.

FIG. 3.13. (Color online) Total negative valence number (2a+3b+y) evolution of SiO<sub>a</sub>N<sub>b</sub>F<sub>y</sub> layer during one ALE cycle for both C<sub>4</sub>F<sub>8</sub> and CHF<sub>3</sub> based FC depleted conditions in two probing angle.

FIG. 3.14. (Color online) Surface chemistry evolution of  $\text{Si}_3\text{N}_4$  surfaces during one ALE cycle for FC depleted conditions. (a) AR-XPS FC film thickness evolution, as calculated by  $\text{Si}2p$  signal attenuation for  $90^\circ$  and  $20^\circ$  electron take-off angles. The individual decomposed peak intensities of  $\text{F}1s$  spectra are shown for (b)  $\text{C}_4\text{F}_8$  and (c)  $\text{CHF}_3$ . The surface fluorine is transferred from a FC film into the substrate.

FIG. 3.15. (Color online) Comparison of FC thickness determined by AR-XPS calculation and overlayer thickness change determined by ellipsometry. Thickness increases after precursor injection obtained by these two methods are consistent with each other. After etching step, the AR-XPS FC thickness goes back to the initial value, while the overlayer thickness drops about  $4 \text{ \AA}$  lower than the initial value indicating substrate material etching.

FIG. 3.16. (Color online)  $20^\circ$   $\text{C}1s$  spectra of  $\text{Si}_3\text{N}_4$  surfaces scanned at the end of etching step with the condition of  $25 \text{ eV}$  maximum ion energy and  $4 \text{ \AA}$  FC per cycle deposited by  $\text{C}_4\text{F}_8$ . Etching step lengths (ESL) of (a)  $40 \text{ s}$  and (b)  $20 \text{ s}$  are shown, representing FC depleted and accumulation conditions, respectively.

FIG. 3.17. (Color online) AR-XPS FC thickness at the end of etching step as a function of ESL on  $\text{Si}_3\text{N}_4$  surface with the condition of  $25 \text{ eV}$  maximum ion energy and  $4 \text{ \AA}$  FC per cycle deposited by  $\text{C}_4\text{F}_8$ . Each data point represents one experiment with a specific ESL at the end of etching step on  $\text{Si}_3\text{N}_4$ .  $20 \text{ s}$  ESL shows an accumulation of FC on the  $\text{Si}_3\text{N}_4$  surface.

FIG. 4.1 (Color online) (a) Schematic overview of the experimental layout of the multi-chamber tool and (b) notations of currents and voltages of the electrical setup. In (c) a photograph of the setup when used with an Ar EB is shown.

FIG. 4.2 (Color online) Electrical current and optical emission characterization of the EB source/main chamber setup are shown as a function of extraction voltage,  $V_E$ . (a) Measurement of emission current  $I_E$ , acceleration plate current  $I_A$  and net measured substrate current  $I_B$  with varying extraction voltage  $V_E$ . (b) Corresponding behavior of optical emission intensity of Ar I (750.39 nm) and Ar II (472.69 nm) versus  $V_E$ .

FIG. 4.3 (Color online) Measurement of extraction current  $I_E$ , acceleration plate current  $I_A$  and net measured substrate current  $I_B$  with varying (a) discharge current  $I_D$ , (b) process chamber pressure and (c) distance at 2 mTorr (solid) and 10 mTorr (open) at 50 V extraction voltage.

FIG. 4.4 (Color online) Electron energy probability function (EEPF) measured by Langmuir probe for Ar EB with varying (a) extraction voltage  $V_E$ , (b) discharge current  $I_D$ , and (c) pressure. The EEPF of EB generated plasma consists with two major peaks separated by energy.

FIG. 4.5 (Color online) Electron temperature ( $T_e$ ) and electron density ( $n_e$ ) calculated for the low electron energy portion of EEPF measured by Langmuir probe for Ar EB with varying (a) extraction voltage  $V_E$ , (b) discharge current  $I_D$ , and (c) pressure.

FIG. 4.6. (Color online) Beam electron peak energy vs extraction voltage  $V_E$  with reference to  $V_E$  and  $V_E+V_D$  (a). The EEPF areas for both peaks vs extraction voltage  $V_E$  (b).

FIG. 4.7. (Color online) The EEPF area for three energy ranges vs  $I_D$  (a) and area slope of increase for three energy ranges (b).

Fig. 4.8 (Color online) Electron energy probability function (EEPF) measured by Langmuir probe for different processing gas to Ar ratio at condition of 10 sccm Ar, CF<sub>4</sub>/O<sub>2</sub> (1/4 ratio), 1.5 A discharge current, 50 V extraction voltage, 3.5 mTorr processing pressure, 400 W ECWR source power, and 1.8 mT ECWR B-field.

FIG. 4.9 (Color online) EB activated  $\text{Si}_3\text{N}_4$  / poly-Si surface etching with  $\text{CF}_4/\text{O}_2$  remote plasma: (a) ER vs  $V_E$  (b) optical emission of F, Ar, O intensities.

FIG. 4.10 (Color online) (a) Lateral etched thickness profiles of  $\text{Si}_3\text{N}_4$  and Poly-Si due to EB induced surface etching versus position. The etching times are 7 min for  $\text{Si}_3\text{N}_4$  and 2 min for Poly-Si. (b) Normalized etched thickness distribution and electron saturation current measured with a Langmuir probe setup versus position. Optical photographs of etched sample surfaces showing etched thickness distribution by optical interference are shown on top.

FIG. 5.1 (Color online) (a) Schematic overview of the experimental layout of the multi-chamber tool and (b) notations of currents and voltages of the electrical setup.

FIG. 5.2 (Color online) ECWR remote plasma etching characterized by converting  $\text{Si}_3\text{N}_4$  etching rate into surface reacted F as a function of  $\text{O}_2$  to  $\text{CF}_4+\text{O}_2$  flow ratio. Ar emission (751 nm) is used to normalize optical emission intensities of F (703 nm) and O (777 nm) and these ratios are also shown. When  $\text{O}_2$  concentration is greater than 20%, surface passivation/oxidation suppressed the  $\text{Si}_3\text{N}_4$  surface reaction. At 80%  $\text{O}_2$  concentration,  $\text{Si}_3\text{N}_4$  etching has ceased even though there is still a small amount of gas phase F shown by the OES measurements.

FIG. 5.3 (Color online)  $\text{Si}_3\text{N}_4$  surface XPS data after processing using different  $\text{O}_2$  concentrations in the  $\text{CF}_4/\text{O}_2$  remote plasma. Data obtained with a pristine  $\text{Si}_3\text{N}_4$  surface with native oxide is also compared in 20-degree probe angle XPS spectra of (a) C1s (b) Si2p (c) N1s (d) O1s (e) F1s. With the addition of  $\text{O}_2$  in plasma, there is no surface carbon contamination. A SiOF layer was observed on top of  $\text{Si}_3\text{N}_4$  surface.

FIG. 5.4 (Color online)  $\text{Si}_3\text{N}_4$  remote plasma etch rate vs passivation layer thickness determined by angle resolved XPS.

FIG. 5.5 (Color online) Electron-beam activated  $\text{Si}_3\text{N}_4$  surface etching with  $\text{CF}_4/\text{O}_2$  remote plasma in two different gas ratios: (a) ER vs  $V_E$ . (b) Optical emission of Ar normalized F and O intensities.

FIG. 5.6 (Color online) Electron energy probability function (EPPF) measured by Langmuir probe for Ar EB in  $\text{CF}_4/\text{O}_2$  remote plasma condition with varying extraction voltage  $V_E$ . The EPPF of EB generated plasma consists of two major peaks, one of which changes strongly with  $V_E$ .

FIG. 5.7 (Color online) (a) Ar emission intensity and (b)  $\text{Si}_3\text{N}_4$  ER vs extraction voltage for different discharge current. (c) The corresponding ER vs Ar emission for selected  $V_E$ .

FIG. 5.8 (Color online) (a) Ar emission intensity and (b)  $\text{Si}_3\text{N}_4$  ER vs extraction voltage for different pressure.

FIG. 5.9 (Color online) (a) Ar emission intensity and (b) Si<sub>3</sub>N<sub>4</sub> ER vs extraction voltage for different EB source to sample distances.

FIG. 5.10 (Color online) Si<sub>3</sub>N<sub>4</sub> thickness time evolution before and after electron beam injection. No spontaneous etching is observed without electron beam. After applying an extraction voltage  $V_E=50$  V, Si<sub>3</sub>N<sub>4</sub> is etched by electron chemical synergy effect with a etch rate of 6.18 nm/min. In the inset an optical micrograph is shown that was obtained after extended etching and shows the localized etching effect.

FIG. 5.11 (Color online) Si<sub>3</sub>N<sub>4</sub> surface chemistry scanned by XPS under 80% O<sub>2</sub> concentration in CF<sub>4</sub>/O<sub>2</sub> remote plasma with (red) and without (black) EB activation in 90-degree probe angle XPS spectra of (a) C1s (b) Si2p (c) N1s (d) O1s (e) F1s.

# Chapter 1: Introduction

## 1.1 Advanced Semiconductor Device Processing

Advanced semiconductor manufacturing requires precise etching control in order to fabricate devices with nanometer critical dimensions (CD).<sup>1,1,1.2</sup> For instance, patterning dielectric materials requires low temperature plasma-based etching processes, which are traditionally performed using continuous wave (CW) plasma reactive ion etching (RIE) processes based on fluorocarbon (FC) chemistries. Such etching methods are facing challenges when CD approach 10 nm and issues included low etching selectivity, surface damage, roughness and poor etching profile control.<sup>1.3</sup> This RIE process is utilizing the synergy effect of chemical reaction and ion bombardment, which normally requires three aspects: 1, a FC precursor chemistry; 2, a CW plasma providing gas chemistry dissociation and energetic ion bombardment at same time; 3, using accelerated ion as energy input. Correspondingly, various aspects of low temperature plasma-based etching approaches need to be tailored for optimal plasma etching performance, including improved gaseous precursors for better gas chemistry radicals, tailoring the relative importance of radicals and ion bombardment at surface, and the selection of energy input to surfaces which can be achieved with either energetic ions and/or electrons.

The fluorocarbon (FC) precursor molecular structure has been shown to impact plasma processes and surface properties. Many mechanistic details by which fluorocarbon-based plasma etching and polymerization take place on surfaces have remained unclear. While fluorocarbon-based plasma deposition of thin films has been

related to  $\text{CF}_2$  radicals, large  $\text{C}_x\text{F}_y$  groups, hydrogen addition and ion bombardment, the understanding of the role of precursor molecular structure and composition for FC plasma production, plasma-surface interaction, and film formation on the substrate is still poor. Additionally, the impact of FC precursor molecular structure with regard to plasma etching performance and plasma surface interactions is still not well known. In this work, we have examined these aspects, and shown how judicious selection of the molecular structure of the FC precursor molecules can be employed to achieve extremely high materials etching selectivity.<sup>1,4</sup>

Recently, FC assisted atomic layer etching (ALE) has been shown to have potential in the application of etching Si based materials. Metzler *et al* experimentally realized self-limited  $\text{SiO}_2$  ALE in 2013 using a highly controllable Ar/ $\text{C}_4\text{F}_8$  inductively coupled plasma (ICP) system and validated these concepts using *in-situ* etching depth measurements.<sup>1,5, 1.14, 1.15</sup> This ALE method is based on temporal separation of chemical reactant supply and ion bombardment induced etching that takes place in two sequential steps. The ion bombardment energy is set to a value between the chemical enhanced etching energy threshold and physical sputtering energy threshold and enables to achieve self-limited etching. The ion energies required for ALE are much lower than the traditional CW plasma etching ion energies.<sup>1,3, 1.6, 1.7</sup> This reduces substrate damage and enables high materials etching selectivity. To expand this ALE of  $\text{SiO}_2$  to etching of Si and  $\text{Si}_3\text{N}_4$ , and selectivity optimization e.g.  $\text{SiO}_2$  over Si and  $\text{Si}_3\text{N}_4$  is of interest.<sup>1.17-1.19</sup>

However, this ALE method based on an inductively coupled plasma sources still faces difficulty when etching material with low physical sputtering threshold, e.g.

Si or SiGe, due to plasma potential limiting the lowest possible ion energy<sup>1.8</sup> and/or plasma chamber wall interactions<sup>1.9</sup>. The momentum transfer of ions causes damage and surface roughness to the etched material surface.<sup>1.10-1.12</sup> Moreover, the minimum ion bombardment energy is limited by the sheath potential (typically 15-20 eV for inductively couple plasma<sup>1.13</sup>), causing difficulties with respect to achieving material etching selectivity for materials with a low energy threshold for etching, such as Si or SiGe .

Electron-beam (EB) induced etching is a potential approach for such low damage selective etching applications. Similar to ion assisted etching, electron assisted gas surface interaction has also been discussed by Coburn and Winters as early as 1979, when they used electron-beam bombardment in conjunction with XeF<sub>2</sub> to etch Si<sub>3</sub>N<sub>4</sub>, SiO<sub>2</sub> and SiC surfaces<sup>1.14</sup>. The potential of utilizing plasma-produced EBs<sup>1.15</sup> injected into process chambers for direct control of surface processes has hardly been studied.

To understand and develop each of these three aspects in the plasma composition, in this work, we studied the plasma etching performance of several materials as we optimized FC precursor structure, the extended parameter range available in FC-based ion-based atomic layer etching approaches, and finally injection of an electron beam into the downstream process environment of a FC plasma for substrate etching.

The present work has unveiled highly promising elements of a new roadmap of next generation semiconductor etching approaches and is expected impact multiple areas of nanoscience and technology, including plasma etching of post-silicon

materials. The method of separately improving various essential aspects that ultimately dominate the performance of low temperature plasma-based materials etching approaches is excited to have impacts both in future semiconductor technology and other areas. The use of better selected gaseous precursor chemistry, temporal separation of radical exposure and energy-induced etching, and finally using electron bombardment for activation of surface etching, challenge our current understanding of semiconductor plasma processing and presents an important step forward in terms of the further industrial development of these approaches.

## **1.2 Collaborative Research**

This research was performed in a collaborative effort with several groups of experts in both academia and industry. A brief description is shown in Table 1.1.

There are several benefits to having industrial collaborators with regard this research work. The industrial collaborators with excellent experience provide the most critical industrial and practical guidance for the research direction. For our collaborations, we held monthly phone conferences to discuss the recent progress and challenges. Their expert feedback and research strategy maximized the importance of this work. Several unique industrial level samples such as sub-nanometer stacks of material were provided to ensure highest research productivity.

The Langmuir probe for electron beam studies were conducted in collaboration with Prof. Valery Godyak from the RF Plasma Consulting and University of Michigan, Ann Arbor. Prof. Valery Godyak is a leading expert on Langmuir probe measurements with dedicated equipment and expertise.

Table 1.1: Organization of collaborations in this dissertation

<b>Project Collaborator</b>	<b>Member</b>	<b>Project</b>
Air Liquide	R. Gupta, V. Pallem	Precursor structure studies for low-k etching
Lam Research	S. Lai, M. Danek, E. Hudson, A. Dulkan	Atomic layer etching of dielectric materials with high selectivity
IBM	D. Metzler, S. Engelmann, R. Bruce, E.A. Joseph	
GLOBALFOUNDRIES	C. Labelle, A. P. Labonte, C. Park, G. Beique	
Carl Zeiss, SMS	T. Hofmann, K. Edinger	Electron beam enhanced material etching
RF Plasma Consulting and University of Michigan, Ann Arbor	Prof. V. Godyak	

### 1.3 Plasma Processing

Plasma processing was performed in the Laboratory for Plasma Processing of Materials at the University of Maryland. Three different plasma processing systems were used for the three major research projects of this thesis. The precursor structure studies were performed using a custom-build dual frequency capacitively coupled plasma (CCP) system<sup>1,16</sup> which is very similar to the kind of plasma processing tool used industrially for plasma etching of dielectrics. This is described in detail in

chapter 2. Briefly, a pair of 5 inch diameter electrodes is located in the center of a stainless steel vacuum chamber with 10 inch diameter. The gap between the two electrodes is 50 mm. The top electrode features a showerhead design for gas distribution. The 13.56 MHz source power is using an L-type matching network configuration. The bottom electrode is powered through a modified  $\Pi$ -type matching network using a 4 MHz RF generator. Plasma density and ion energy can be controlled separately using high frequency top electrode RF power and low frequency bottom electrode RF bias power.

For the FC-based atomic layer etching work, a custom-built inductively coupled plasma (ICP) system was used.<sup>1-5</sup> A 13.56 MHz source power is applied through a water-cooled coil above a quartz window with an L-type matching network. The plasma was confined within a 195 mm diameter anodized Al confinement ring. A 125 mm diameter silicon substrate is located 150 mm below the top electrode on an electrostatic chuck. The bottom electrode can be biased with another RF bias power supply at 3.7 MHz allowed ion bombardment energy control.

In the last part of this work, the electron beam (EB) etching experiments were performed in an electron beam etching system, consisting of a hollow cathode (HC) EB source on top of a reaction chamber and an electron cyclotron wave resonance (ECWR) remote plasma source on the side. The pressure in the HC source (Torr level) is significantly higher than the chamber pressure below because of a choked flow connection. The ECWR remote plasma source consists of a COPRA DN160 ECWR plasma beam source running at 13.56 MHz radio frequency with a modified neutralization plate. This neutralization plate consists of an electrically grounded

aluminum plate covered by Kapton tape and a quartz plate protecting the plate from plasma erosion. Direct exposure of the substrate and reaction chamber to the ECWR plasma is prevented by this plate, and only neutral chemical radicals can diffuse from the ECWR chamber to the processing chamber, creating a remote plasma process condition. The ECWR effect requires an additional static magnetic field to utilize interaction of an electromagnetic wave with a plasma.<sup>1,17</sup> A 400 W source power level and 1.8 mT static magnetic field were applied in the ECWR work for all experiments requiring chemical radicals.

The EB source, consists of a 1.57 mm diameter direct current (DC) HC tube, a 34.35 mm diameter discharge tube, an anode plate with a hole in it, a separation mesh and an electron acceleration plate. The latter is located below the HC source and inside the vacuum chamber above a water cooled (10 °C) and electrically grounded stainless steel (S. S.) substrate. The electrons are extracted from the HC plasma through a 1.57 mm diameter hole in the anode. A S. S. mesh with high transmission is attached to the anode plate and prevents the extraction electric field to penetrate into the HC plasma region.

For all reactors used in this work, a base pressure of  $10^{-6}$  Torr is achieved before any processing. The reaction chamber processing pressure was kept at 2-100 mTorr using a butterfly valve in the mechanical pump backed turbo molecular pumping line.

Typically, we did not process full wafers but 1x1 inch<sup>2</sup> samples cut from full wafers. The samples were placed on a water-cooled substrate the temperature of which was stabilized at 10 °C during processing.

All plasma processing systems have various gas phase and surface diagnostics built in, and are additionally connected to a vacuum cluster for sample vacuum transport to a surface chemistry analysis system.

Additional details of these reactors will be described in the following chapters respectively.

#### **1.4 Brief Description of Materials Used**

In this study we utilized various electronic materials for plasma processing. The materials were all silicon based and included a commercial Si based low dielectric constant (low-k) material (Black Diamond II (BDII)), SiO<sub>2</sub>, Si<sub>3</sub>N<sub>4</sub> and polycrystalline Si. Stacks of materials, e.g. SiO<sub>2</sub>-Si<sub>3</sub>N<sub>4</sub>-SiO<sub>2</sub> stacked samples with varying thicknesses were studied primarily for ALE work since this allowed to achieve the highest measurement sensitivity and the best observation of material transitions from one material to a second material, e.g. SiO<sub>2</sub> to Si<sub>3</sub>N<sub>4</sub> during etching. The polycrystalline Si sample is deposited on top of a thin layer of SiO<sub>2</sub>, which maximizes the ellipsometry measurement precision. All samples were provided by our industrial collaborators. More information on the materials used will be presented in the following chapters.

#### **1.5. Characterization Techniques**

The sample material films were characterized by a variety of techniques including, but not limited to, *in-situ* ellipsometry, *ex-situ* spatially resolved ellipsometry, and X-ray photoelectron spectroscopy (XPS).

Plasma conditions were characterized using Optical Emission Spectroscopy (OES) and Langmuir Probe (LP).

### **Ellipsometry**

The material film thicknesses and optical indexes were studied using an *in-situ* ellipsometry setup that used a HeNe laser ( $\lambda = 632.8$  nm). The ellipsometer is an automated rotating compensator ellipsometer working in the polarizer-compensator-sample-analyzer (PCSA) configuration at a  $\approx 72^\circ$  angle of incidence. Optical multilayer modeling was used to analyze the measured data and to establish real-time thickness evolution of various films. Spatial resolved *ex-situ* ellipsometry was used for characterizing the etching profile across the sample.

### **X-ray Photoelectron Spectroscopy (XPS)**

X-ray photoelectron spectroscopy (XPS) analysis provides information on the chemical composition of the film surface. The analysis was performed using a Vacuum Generators ESCALAB MK II surface analysis system that is interconnected to the various plasma devices with a central wafer handler that allows sample transfer under vacuum to the surface analysis system for measurements. High resolution scans of characteristic energy regions, e.g. Si2p, C1s, O1s, N1s and F1s binding energy regions for fluorocarbon plasma processed Si<sub>3</sub>N<sub>4</sub>, were obtained at 20 eV pass energy at an electron take-off angle of 90° and 20° with respect to the sample surface. The spectra were fitted using least-squares fitting routines with 70/30 % Gaussian/Lorentzian line shapes at fixed full width at half maximum (FWHM) for each spectrum after Shirley background subtraction. All fittings were obtained with

consistency across all individual spectra, i.e. the chemical compositions deduced from the measured spectral intensities was internally consistent for each sample surface.

### **Optical emission spectrometer**

Optical emission from the plasma is an indicator of chemical species and plasma densities by the emission of plasma excited states.<sup>1.18</sup> It was used extensively in this study as a way to determine the gas phase precursor species density in order to correlate the surface etching behavior to the plasma gas phase properties.

### **Langmuir Probe**

The electron beam generated plasma electron and the primary beam electron properties were characterized using a Langmuir probe from PlasmaSensors in collaboration with Dr. Valery Godyak.<sup>1.19</sup>

## **1.6 Thesis Outline**

The main goal of this work is to develop and characterize novel plasma etching methods of electronic materials by a) optimizing the composition and structure of precursor gas molecules, b) achieve ultra-high materials etching selectivity in ion-based atomic layer etching by utilizing the enhanced control parameters not available in CW plasma etching approaches, and c) explore electron-induced etching by direct electron beam injection into the downstream reactive gaseous environment created by a separate plasma source.

In chapter 2, a systematic study of hydrofluorocarbon (HFC) precursor structure impact on low-k dielectric material etching established a fundamental basis for HFC gas behavior in terms of polymerization rate, gas-surface interactions and etching selectivity of low-k material to amorphous carbon. The results of this work

are the basis of further applications of novel HFC precursors for other plasma processing applications, e.g. as demonstrated recently atomically abrupt materials-selective ALE<sup>1,4</sup>.

In chapter 3 we developed a new method of ALE to achieve extremely high etching selectivity of SiO<sub>2</sub> to Si<sub>3</sub>N<sub>4</sub> by using a FC accumulation conditions. In that situation, FC film can be selectively accumulated on low carbon consumption materials such as Si<sub>3</sub>N<sub>4</sub>, allowing perfect etching-stop after ALE of a top layer like SiO<sub>2</sub> which reacts with more carbon during etching.

To overcome limitations of ion-based surface activation approaches for plasma etching, electron beam enhanced material etching was established for Si<sub>3</sub>N<sub>4</sub> and polycrystalline Si etching in Chapter 4. This was achieved by direct electron beam injection into the downstream reactive gaseous environment created by a separate CF<sub>4</sub>/O<sub>2</sub> plasma source. Using a Langmuir probe measurement, it was possible to directly observe the primary beam electrons and changes in this distribution as inelastic collisions with the background gas led to additional ionization and excitation. This electron beam induced plasma was further characterized by optical emission. The surface etching aspects were examined by *in-situ* and *ex-situ* spatial resolved ellipsometry measurements which confirmed the electron-chemical synergy effect for material etching.

Chapter 5 extends the study of the electron beam enhanced etching approach to a systematic survey of the full parameter space. The role of process parameters like precursor gas composition, extraction voltage, discharge current, pressure and source to sample distance on plasma properties and surface etching behavior were

characterized to arrive at a more complete understanding of cause and effect for this novel approach.

In chapter 6, the main findings and conclusions are summarized. In addition, possible future work directions are discussed.

## Chapter 2: Impact of Hydrofluorocarbon Molecular Structure Parameters on Plasma Etching of Ultra-Low-K Dielectric

*Journal of Vacuum Science & Technology A 34, 031306 (2016)*

C. Li, R. Gupta, V. Pallem, and G. S. Oehrlein

### ABSTRACT

The authors report a systematic study aimed at evaluating the impact of molecular structure parameters of hydrofluorocarbon (HFC) precursors on plasma deposition of fluorocarbon (FC) films and etching performance of a representative ultralow dielectric constant (ultra-low-k) material, along with amorphous carbon. The precursor gases studied included fluorocarbon and hydrofluorocarbon gases whose molecular weights and chemical structures were systematically varied. Gases with three different degrees of unsaturation (DU) were examined. Trifluoromethane ( $\text{CHF}_3$ ) is the only fully saturated gas that was tested. The gases with a DU value of one are 3,3,3-trifluoropropene ( $\text{C}_3\text{H}_3\text{F}_3$ ), hexafluoropropene ( $\text{C}_3\text{F}_6$ ), 1,1,3,3,3-pentafluoro-1-propene ( $\text{C}_3\text{HF}_5$ ), (E)-1,2,3,3,3-pentafluoropropene ( $\text{C}_3\text{HF}_5$  isomer), heptafluoropropyl trifluorovinyl ether ( $\text{C}_5\text{F}_{10}\text{O}$ ), octafluorocyclobutane ( $\text{C}_4\text{F}_8$ ), and octafluoro-2-butene ( $\text{C}_4\text{F}_8$  isomer). The gases with a DU value of two includes hexafluoro-1,3-butadiene ( $\text{C}_4\text{F}_6$ ), hexafluoro-2-butyne ( $\text{C}_4\text{F}_6$  isomer), octafluorocyclopentene ( $\text{C}_5\text{F}_8$ ), and decafluorocyclohexene ( $\text{C}_6\text{F}_{10}$ ). The work was performed in a dual frequency capacitively coupled plasma reactor. Realtime characterization of deposition and etching was performed using in situ ellipsometry, and optical emission spectroscopy was used for characterization of  $\text{CF}_2$  radicals in the

gas phase. The chemical composition of the deposited FC films was examined by x-ray photoelectron spectroscopy. The authors found that the  $\text{CF}_2$  fraction, defined as the number of  $\text{CF}_2$  groups in a precursor molecule divided by the total number of carbon atoms in the molecule, determines the  $\text{CF}_2$  optical emission intensity of the plasma.  $\text{CF}_2$  optical emission, however, is not the dominant factor that determines HFC film deposition rates. Rather, HFC film deposition rates are determined by the number of weak bonds in the precursor molecule, which include a ring structure,  $\text{C}=\text{C}$ ,  $\text{C}\equiv\text{C}$ , and  $\text{C}-\text{H}$  bonds. These bonds are broken preferentially in the plasma, and/or at the surface and fragments arriving at the substrate surface presumably provide dangling bonds that efficiently bond to the substrate or other fragments. Upon application of a radio-frequency bias to the substrate, substrate etching is induced. Highly polymerizing gases show decreased substrate etching rates as compared to HFC gases characterized by a lower HFC film deposition rate. This can be explained by a competition between deposition and etching reactions, and an increased energy and etchant dissipation in relatively thicker steady state FC films that form on the substrate surface. Deposited HFC films exhibit typically a high  $\text{CF}_2$  density at the film surface, which correlates with both the  $\text{CF}_2$  fractions in the precursor molecular structure and the deposition rate. The FC films deposited using hydrogen-containing precursors show higher degrees of crosslinking and lower F/C ratios than precursors without hydrogen, and exhibit a lower etch rate of substrate material. A small gap structure that blocks direct ion bombardment was used to simulate the sidewall plasma environment of a feature and was employed for in situ ellipsometry measurements. It is shown that highly polymerizing precursors with a DU of two

enable protection of low-k sidewalls during plasma exposure from oxygen-related damage by protective film deposition. Dielectric film modifications are seen for precursors with a lower DU.

## 2.1 INTRODUCTION

Fluorocarbon-based plasma has been widely used in the semiconductor industry for etching of dielectric materials.<sup>2.1–2.8</sup> The fluorocarbon (FC) precursor molecular structure has been shown to impact plasma processes and surface properties.<sup>2.9–2.17</sup> However, many mechanistic details by which fluorocarbon-based plasma etching and polymerization takes place have remained unclear. While fluorocarbon-based plasma deposition of thin films has been related to  $\text{CF}_2$  radicals, large  $\text{C}_x\text{F}_y$  groups, hydrogen addition, and ion bombardment, the understanding of the role of precursor molecular structure and composition for FC plasma production, plasma–surface interaction, and film formation on the substrate is still poor<sup>2.18–2.24</sup>. Additionally, the impact of FC precursor molecular structure with regard to plasma etching performance and plasma surface interactions is still not well known. This work focused on the relative importance of precursor structure versus chemical composition for low-k dielectric material etching performance. In this work, the authors investigated mechanisms of plasma-based FC deposition and low-k material etching by varying the precursor molecular structure and chemical composition, i.e., fluorine to carbon ratio, presence/absence of carbon double or triple bonds, presence/absence of hydrogen, and ring versus linear structure to provide systematic guidelines for precursor selection for industrial applications. This article is organized as follows: in the first part, the authors studied the dependence of  $\text{CF}_2$  optical emission, FC film deposition rates, and surface chemistry on precursor structure, and established the respective roles of  $\text{CF}_2$  and weak bonds in the precursor. In the second part, the authors studied the dependence of blanket low-k material etching

performance on precursor. Finally, a low-k sidewall (SW) simulation study was performed, and the dependence of low-k dielectric sidewall damage on precursor gases is reported.

## **2.1 EXPERIMENT**

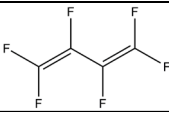
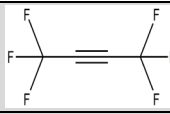
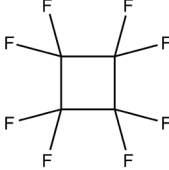
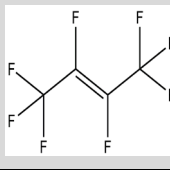
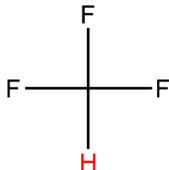
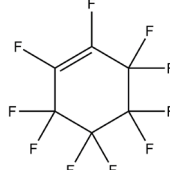
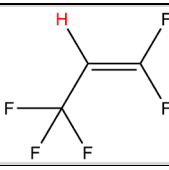
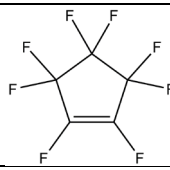
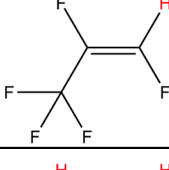
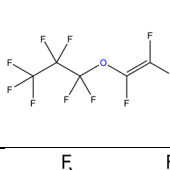
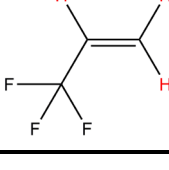
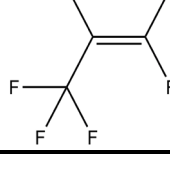
A description of materials and precursors used in this work, along with the plasma reactor configuration, process conditions, gap structure setup, and characterization method, follows.

### **2.1.1 Description of material and precursor gases**

The low-k material used in this work was 500 nm thick Black diamond II™ (BDII), which is a chemical vapor deposited (CVD) porous SiCOH film with a dielectric constant of 2.2 on a silicon substrate. The porosity is induced in the silicon-dioxide-based CVD film by ultraviolet curing. Properties and characterizations of this material can be found in a previous study.<sup>2.25</sup> The porous structure and hydrocarbon composition make the low-k material susceptible to plasma induced changes, i.e., damage.<sup>2.26, 2.27</sup> The hard mask material studied was amorphous carbon (aC). Table 2.1 lists and describes the precursor gases considered in this work. The authors studied traditional industrial precursors, such as cyclic C<sub>4</sub>F<sub>8</sub> (cC<sub>4</sub>F<sub>8</sub>), C<sub>4</sub>F<sub>6</sub> with double bonds, C<sub>5</sub>F<sub>8</sub>, and CHF<sub>3</sub>. The double bond isomer of C<sub>4</sub>F<sub>8</sub> and triple bond isomer of C<sub>4</sub>F<sub>6</sub> were also studied. The authors also studied C<sub>3</sub>F<sub>6</sub>, which has the same F/C ratio as C<sub>4</sub>F<sub>8</sub>, and hydrogen substituted gases, e.g., C<sub>3</sub>HF<sub>5</sub> isomers, for which the hydrogen position in the molecule was varied, and C<sub>3</sub>H<sub>3</sub>F<sub>3</sub>. In addition, the authors examined an oxygen containing precursor, C<sub>5</sub>F<sub>10</sub>O, and another large molecular precursor, C<sub>6</sub>F<sub>10</sub>. The comparison of these gases allows to draw conclusions as to the

role of several precursor structural parameters. For example, the effect of single, double, and triple carbon bonds can be investigated by comparing the  $C_4F_8$  and  $C_4F_6$  isomers. The  $C_3HF_5$  isomer comparison provides insight into the impact of the hydrogen position within the molecule and  $CF_2$  groups. Comparing  $C_3HF_5$  with  $C_3F_6$  highlights the roles of  $CF_2$  groups and hydrogen. The role of oxygen can be studied by comparing  $C_5F_{10}O$  to other nonoxygen containing precursor gases.

Table 2.1 Precursor gas chemical  $CF_2$  fraction in gas structure, and degree of unsaturation (DU) for the precursors studied in this work.

	Gas	Structure	$CF_2\%$	DU		Gas	Structure	$CF_2\%$	DU
Traditional	$C_4F_6\_DB$		50%	2	Isomers	$C_4F_6\_TB$		0%	2
	$cC_4F_8$		100%	1		$C_4F_8\_DB$		0%	1
	$CHF_3$		0%	0		$C_6F_{10}$		33%	2
	Other Hydrogen Containing	$C_3HF_5\_1$		33%		1	Other Candidates	$C_5F_8$	
$C_3HF_5\_2$			0%	1	$C_5F_{10}O$			60%	1
$C_3H_3F_3$			0%	1	$C_3F_6$			60%	1

### **2.1.2 The dual frequency capacitively coupled plasma reactor and processing conditions**

This work used a dual frequency capacitively coupled plasma reactor. A pair of 5 inch diameter electrodes is located in the center of a stainless steel vacuum chamber with 10 inch diameter. The gap between the two electrodes is 50 mm. The top electrode features a showerhead design for gas distribution. The 13.56 MHz source power is using an L-type matching network configuration. The bottom electrode is powered through a modified  $\Pi$ -type matching network using a 4 MHz RF generator. Plasma density and ion energy can be controlled separately using high frequency top electrode RF power and low frequency bottom electrode RF bias power. This independent control is possible because electrons are heated efficiently by high frequency RF power, while ions are more effectively accelerated by low frequency RF power. A more detailed description of this CCP system can be found in prior publications.<sup>2,28</sup>

The bottom electrode is kept at 10 °C via backside water cooling. Samples are mounted on the cooled bottom electrode by thermal grease to provide good temperature control. The chamber base pressure was  $\sim 5 \times 10^{-6}$  Torr, generated by a magnetically suspended turbo molecular pump backed by a roots blower and a mechanical pump.

The experiments were done at 50 W source power, 35 W bias power (if bias power was applied), and 20 mTorr pressure in an oxygen plasma cleaned chamber.

For the experiments in section III (A), the processing gas consisted of 4 sccm (standard cubic centimeter per minute, at STP) precursor flow along with 36 sccm Ar flow. No bias power was applied for the FC film deposition work.

For the experiments in section III (B), etching and deposition tests were done with 5 % precursor in Ar with 40 sccm total gas flow rate. A 35 W RF bias power was applied to the substrate. An additional O<sub>2</sub> flow rate of 4 sccm was used for both BDII and aC etching conditions which increased etch rates and reduced surface polymerization. For better comparison, 5 sccm O<sub>2</sub> flow was used for C<sub>3</sub>H<sub>3</sub>F<sub>3</sub> due to a lack of etching on aC with low O<sub>2</sub> flow rate. This increased O<sub>2</sub> flow was found not to influence the parametric trend and conclusions.

For the experiments in section III (C), a gap structure was used to investigate how the low-k material interacts with different precursor gases in a simulated sidewall environment for which no direct ion bombardment takes place.<sup>2,28, 2.29</sup> The aspect ratio (A/R) of the small gap structure was selected to be the same as that of typical trench structures, and was ~15 at the center of the gap structure. The roof width was 39 mm and the gap height was 1.3 mm. This roof was used underneath an aluminum block with two small holes for the path of the laser used in *in situ* ellipsometry, and enabled *in situ* measurement of sample surface modifications. A more detailed description of the modified gap structure can be found in previous work.<sup>2,29</sup> The gas flows were 40 sccm of 5 % precursor mixed in Ar with addition of 4 sccm O<sub>2</sub>. Since there is no ion bombardment under the small gap structure or on the sidewall of the trench, no RF bias power was applied to avoid additional heating to the gap structure.

The plasma and gas operating conditions selected for this precursor comparison are targeted at low-k etching applications. The relatively low precursor concentration used in this work is characteristic of these applications, and also ensures that all precursors are tested under similar etching or deposition conditions, even if their individual polymerization properties strongly differ. A Kapton film covered the aluminum top electrode for the experiment section III (B) to avoid aluminum sputtering from the top electrode for these etching experiments. For the work discussed in section III (A) and (C), no Kapton was exposed in the plasma. Comparison tests have been performed, and showed that while the presence of Kapton in the process chamber will slightly increase the FC film deposition rate and influence the surface chemistry, the parametric trends seen for the different precursor molecules remain the same.

### **2.1.3 Surface and Optical Characterizations**

X-ray photoelectron spectroscopy was used to measure surface chemical changes after plasma processing. The analysis was performed with a Vacuum Generators ESCALAB MK II equipped with an Mg  $K_{\alpha}$  source (1253.6 eV). The FC film was scanned after passive deposition (no bias power) in the CCP chamber and subsequent air-transfer to XPS. Survey spectra and high resolution C 1s and F 1s spectra with 20 eV pass energy and two electron take-off angles (20° and 90° relative to substrate surface) were scanned for all samples. This article focuses on the C 1s spectra scanned at normal electron emission angle for FC film comparison, except for the isomer difference spectra comparison. The spectra were fitted with C-C/CH, C-CF<sub>x</sub>, C-F, C-F<sub>2</sub> and C-F<sub>3</sub> moieties employing 70/30 % Gaussian/Lorentzian line

shapes after Shirley background subtraction. The FC film F/C ratio is calculated according to<sup>2.22, 2.30</sup>

$$\frac{F}{C} = \frac{CF + 2 \times CF_2 + 3 \times CF_3}{\text{total carbon area}} \quad (2.1)$$

The degree of crosslinking can be estimated by<sup>2.13, 2.31</sup>

$$\text{crosslinking} = \frac{CC + CCF_x + CF}{\text{total carbon area}} \quad (2.2)$$

This expression is an approximation, and ignores some of the chain elongating or terminating species, such as FC=CF<sub>2</sub> or FC=CF, from branching sites, like FC=C, CF-CF or C-CF, due to XPS C1s limited energy resolution, which is discussed by L. Reto *et al.*<sup>2.31</sup> Optical emission spectroscopy (OES) was used to measure emission intensities in the plasma gas phase. The CF<sub>2</sub> emission at a wavelength of 259 nm is measured, and normalized to the Ar emission intensity at a wavelength of 750 nm.

An *in situ* ellipsometer with a 632.8 nm He-Ne laser was installed in the processing chamber to monitor substrate material thickness changes and surface modifications in real time. Due to the similar refractive indices of FC and BDII (~1.3 to 1.4), a single layer model was applied for the FC deposition rate and etch rate measurements.

## 2.2 RESULTS AND DISCUSSION

### 2.2.1 Correlations of CF<sub>2</sub> emission, fluorocarbon deposition rate, and surface chemistry of hydrofluorocarbon based plasma

Figure 2.1 shows an overview of the FC deposition process. Precursor weak bonds will preferentially break and precursor fragments adsorbed at the surface

provide sites for attachment of additional fragments. Energetic ions bombarding the FC surface induces etching and damage of the FC film structure. The  $\text{CF}_2$  moiety is often abundant in these precursors, and can be measured in the gas phase upon dissociation of the parent molecule, and also at the surface after incorporation in a depositing film.<sup>2.32</sup>

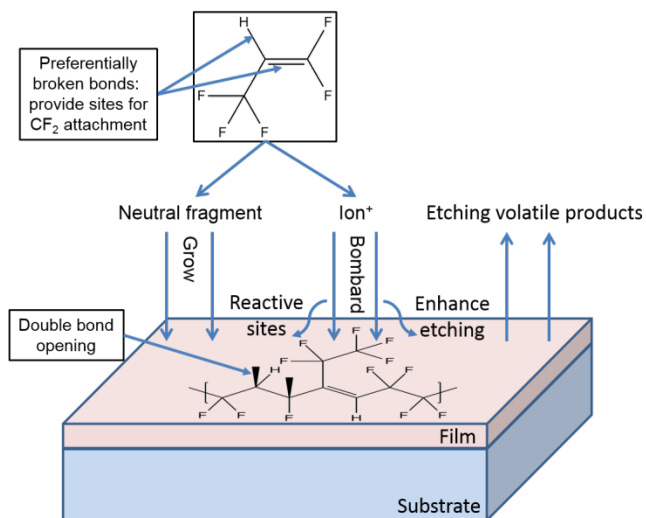


FIG. 2.1 (Color online) Overview of FC deposition process. Precursor weak bonds will preferentially break and provide sites for polymerization. On the other hand, energetic ions will be accelerated and bombard on FC surface, inducing etching and damage to FC film structure.

### 2.2.1.1 $\text{CF}_2$ optical emission and surface $\text{CF}_2$ concentration dependence of precursor $\text{CF}_2$ fraction

The authors measured the  $\text{CF}_2$  optical emission and the deposition rate *in situ* and deposited film chemical composition after the plasma treatment. The  $\text{CF}_2$  optical emission intensity correlates with the  $\text{CF}_2$  group fraction in precursor gas structure, see Fig. 2.2 The  $\text{CF}_2$  fraction refers to the number of  $\text{CF}_2$  groups divided by the total number of carbon atoms in the precursor gas structure, and is plotted on the y-axis,

with the bottom five gases having no CF<sub>2</sub> group. A linear relation between the CF<sub>2</sub> optical emission intensity and the CF<sub>2</sub> fraction in the precursor structure is observed, with a regression coefficient of 0.79. Linear regression fittings are shown with dashed lines. Two gases do not follow this trend: One is an oxygen containing gas, C<sub>5</sub>F<sub>10</sub>O, which showed lower CF<sub>2</sub> emission intensity than expected. The strongly reduced CF<sub>2</sub> intensity can be explained by oxygen reaction with carbon in CF<sub>2</sub>.<sup>2,33</sup> Second, the C<sub>4</sub>F<sub>6</sub> containing two double bonds showed relatively higher CF<sub>2</sub> emission than the fitted trend line in Fig. 2.2. The mechanism for this is unclear at present and still being investigated.

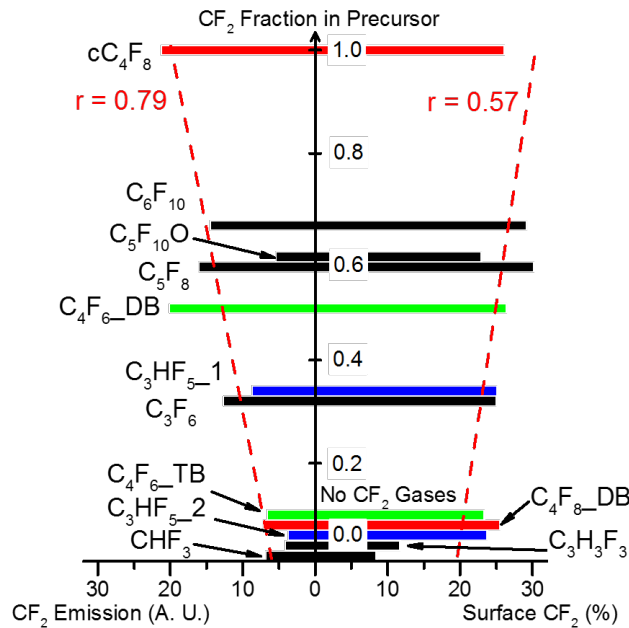


FIG. 2.2 (Color online) CF<sub>2</sub> optical emission and deposited film surface CF<sub>2</sub> intensity vs. CF<sub>2</sub> fraction (CF<sub>2</sub> number /C number) in gas structure. Isomer pairs are in the color of red, green, and blue. CF<sub>2</sub> emission intensity has good correlation to gas structure, while the surface CF<sub>2</sub> is not.

Figure 2.2 also shows the surface CF<sub>2</sub> bond fraction in the deposited FC films obtained from the C 1s spectra in XPS measurements. Precursors with higher CF<sub>2</sub> fraction deposit CF<sub>2</sub> rich FC films, indicating the precursor structure information can influence the deposited film chemistry. However, the correlation between the precursor structure and surface chemistry is weaker than that seen between precursor structure and CF<sub>2</sub> optical emission. The surface CF<sub>2</sub> concentration varies less than gas phase CF<sub>2</sub> emission among these gases, indicating CF<sub>2</sub> from the gas phase may not strongly deposit and/or that surface processes strongly modify deposited chemical moieties<sup>2,32</sup>, e.g. by ion bombardment conditions of the surface without RF bias. The hydrogen containing gases with no CF<sub>2</sub> groups showed low surface CF<sub>2</sub> concentrations. This can be explained by hydrogen reaction with the deposited film, e.g. fluorine abstraction to form HF.<sup>2,22</sup>

Isomers sharing the same elemental composition but different molecular structure show different CF<sub>2</sub> emission intensity behavior. For example, the C<sub>4</sub>F<sub>6</sub> isomers have the same carbon and fluorine number, but double bonded C<sub>4</sub>F<sub>6</sub> contains two CF<sub>2</sub> groups and two CF groups, whereas the triple bond C<sub>4</sub>F<sub>6</sub> consists of two CF<sub>3</sub> groups. This structure difference is consistent with the observation that the CF<sub>2</sub> emission intensity of the double bonded C<sub>4</sub>F<sub>6</sub> is much higher than for the triple bonded moiety, and indicates that the CF<sub>2</sub> emission can reflect the precursor structure. Again, the difference of the surface CF<sub>2</sub> intensity of the deposited FC films is small.

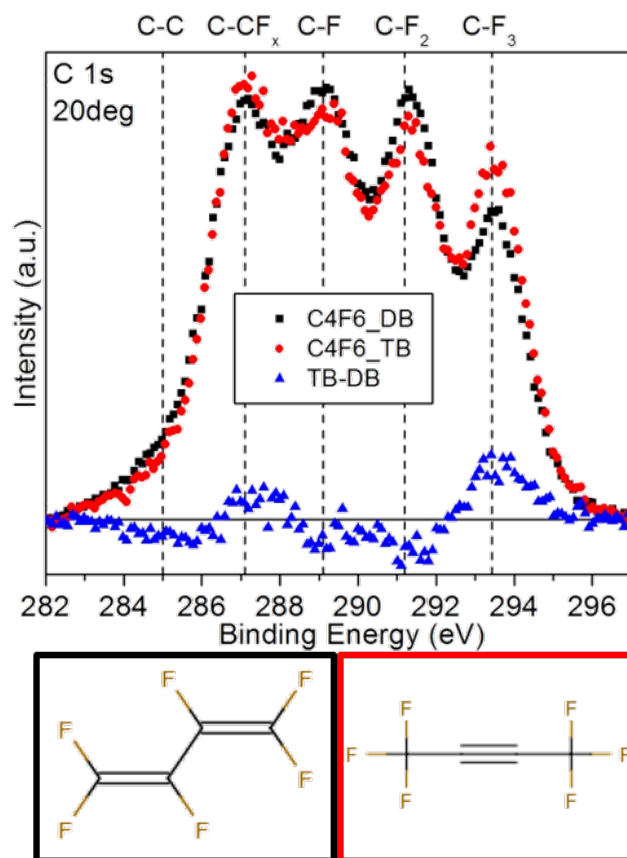


FIG. 2.3 (Color online) High resolution C 1s XPS spectra of deposited film of  $C_4F_6$  isomers with differential spectra (panel a). Peak assignments are indicated at the top of the spectra. Precursor gas structures are shown at panel b. With ion bombardment, crosslinking degree is high for the deposited film. Surface chemistry has a weak memory from the gas structure.

Figure 2.3 shows the C 1s spectra of the deposited FC films and the difference spectrum for the two  $C_4F_6$  isomers for a 20 degree angle of electron emission. The difference spectrum shows that the surface chemical composition difference reflects the molecular structure of the gas to some extent. However, compared to the absolute intensity value, the difference is small. This small difference suggests that the memory of the precursor gas structure as reflected in observed surface chemistry is

weak for the surface processing conditions in the CCP reactor. This is plausible since ion bombardment of the growing FC film will destroy the structural information, and lead to a highly crosslinked film (high C-C, C-CF<sub>x</sub> and C-F content) and a weak memory effect.<sup>2,34</sup> This result agrees with the weak relation between gas CF<sub>2</sub> fraction and surface CF<sub>2</sub> intensity for all gases seen in Fig. 2.2.

### **2.2.1.2 CF<sub>2</sub> optical emission and surface CF<sub>2</sub> concentration dependence of FC deposition rate.**

To study the correlation between FC deposition rate, precursor molecular structure, plasma gas phase composition, and surface chemistry, the CF<sub>2</sub> emission and surface CF<sub>2</sub> bond intensity are shown with respect to measured FC film deposition rate for each precursor in Fig. 2.4. The degree of unsaturation (DU) is marked in Fig. 2.4, which determined by the sum of ring number and  $\pi$  bond number, e.g. DU is 1 for a carbon double bond, and 2 for a carbon triple bond. Reactivity increases strongly with DU.

There is no clear correlation between CF<sub>2</sub> emission and deposition rate (left part of Fig. 2.4), suggesting that CF<sub>2</sub> is not a key factor for FC deposition rate, consistent with prior work.<sup>2,19</sup> Figure 2.4 shows that the FC deposition rates for the different precursors are separated into three major groups according to the DU of the precursor gas. A possible mechanism is that broken unsaturated bonds provide more dangling bonds allowing radicals from the gas phase to attach at these sites. For example, radicals will attach at the C=C bonds by changing the bonding structure at the surface, enabling a higher deposition rate. This will be discussed in more detail in the next section.

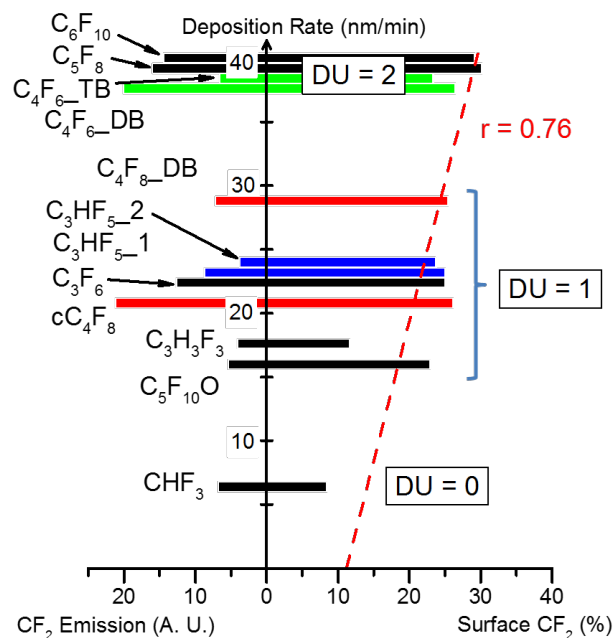


FIG.2.4 (Color online)  $\text{CF}_2$  optical emission and deposited film surface  $\text{CF}_2$  intensity vs. deposition rate. High deposition rate gas minimizes ion bombardment modification of the surface. Precursor gases with different deposition rate is separated by degree of unsaturation ( $\text{DU} = \text{Ring} + \text{C}=\text{C} + 2 \times \text{C}\equiv\text{C}$ ). Isomer pairs are in the color of red, green, and blue.

The right part of Fig. 2.4 shows the relation between deposition rate and surface  $\text{CF}_2$  concentration. A high deposition rate minimizes the destruction of the film structure by ion bombardment and thus will retain more of the molecular structure of the fragments arriving at the surface, e.g. surface  $\text{CF}_2$ . As a result, FC films deposited at high rates can retain more precursor gas structural information, e.g. higher surface  $\text{CF}_2$  concentration.

Combining the factors of deposition rate and  $\text{CF}_2$  fraction for surface  $\text{CF}_2$  concentration, the normalized product of these two factors is plotted against the surface  $\text{CF}_2$  concentration in Fig. 2.5. The product shows a better correlation than the

one seen when deposition rate was not considered (Fig. 2.2), but the correlation is worse than if only the deposition rate considered. This suggests that surface  $\text{CF}_2$  concentration is primarily determined by FC deposition rate, e.g. due to minimizing modification of the surface FC film relative to film growth. Precursor  $\text{CF}_2$  fraction, which is the theoretical value of available  $\text{CF}_2$ , only has a small impact. The fact that ion bombardment at the depositing surface will destroy precursor structure-related information by ion impact dissociation is a plausible explanation.

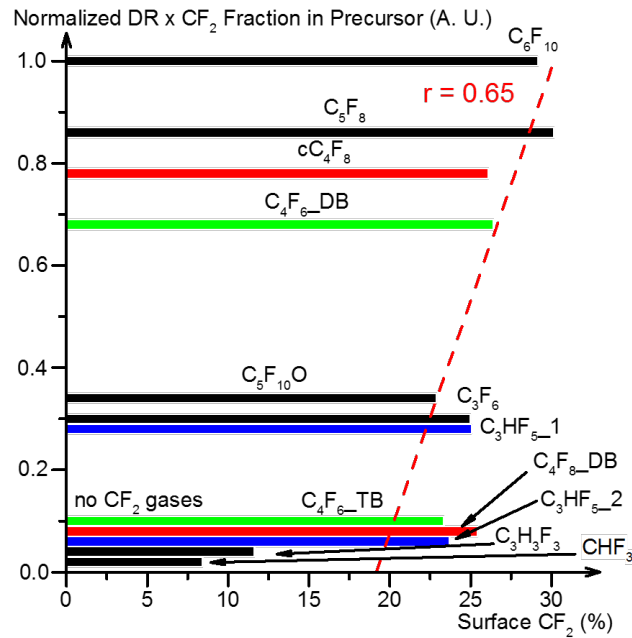


FIG. 2.5. (Color online) Surface  $\text{CF}_2$  vs. normalized product of deposition rate (DR) and  $\text{CF}_2$  fraction in precursor. No  $\text{CF}_2$  gases can also have  $\text{CF}_2$  bond on the surface.

In Fig. 2.6, the dependence of surface F/C and crosslinking degree of FC film deposited by precursor gases on the deposition rate is investigated. The hydrogen containing precursors show low F content in the film and leave a highly crosslinked

film. This effect should be caused by the same reason as that low surface  $\text{CF}_2$  shown on deposited FC film, i.e. hydrogen-induced fluorine abstraction.<sup>2,22</sup>

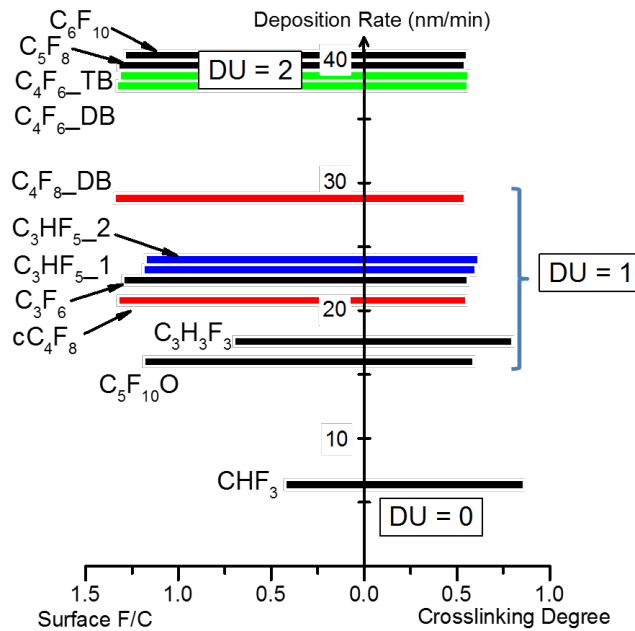


FIG. 2.6 (Color online) Correlation between deposition rate and deposited FC film crosslinking degree and F/C ratio, characterized by XPS C1s high resolution scan (Crosslink =  $\text{C-C \%} + \text{C-CFx \%} + \text{C-F \%}$ ,  $\text{F/C} = \text{C-F \%} + 2*\text{C-F}_2 \% + 3*\text{C-F}_3 \%$ , each peak intensity percentage is calculated by total carbon area). Hydrogen containing gases show strongly interaction with F, leaving a low F/C and highly crosslinked film.

### 2.2.1.3 Role of $\text{CF}_2$ and precursor weak bonds for fluorocarbon deposition

Figure 2.7 shows the deposition rate dependence for selected gases versus the logarithm of gas phase  $\text{CF}_2$  optical emission for 5, 10, and 15% precursor addition in Ar. A linear relation between deposition rate and logarithm of  $\text{CF}_2$  optical emission is seen for each gas. Similar relationships were seen for the other gases investigated, and have been omitted for sake of clarity. More FC gas in the plasma causes higher

CF<sub>2</sub> emission and a higher FC deposition rate. Varying slopes of the fitting line and different FC deposition rates at the same CF<sub>2</sub> emission indicates that CF<sub>2</sub> does not dominate FC deposition.

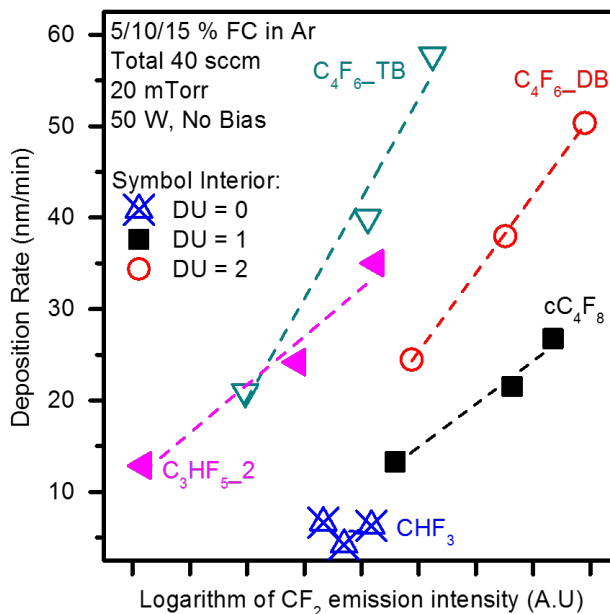


FIG. 2.7 (Color online) Selected precursor deposition rate dependence of logarithm of gas phase CF<sub>2</sub> optical emission intensity.

Table 2.2: Bond Energies<sup>2,44</sup>

Bond Energies	
Bond	Energy (kJ/mol)
C-C	348
C-H	412
C-O	360
C-F	484
C=C	612
C≡C	837

In order to relate CF<sub>2</sub> deposition rate to precursor molecular structure, the authors considered the available dangling bond number due to breaking of specific

bonds in the precursor structure. The carbon single bond (C-C) is a  $\sigma$  bond, which is the strongest type of covalent chemical bond.<sup>2,35</sup> The carbon double bond (C=C) consists of one  $\sigma$  bond and one lower energy  $\pi$  bond. Carbon triple bond (C $\equiv$ C) consists of one  $\sigma$  bond and two lower energy  $\pi$  bonds. The bond energies are listed in Table 2.2. Please note that the bond energy only provides minimum dissociation thresholds, whereas actual plasma dissociation is complex and non-equilibrium process, and generally threshold energies are different since they reflect Franck-Condon effects, vibrational excitation, and so forth. The  $\pi$  bond energies in double and triple bond can be estimated by using their bond energy minus the C-C  $\sigma$  bond energy, which leaves 264 and 489 kJ/mol for the  $\pi$  bond energy in C=C and the two  $\pi$  bond energies in C $\equiv$ C. Assuming that the energy transferred to the precursors by electron impacts is not sufficient to break all carbon bonds, the lowest binding energy (B. E.) bond will be broken first, leaving available dangling bonds for CF<sub>2</sub> attachment. If the  $\pi$  bond in C=C is broken, there will be two available dangling bonds on these two carbon atoms. Similarly, C $\equiv$ C, carbon ring structure (ring open) and C-H will provide four, two, and one available dangling bond on the precursor structure, respectively. Figure 2.8 shows a strong correlation of the deposition rate with the available dangling bond number. The C<sub>3</sub>H<sub>3</sub>F<sub>3</sub> is an exception, which may be due to its high hydrogen concentration. The additional available dangling bonds presumably provide more available sites for attachment of radicals, e.g. CF<sub>2</sub>, which leads to high FC deposition rates and high surface CF<sub>2</sub> concentrations (Fig. 2.4). The oxygen containing gas, C<sub>5</sub>F<sub>10</sub>O, shows the lowest deposition rate with two available dangling bonds.

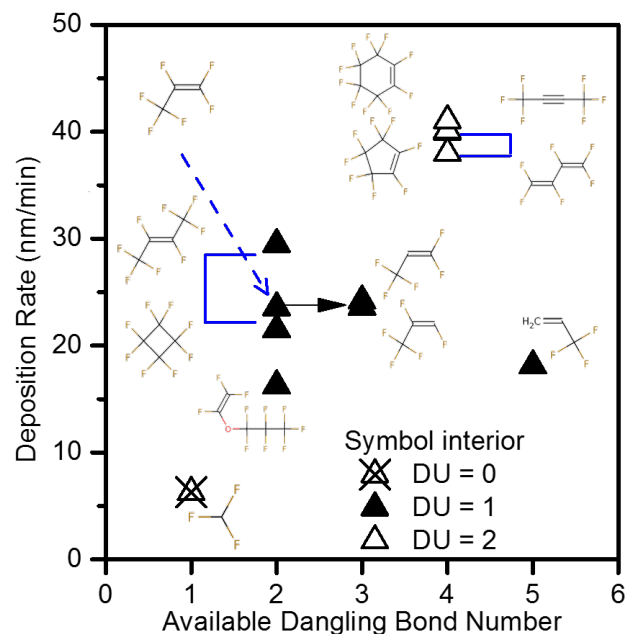


FIG. 2.8 (Color online) Deposition rate vs. precursor gas available dangling bond number after low binding energy bonds broken. Gas structures are shown next to the data.

Isomers studied in these work, which share the same chemical composition and available dangling bond number after weak bonds are broken, showed different deposition rates.  $C_4F_8$  with double bonded carbon showed a higher deposition rate than cyclic  $C_4F_8$ , and can be explained by the  $\pi$  bond binding energy in the double bond being lower than the binding energy of the  $\sigma$  bond in the ring structure.  $C_4F_6$  with triple bond showed higher deposition rate than double bonded  $C_4F_6$ , which can be explained by the binding energy sum of two  $\pi$  bonds in a triple bond being smaller than the sum of the binding energy of the two  $\pi$  bond in the two double bonds. From the comparison of these pairs of isomers, the authors conclude that the lower binding energy bonds are easier to break and leave dangling bonds for FC film formation, e.g. by  $CF_2$  attachment, thus contributing to a higher FC film deposition rate. The

comparison of the C<sub>3</sub>HF<sub>5</sub> isomers showed that the isomer with CF<sub>2</sub> exhibited only a slightly higher deposition rate than the isomer with no CF<sub>2</sub> group. This indicates again that the carbon chain structure in the precursor is the dominating factor for FC deposition rather than the CF<sub>2</sub> group fraction. C<sub>3</sub>F<sub>6</sub> and C<sub>3</sub>HF<sub>5</sub> have the same carbon chain structure, but the additional C-H group is susceptible to dangling bond formation when H is removed from the precursor. This makes it plausible that the two C<sub>3</sub>HF<sub>5</sub> precursors showed slightly higher deposition rate than C<sub>3</sub>F<sub>6</sub>. However, the impact of hydrogen is small relative to the overall impact of the carbon chain structure. More detailed comparisons and analysis require accurate calculations of the dissociation behavior of the weak bonds for each precursor structure. Overall, enhanced HFC film deposition seen for precursors with lower bond dissociation energies may be explained by carbon chains initially deposited to the substrate surface that provide reactive sites through weak carbon bond dissociation, e.g. C=C. Gas phase radicals can attach to those reactive sites by exchanging the binding structures. Additionally, the weak bonds may also accelerate the formation of oligomer in gas phase, enhancing the overall deposition rate.

## **2.2.2 BDII etching rate and selectivity dependence of precursor**

### **2.2.2.1 BDII and aC etch rate dependence of deposition rate**

Figure 2.9 shows the BDII and aC etch rate dependence on precursor deposition rate. The gases are sorted by precursor deposition rate on a relative scale on the y-axis. In general, high deposition rate gases show lower BDII and aC etch rate, which agrees with fluorocarbon-based plasma general etching model.<sup>2.1, 2.36, 2.37</sup> In this model, a FC film is continually depositing and etching on the substrate surface. As the fluorine in the FC film reacts with the substrate material, part of the deposited

FC film will be consumed. The consumption rate is proportional to the substrate etching rate. As a result, a steady-state FC film will form on the surface. High deposition rate gases will produce a thicker steady-state FC film on the substrate surface. This means more energy and etchant will be needed to maintain steady-state etching for this thicker FC film, which leads to a lower substrate etching rate.  $\text{CHF}_3$  and  $\text{C}_3\text{H}_3\text{F}_3$  show lower etch rates than the expected value. The lower etch rate is caused by the HFC film deposited is highly cross-linked and fluorine deficient, due to hydrogen removing fluorine in both the plasma and on the surface as discussed in the first section. This resulting carbonaceous film is difficult to etch.<sup>2,22</sup>

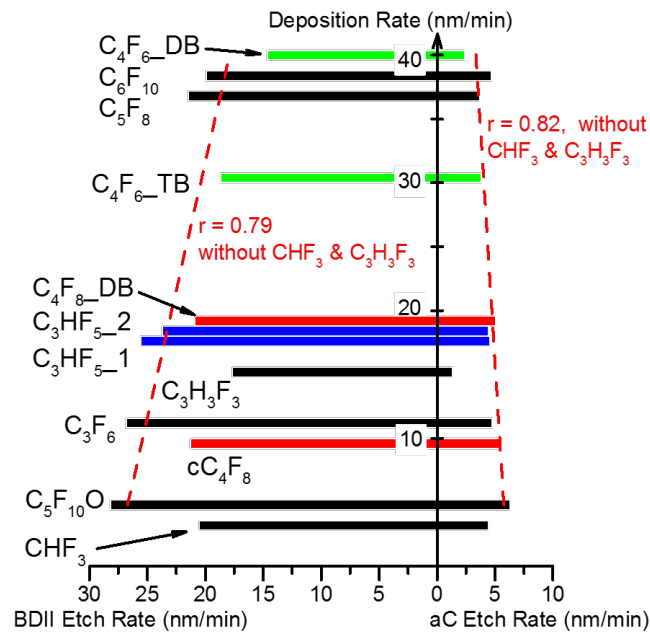


FIG.2.9 (Color online) BDII and aC etch rate vs. precursor deposition rate. High deposition rate precursor shows low etch rate.

### 2.2.2.2 Reduced F/C ratio, a parameter to evaluate hydrogen or oxygen containing precursor

A widely-used method to evaluate precursor polymerizing property is the F/C ratio in precursor structure.<sup>2.13, 2.38</sup> Lower F/C ratios are seen for highly polymerizing precursors. However, in the presence of hydrogen or oxygen in the precursor structure, this value will not reflect the effective chemical consequences in the discharge. The authors assume that the hydrogen in the precursor will fully dissociate from the precursor structure and bond with a fluorine atom to form HF.<sup>2.22, 2.39</sup> Oxygen will react with carbon and cause carbon consumption.<sup>2.33, 2.40</sup> With these assumptions, a reduced F/C ratio (RF/C) is defined as

$$\text{reduced } F / C = \frac{F - H}{C - O} \quad (2.3)$$

where H and O denote the corresponding numbers of H and O in the precursor molecule, respectively. Figure 2.10 shows the BDII etch rate and BDII/aC etching selectivity dependence on this reduced F/C ratio. High RF/C gases show high BDII etch rates, but BDII/aC etching selectivities are poor. Low RF/C gases show the opposite behavior. The two C<sub>3</sub>HF<sub>5</sub> isomers show etch rate values that similar to C<sub>3</sub>F<sub>6</sub> and higher than the other two hydrogen containing gases. This can be explained by the low hydrogen fraction in precursor structure, which cannot provide enough defluorination to influence the substrate etch rate. The correlation between RF/C and BDII/aC etching selectivity is stronger than between RF/C and BDII etch rate.

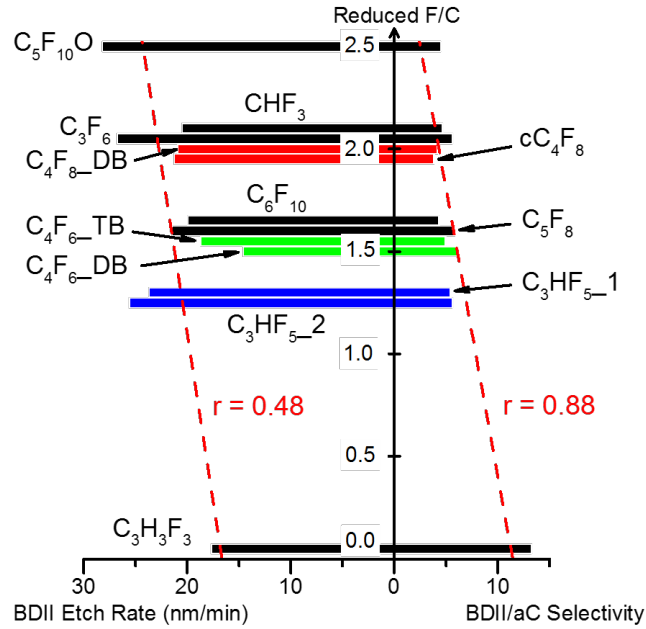


FIG. 2.10 (Color online) BDII etch rate and BDII/aC selectivity vs. precursor reduced F/C ratio. Low reduced F/C ratio gases show high selectivity.

As discussed, the etch rate and BDII/a-C etching selectivity is correlated to the FC deposition rate and RF/C value of the precursor. The etch rates, etching selectivities, and their products for all precursors are shown in Fig. 2.11 in a precursor property map. The precursors with higher FC deposition rates show lower etch rates. Low RF/C precursors show high selectivity, which can be attributed to hydrogen-induced defluorination of FC films. The rectangular areas shown are the products of etch rate and BDII/a-C etching selectivity which allows to evaluate both etch rate and selectivity.

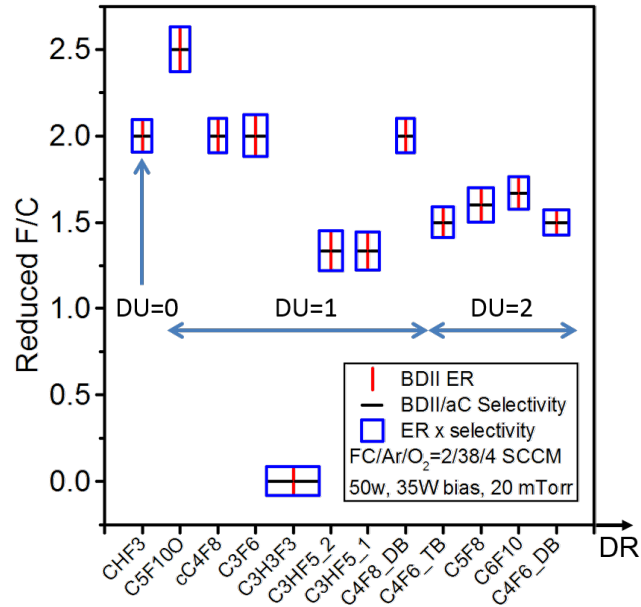


FIG. 2.11 (Color online) BDII ER (perpendicular bar), BDII/aC selectivity (horizontal bar), and the product of ER and selectivity (rectangular area) are shown in the precursor property (reduced F/C vs. DR) map.

### 2.2.3 Low-k sidewall O<sub>2</sub> protection dependence of Precursor

During plasma etching of low-k based structures, low-k sidewall (SW) damage by oxygen in the etching gas mixture is an issue. Higher sidewall deposition rates of FC films are expected to reduce SW ULK damage. A homemade gap structure compatible with *in situ* ellipsometry measurement was used to characterize the sidewall profile behavior under different plasma conditions. The gap structure blocks direct ion bombardment from the plasma, and allows only radicals to reach the substrate.<sup>2.28, 2.29, 2.41</sup> This is similar to the plasma environment on the sidewall of the patterned trench. It is well known that O<sub>2</sub> plasma will damage the low-k dielectric and increase the dielectric constant.<sup>2.42, 2.43</sup> Therefore, pure O<sub>2</sub> plasma are used in this simulated sidewall condition to evaluate low-k damage introduction, Fig. 2.12 (a).

The *in situ* ellipsometry trajectory continuously moved to the bottom left in delta-psi space. This change can be interpreted as a removal of material caused by low-k materials damage.

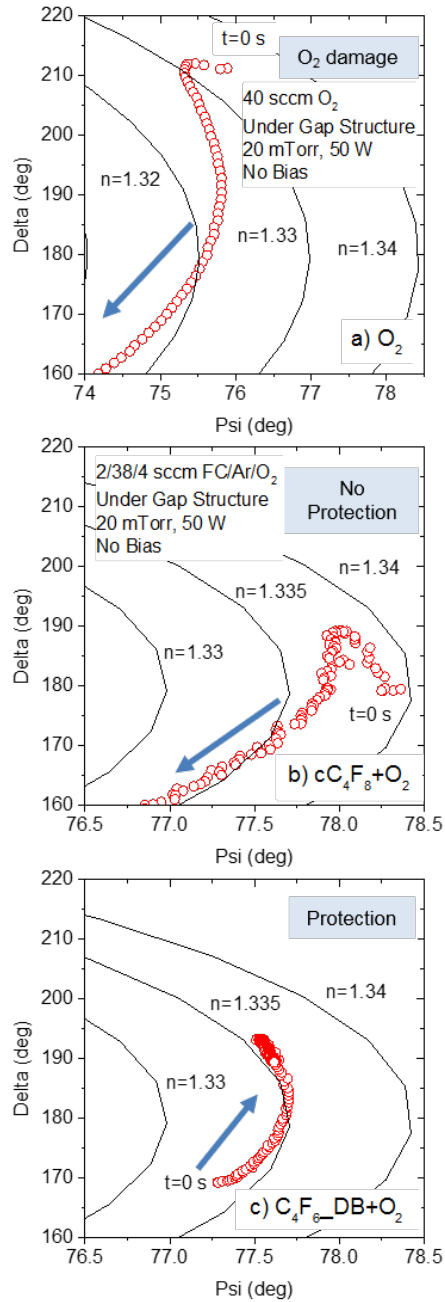


FIG. 2.12 (Color online) *In situ* ellipsometric measurements of BDII simulated sidewall modification with: a)  $O_2$  plasma, b) Ar/ $cC_4F_8/O_2$  plasma, and c)

Ar/C<sub>4</sub>F<sub>6</sub>\_DB/O<sub>2</sub> plasma. Ellipsometric models with different refractive indexes are also shown.

The authors applied this method to evaluate plasma damage for etching gas mixtures of all gas precursors studied. Two major types of ellipsometry trajectories were observed for all precursor gases. For DU = 0 and 1 gases (except C<sub>3</sub>H<sub>3</sub>F<sub>3</sub>), e.g. cC<sub>4</sub>F<sub>8</sub>, the ellipsometry trails are similar as seen for pure O<sub>2</sub> plasma, indicative of similar damage of the low-k dielectric material under these sidewall-like testing conditions, Fig. 2.12 (b). This suggested that these kinds of gaseous precursors do not provide protection from O<sub>2</sub> damage.

On the other hand, for DU = 2 precursors, e.g. C<sub>4</sub>F<sub>6</sub>\_DB, the ellipsometry data showed a different trend, moving to the top right of delta-psi space, and saturating after a certain time, Fig. 2.12 (c). This result can be interpreted by the formation of a self-limited FC film on the low-k material surface. This film was sufficiently thick to protect the BDII material from oxygen damage by blocking the diffusion of O atoms into the pores of the low-k material.

C<sub>3</sub>H<sub>3</sub>F<sub>3</sub> behaved differently from all the other FC precursors. A thickness loss and strong surface modification were seen, and may be explained by surface hydrogen incorporation due to high hydrogen fraction in precursor structure.

The change in delta after 600 s plasma exposure allows to compare the sidewall treatment for different precursors. A positive change in delta indicates that the low-k sidewall was protected from O<sub>2</sub> damage by a FC film, and vice versa. Figure 2.13 shows that the precursor gases with DU=2 showed protective behavior. Low k damage involves a competition between FC deposition and modification of the

low k material (material damage) on sidewall. For highly polymerizing gases (DU=2), the FC deposition dominates this competition, and deposits a layer on the sidewall that protects the material from O<sub>2</sub> damage.

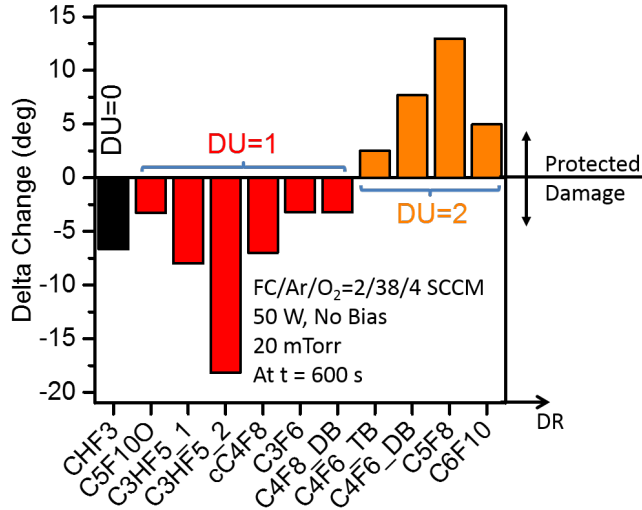


FIG. 2.13 (Color online) Delta changed of simulated BDII sidewall ellipsometry data at 600 s vs. precursor deposition rate.

### 2.3 SUMMARY AND CONCLUSIONS

In this work, the authors evaluated various FC/HFC precursor molecular parameters with regard to CF<sub>2</sub> emission, FC film plasma deposition, low-k material etching, and low-k sidewall damage. For FC film deposition, both the gas precursor CF<sub>2</sub> fraction and the number of weak bonds are important. The CF<sub>2</sub> fraction directly determines the CF<sub>2</sub> density in plasma gas phase. The weak bonds are preferentially broken in the plasma, and their number controls the abundance of dangling bonds available for film growth. This factor makes a dominant contribution to the deposition rate. The deposited FC film surface CF<sub>2</sub> was seen to relate to a combination of CF<sub>2</sub> fraction in the precursor gas and the FC film formation rate. This can be explained by retaining precursor structural aspects as film damage by ion bombardment is reduced

for higher FC film formation rates. Low-k etching rates measured for different precursors agree with the FC consumption model, which suggests that highly polymerizing gases have lower etching rates, due to more energy and etchant dissipation in the relatively thicker steady state FC film formed at the substrate surface. The FC films deposited by hydrogen containing gases show higher crosslinking degrees and lower F/C ratios, resulting in lower material etch rates. The reduced F/C ratio was shown useful for evaluating etching properties of hydrogen and oxygen containing FC precursors. Highly polymerizing gases with a DU of two were shown to protect the low-k material sidewall from oxygen-related damage.

#### **ACKNOWLEDGMENTS**

The authors gratefully acknowledge the financial support of this work by Air Liquide.

The authors thank Dr. N. Lyon, Dr. E. Bartis, D. Metzler, A. Knoll, P. Luan, A.

Pranda and M. Amin for helpful discussions and collaboration.

## Chapter 3: Fluorocarbon Based Atomic Layer Etching of $\text{Si}_3\text{N}_4$ and Etching Selectivity of $\text{SiO}_2$ over $\text{Si}_3\text{N}_4$

*Journal of Vacuum Science & Technology A: Vacuum, Surfaces, and Films* 34 (4), 041307 (2016).

C Li, D. Metzler, C. S. Lai, E. A. Hudson, and G. S. Oehrlein

### ABSTRACT

Angstrom-level plasma etching precision is required for semiconductor manufacturing of sub-10 nm critical dimension features. Atomic layer etching (ALE), achieved by a series of self-limited cycles, can precisely control etching depths by limiting the amount of chemical reactant available at the surface. Recently,  $\text{SiO}_2$  ALE has been achieved by deposition of a thin (several Angstroms) reactive fluorocarbon (FC) layer on the material surface using controlled FC precursor flow and subsequent low energy  $\text{Ar}^+$  ion bombardment in a cyclic fashion. Low energy ion bombardment is used to remove the FC layer along with a limited amount of  $\text{SiO}_2$  from the surface. In the present article, we describe controlled etching of  $\text{Si}_3\text{N}_4$  and  $\text{SiO}_2$  layers of one to several Angstroms using this cyclic ALE approach.  $\text{Si}_3\text{N}_4$  etching and etching selectivity of  $\text{SiO}_2$  over  $\text{Si}_3\text{N}_4$  were studied and evaluated with regard to the dependence on maximum ion energy, etching step length (ESL), FC surface coverage, and precursor selection. Surface chemistries of  $\text{Si}_3\text{N}_4$  were investigated by x-ray photoemission spectroscopy (XPS) after vacuum transfer at each stage of the ALE process. Since  $\text{Si}_3\text{N}_4$  has a lower physical sputtering energy threshold than  $\text{SiO}_2$ ,  $\text{Si}_3\text{N}_4$  physical sputtering can take place after removal of chemical etchant at the end of each cycle for relatively high ion energies.  $\text{Si}_3\text{N}_4$  to  $\text{SiO}_2$  ALE etching selectivity was observed for these FC depleted conditions. By optimization of the ALE process parameters, e.g. low ion energies, short

ESLs, and/or high FC film deposition per cycle, highly selective SiO<sub>2</sub> to Si<sub>3</sub>N<sub>4</sub> etching can be achieved for FC accumulation conditions, where FC can be selectively accumulated on Si<sub>3</sub>N<sub>4</sub> surfaces. This highly selective etching is explained by a lower carbon consumption of Si<sub>3</sub>N<sub>4</sub> as compared to SiO<sub>2</sub>. The comparison of C<sub>4</sub>F<sub>8</sub> and CHF<sub>3</sub> only showed a difference in etching selectivity for FC depleted conditions. For FC accumulation conditions, precursor chemistry has a weak impact on etching selectivity. Surface chemistry analysis shows that surface fluorination and FC reduction take place during a single ALE cycle for FC depleted conditions. A fluorine rich carbon layer was observed on the Si<sub>3</sub>N<sub>4</sub> surface after ALE processes for which FC accumulation takes place. The angle resolved (AR)-XPS thickness calculations confirmed the results of the ellipsometry measurements in all cases.

### 3.1 INTRODUCTION

Angstrom level precision processes are required to continue shrinking the dimensions of semiconductor devices below the 10 nm critical dimension.<sup>3.1-3.3</sup> Atomic layer deposition (ALD) has been established as early as 1977 by Suntola and Antson<sup>4</sup> and is widely applied in industrial fabrication.<sup>3.5-3.8</sup> Its counterpart, atomic layer etching (ALE) is still under development.<sup>3.9-3.11</sup> Recently fluorocarbon (FC) assisted ALE has been shown to have potential in the application of etching Si based materials. The theoretical concept and simulations were first described by Rauf *et al* in 2007<sup>3.12</sup> and Agarwal *et al* in 2009<sup>3.13</sup>, which indicated the possibility to achieve atomic layer level etching and selectivity for Si and SiO<sub>2</sub>. Metzler *et al* experimentally realized controllable SiO<sub>2</sub> ALE in 2013 using a highly controllable Ar/C<sub>4</sub>F<sub>8</sub> inductively coupled plasma (ICP) system along with *in-situ* etching depth measurements.<sup>3.14, 3.15</sup> This FC assisted ALE method has been further evaluated, expanded to etching of Si and Si<sub>3</sub>N<sub>4</sub>, and selectivity optimization e.g. SiO<sub>2</sub> over Si and Si<sub>3</sub>N<sub>4</sub> is of interest.<sup>3.16-3.18</sup>

Si<sub>3</sub>N<sub>4</sub> is a commonly used etch stop layer or spacer in the fabrication of certain damascene and self-aligned contact (SAC) structures, where high etching selectivity is required. For example, SAC structure etching requires high etching selectivity of SiO<sub>2</sub> over Si<sub>3</sub>N<sub>4</sub> to maintain the Si<sub>3</sub>N<sub>4</sub> spacer after SiO<sub>2</sub> removal<sup>3.19</sup>, Si<sub>3</sub>N<sub>4</sub> mask material plasma stripping after local oxidation of silicon (LOCOS) needs Si<sub>3</sub>N<sub>4</sub> over SiO<sub>2</sub> selectivity to avoid damage to the pad oxide.<sup>3.20</sup> ALE may offer the possibility to achieve atomic layer level SiO<sub>2</sub> etching precision along with SiO<sub>2</sub> to

Si<sub>3</sub>N<sub>4</sub> etching selectivity. The authors have examined this objective in the present work.

This article is organized as follows: in the first part, the authors extended the FC depleted ALE from SiO<sub>2</sub> to Si<sub>3</sub>N<sub>4</sub>, and compared Si<sub>3</sub>N<sub>4</sub> ALE results to those obtained with SiO<sub>2</sub>. In the second part, the authors optimized the ALE process for FC accumulation conditions which enabled high SiO<sub>2</sub> to Si<sub>3</sub>N<sub>4</sub> etching selectivity. The impact of maximum ion energy, etching step length (ESL), FC film thickness and precursor gas were evaluated. Finally, Si<sub>3</sub>N<sub>4</sub> surface chemistry analysis was conducted for both FC depleted and accumulation conditions and will be described.

### 3.2 EXPERIMENTAL

The experiments were performed in an inductively coupled plasma (ICP) reactor excited at 13.56 MHz. The substrate can be biased at 3.7 MHz. The ion energy distribution can be found in the previous work.<sup>3,21</sup> The base pressure achieved before processing was in the  $1 \times 10^{-7}$  Torr range and the temperature of the samples (25 x 25 mm<sup>2</sup>) was stabilized at 10 °C by substrate backside cooling water circulation during plasma processing. Using SiO<sub>2</sub>-Si<sub>3</sub>N<sub>4</sub>-SiO<sub>2</sub> multi-layer stacks on a Si substrate enables precise evaluation of materials etching selectivity, self-limitation, and material modification by *in-situ* ellipsometry measurements ( $\lambda = 632.8$  nm). The Si<sub>3</sub>N<sub>4</sub> studied in this work is deposited by plasma-enhanced chemical vapor deposition (PECVD). The top SiO<sub>2</sub> layer was thinned from 30 nm to about 5 nm by a 1 % dilute HF solution to reduce overall processing time. The thicknesses of the other layers are 25 nm bottom SiO<sub>2</sub> and 25 nm Si<sub>3</sub>N<sub>4</sub> in between the two oxide layers. The

samples were loaded using a load-lock chamber after performing oxygen plasma cleaning and Ar plasma pre-conditioning of the main ALE chamber. This served to keep chamber conditions prior to processing as consistent as possible. The plasma operating conditions were 50 sccm Ar carrier gas flow with periodic 2 sccm fluorocarbon precursor gas injection. The processing pressure was kept at 10 mTorr by a butterfly valve in the pumping line. 200 W source power was applied for all ALE experiments. The ratio of etched SiO<sub>2</sub> thickness per cycle over etched Si<sub>3</sub>N<sub>4</sub> thickness per cycle is referred to as SiO<sub>2</sub> to Si<sub>3</sub>N<sub>4</sub> etching selectivity.

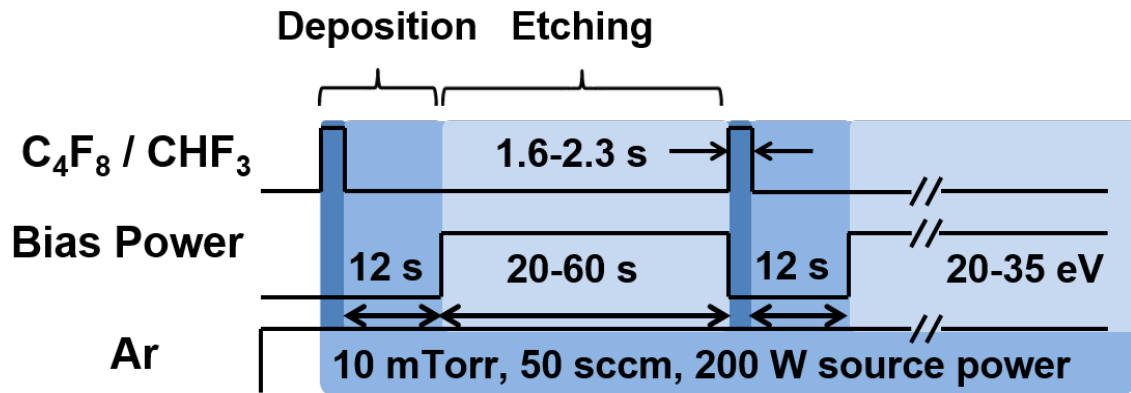


FIG. 3.1 (Color online) Experimental sequence schematic for FC based ALE. The ALE experiment was conducting with a continuous Ar plasma and repeating ALE cycles. One ALE cycle includes an unbiased deposition step and a low energy ion bombardment etching step. A short precursor injection occurs at the beginning of each deposition step. The injection time was varied in order to achieve the desired FC deposition thickness. The duration of the etching step is referred to as etching step length.

The ALE experiments were performed using the standard SiO<sub>2</sub> ALE procedure described in reference 1 and schematically shown in Fig. 3.1. The ALE

process was conducted using a continuous Ar plasma and repeated ALE cycles. Each ALE cycle includes an unbiased FC deposition step and a low energy ion bombardment etching step. A short FC precursor injection takes place at the beginning of each deposition step. The injection time was varied to achieve the desired deposition thicknesses. After the precursor pulse, 12 s of unbiased Ar plasma ensured that all gaseous FC precursor was exhausted from the process chamber. During the etching step, bias power was employed for low energy ion bombardment. Different maximum ion energies (20 to 35 eV), FC film thicknesses (4 to 11 Å), and etching step lengths (20 to 60 s) were explored using C<sub>4</sub>F<sub>8</sub> and CHF<sub>3</sub> precursors. Note: For the sake of convenience, we only refer to this maximum ion energy in the following, and it should be understood that this refers to a distribution of ion energies. After processing, selected samples were transferred under vacuum to a Vacuum Generators ESCALAB MK II surface analysis system for X-ray Photoelectron Spectroscopy (XPS) measurements. High resolution scans of the Si2p, C1s, O1s, N1s and F1s binding energy regions were obtained at 20 eV pass energy at an electron take-off angle of 90° and 20° with respect to the sample surface. The spectra were fitted using least-squares fitting routines with 70/30 % Gaussian/Lorentzian line shapes at fixed full width at half maximum (FWHM) for each spectrum after Shirley background subtraction.

### 3.3 RESULTS AND DISCUSSION

#### 3.3.1 Continuous wave (CW) plasma etching and ellipsometry optical model of $\text{Si}_3\text{N}_4$ stack sample

An exemplary ellipsometry trajectory for Ar/ $\text{C}_4\text{F}_8$  conventional continuous wave (CW) plasma etching of the  $\text{Si}_3\text{N}_4$  stack sample together with the ellipsometry simulation lines are shown in Fig. 2. In this process, a 50/2 sccm gas flow of Ar/ $\text{C}_4\text{F}_8$  mixture, 10 mTorr process pressure and 200 W source power were employed. The maximum ion energy was controlled to be 85 eV. A sharp turn in the ellipsometric Delta-Psi trajectory at the Psi value around  $15^\circ$  and  $25^\circ$  can be seen as the material changes from top  $\text{SiO}_2$  to  $\text{Si}_3\text{N}_4$ , and finally to bottom  $\text{SiO}_2$ , consistent with optical simulations.

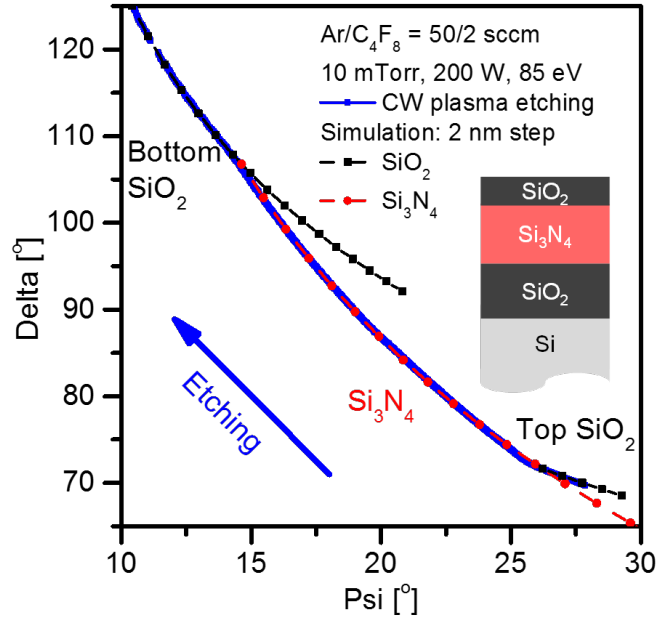


FIG. 3.2 (Color online) Exemplary ellipsometry trajectory for a  $\text{Si}_3\text{N}_4$  stack sample, using an Ar/ $\text{C}_4\text{F}_8$  CW plasma etch. Colored, dashed lines show the optical model simulation.

The  $\text{Si}_3\text{N}_4$  ALE in-situ ellipsometry data was interpreted using a two-layer optical model, which consists of a fixed bottom  $\text{SiO}_2$  layer and a varying top overlayer, representing a combination of  $\text{Si}_3\text{N}_4$ , fluorinated  $\text{Si}_3\text{N}_4$  (SiNF), and FC (Fig. 3.3). This overlayer optical model provides a good approximation of the data, since the optical properties of FC, SiNF and  $\text{Si}_3\text{N}_4$  are similar, and optical refractive index differences of the FC and SiNF play an insignificant role due to the large thickness differences of the layers involved (the thicknesses of FC and SiNF layers is several Å, whereas the  $\text{Si}_3\text{N}_4$  layer thickness investigated is about 20 nm). Indeed, the change of FC thickness given by this overlayer ellipsometry model was confirmed and validated by angle resolved-XPS (AR-XPS) analysis. This will be discussed later when describing the surface chemistry data.

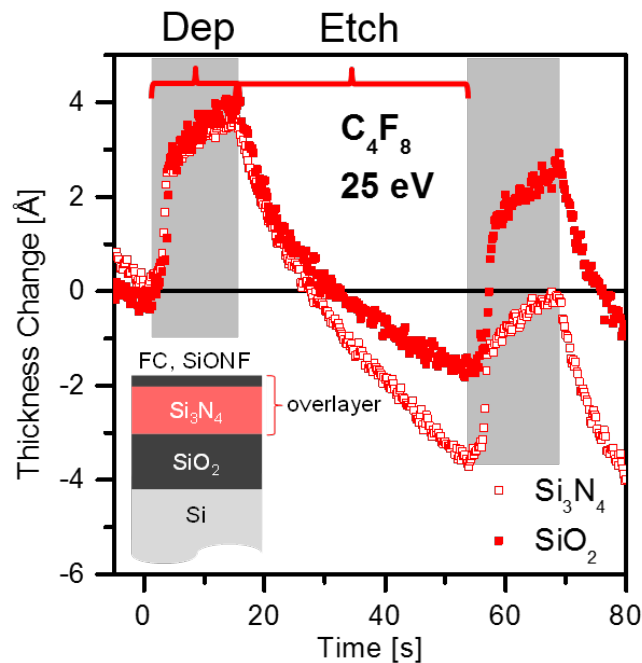


FIG. 3.3 (Color online) Thickness changes of  $\text{Si}_3\text{N}_4$  and  $\text{SiO}_2$  during a single cycle for a 4 Å FC deposition, 25 eV maximum ion energy and 40 s etching step length. The

precursor pulse is injected at the beginning of the deposition step. Twelve seconds after the pulse ends, the bias potential is applied marking the beginning of the etching step. Etch rates reduce during etching step due to FC depletion.

### 3.3.2 Si<sub>3</sub>N<sub>4</sub> ALE in FC depleted condition

With the success of controlled FC based ALE of SiO<sub>2</sub><sup>3,15</sup>, similar experiments were conducted for Si<sub>3</sub>N<sub>4</sub>. To achieve FC depleted conditions, a 40 s long etching step with maximum ion energies of 25 eV and 30 eV was employed. Since the physical sputtering energy threshold energy of SiO<sub>2</sub> ( $\approx 50$  eV<sup>3,13</sup>) is higher than the maximum ion energy applied, self-limited etching can be achieved for SiO<sub>2</sub> when no chemical etchant is present on the SiO<sub>2</sub> surface at the end of the etching step. A similar Si<sub>3</sub>N<sub>4</sub> thickness evolution was observed as for SiO<sub>2</sub> (Fig. 3.3). During the deposition step a thin FC film was deposited on the surface. Once the bias power was applied during the etching step, a thickness reduction was observed with reducing etch rates (ER), indicating that the available etchant for chemical assisted etching was reduced as a function of time, i.e. the FC was being depleted on the surface. However, since the Si<sub>3</sub>N<sub>4</sub> physical sputtering energy threshold ( $\approx 20$  eV<sup>3,22</sup>) is lower than for SiO<sub>2</sub>, a small amount of physical sputtering is still seen for Si<sub>3</sub>N<sub>4</sub> after chemical etchant (FC) depletion. This leads to more thickness removal for Si<sub>3</sub>N<sub>4</sub> than SiO<sub>2</sub> for each ALE cycle for these conditions.

As for SiO<sub>2</sub>, FC depleted Si<sub>3</sub>N<sub>4</sub> ALE at 25 or 30 eV maximum ion energy using 40 s ESL also shows a strong impact of FC film thickness and maximum ion energy (Fig. 3.4 (a)). A higher FC film thickness provides more chemical etchant and allows a higher amount of material to be removed during a cycle. Next to FC film

thickness, maximum ion energy plays an important role for these FC depleted conditions. When comparing 30 eV to 25 eV, both SiO<sub>2</sub> and Si<sub>3</sub>N<sub>4</sub> were etched more for the higher maximum ion energy during an ALE cycle, due to more energy being available for FC assisted chemical etching.

The ratio of thickness etched per cycle of both materials gives the SiO<sub>2</sub> to Si<sub>3</sub>N<sub>4</sub> selectivity and is shown in Fig. 3.4 (b). Due to the lower physical sputtering energy threshold for Si<sub>3</sub>N<sub>4</sub> compared to SiO<sub>2</sub>, more Si<sub>3</sub>N<sub>4</sub> was etched than SiO<sub>2</sub> for FC depleted ALE conditions and resulted in a SiO<sub>2</sub> to Si<sub>3</sub>N<sub>4</sub> etching selectivity of less than one. It is difficult to achieve SiO<sub>2</sub> to Si<sub>3</sub>N<sub>4</sub> etching selectivity for these FC depleted conditions owing to the fact that the Si<sub>3</sub>N<sub>4</sub> physical sputtering energy threshold is smaller than that of SiO<sub>2</sub>.

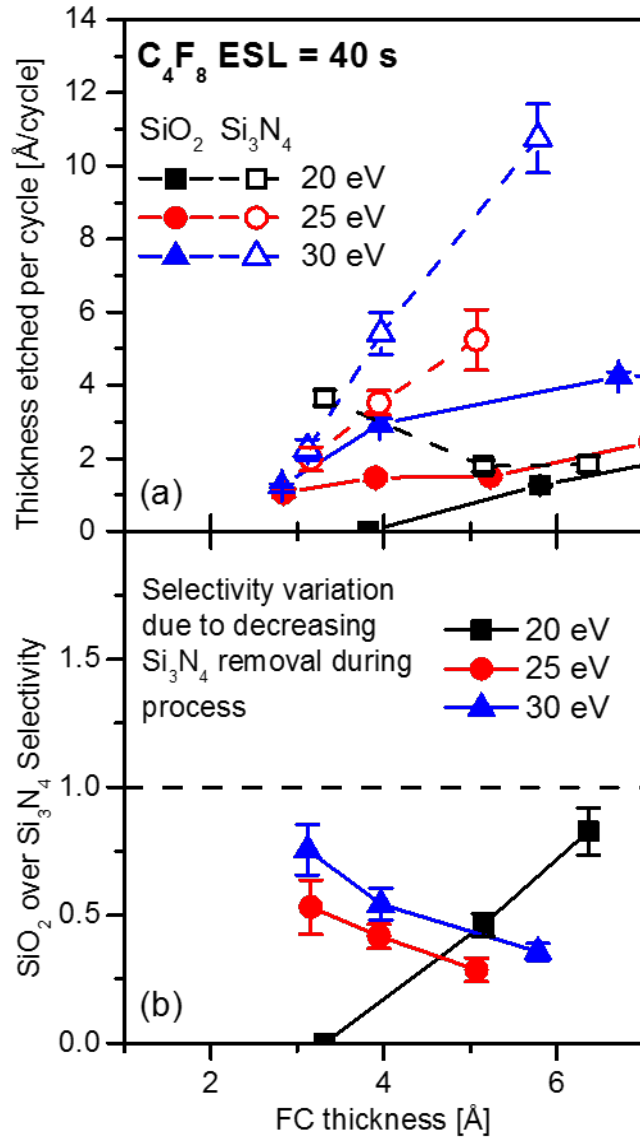


FIG. 3.4. (Color online) (a) Thickness etched per cycle for Si<sub>3</sub>N<sub>4</sub> and SiO<sub>2</sub> as a function of maximum ion energy and FC thickness. (b) SiO<sub>2</sub> to Si<sub>3</sub>N<sub>4</sub> selectivity, calculated by the thickness etched ratio in one cycle. In FC depleted conditions (25 and 30 eV), a higher maximum ion energy and thicker FC thickness enables more material etching. In FC accumulation conditions (20 eV), a thicker FC film reduces Si<sub>3</sub>N<sub>4</sub> etching, while SiO<sub>2</sub> etching is enhanced.

### 3.3.3 SiO<sub>2</sub> to Si<sub>3</sub>N<sub>4</sub> selectivity optimization by FC accumulated conditions

Due to the higher physical sputtering of Si<sub>3</sub>N<sub>4</sub>, FC depleted conditions cannot provide a selective etching of SiO<sub>2</sub> over Si<sub>3</sub>N<sub>4</sub> (Fig. 3.5 (a)). However, the chemical composition difference of Si<sub>3</sub>N<sub>4</sub> and SiO<sub>2</sub> favors a lower carbon consumption on Si<sub>3</sub>N<sub>4</sub> surfaces due to the differences in bond strengths, substrate stoichiometry, volatility of the reaction products, and etc<sup>3,19</sup>. This carbon consumption difference is the basis of selectively etching of SiO<sub>2</sub> over Si<sub>3</sub>N<sub>4</sub> in conventional continuous wave (CW) plasma etching.<sup>3,19</sup> In CW plasma etching, a relatively thicker steady state FC film is formed on Si<sub>3</sub>N<sub>4</sub> compared to SiO<sub>2</sub>, which strongly reduces the Si<sub>3</sub>N<sub>4</sub> etch rate (ER) by a higher energy and etchant consumption in the FC layer. Using the concept of carbon consumption difference, an ALE SiO<sub>2</sub> to Si<sub>3</sub>N<sub>4</sub> selective etching regime can be achieved by process parameter optimization. FC can be accumulated on Si<sub>3</sub>N<sub>4</sub> surfaces, thus protecting Si<sub>3</sub>N<sub>4</sub> from ion bombardment induced chemical and physical etching<sup>3,23</sup> (Fig. 3.5 (b)). In the following, the detailed impact of each ALE parameter, e.g. maximum ion energy, etching step length and FC film thickness will be evaluated. A C<sub>4</sub>F<sub>8</sub> and CHF<sub>3</sub> precursor comparison will also be addressed.

#### 3.3.3.1 Maximum ion energy impact on SiO<sub>2</sub> to Si<sub>3</sub>N<sub>4</sub> selectivity

The first processing parameter to be described is maximum ion energy. When the maximum ion energy is reduced from 25 to 20 eV, the ellipsometric Delta-Psi trajectory indicates a strong deviation from the Si<sub>3</sub>N<sub>4</sub> simulation line after etching the top SiO<sub>2</sub>. This can be explained by a FC layer accumulating on the Si<sub>3</sub>N<sub>4</sub> surface (Fig. 3.6 (a)). The detailed thickness evolutions during exemplary ALE cycle for Si<sub>3</sub>N<sub>4</sub> and SiO<sub>2</sub> are shown in Fig. 3.6 (b). For low maximum ion energy conditions of 20 eV, the

ER is relatively constant, suggesting that the available etchant on the surface is not depleted during the etching step. The FC ER in the low maximum ion energy condition is too low to remove all the FC deposited on the surface, which leaves an increasingly thicker FC layer on top of the  $\text{Si}_3\text{N}_4$  substrate surface. Comparing the etching performance at 20 eV maximum ion energy (Fig. 3.4), as the deposited FC thickness increase, a reduction of thickness etched per cycle is seen for  $\text{Si}_3\text{N}_4$ . As a result, the  $\text{SiO}_2$  to  $\text{Si}_3\text{N}_4$  selectivity increases with FC thickness in the maximum ion energy of 20 eV condition. This improvement of the etching selectivity indicates the potential to achieve high  $\text{SiO}_2$  to  $\text{Si}_3\text{N}_4$  etching selectivity for low maximum ion energy conditions. In these situations, the FC layers will not be fully depleted on the  $\text{Si}_3\text{N}_4$  surface. However, the best selectivity achieved with these conditions is still below one and the  $\text{SiO}_2$  ER is fairly low for such low maximum ion energy process conditions.

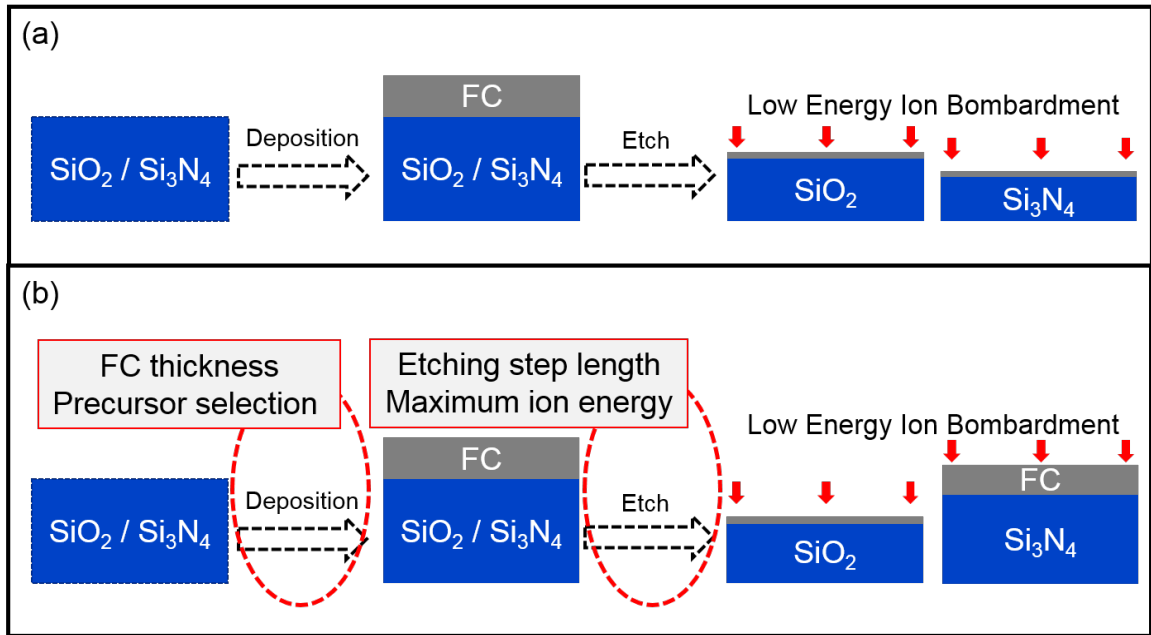


FIG. 3.5 (Color online) Schematics illustrating (a) FC depleted conditions, which allows  $\text{Si}_3\text{N}_4$  to  $\text{SiO}_2$  etching selectivity, and (b) FC accumulation conditions, in which  $\text{SiO}_2$  to  $\text{Si}_3\text{N}_4$  etching selectivity can be achieved.

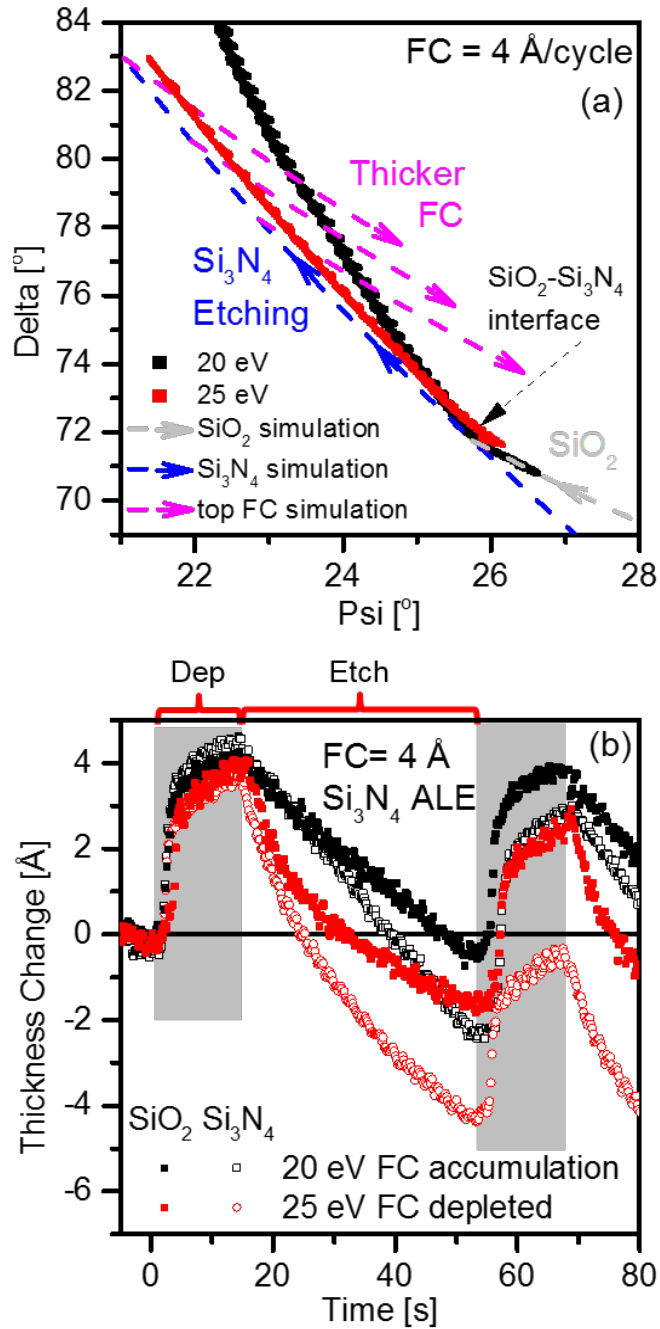


FIG. 3.6 (Color online) Maximum ion energy impact on  $\text{Si}_3\text{N}_4$  ALE behaviors. (a) *in-situ* ellipsometry trajectory in Delta-Psi space. Maximum ion energy of 20 eV

condition shows a strong deviation from Si<sub>3</sub>N<sub>4</sub> simulation line, which can be explained by FC accumulation on top of Si<sub>3</sub>N<sub>4</sub> surface. (b) Thickness changes of Si<sub>3</sub>N<sub>4</sub> during a single cycle for two maximum ion energies.

### 3.3.3.2 Etching step length impact on SiO<sub>2</sub> to Si<sub>3</sub>N<sub>4</sub> selectivity

The ALE cycles consist of separate deposition and etching steps. The etching step length (ESL), or ion bombardment time, is a key parameter that controls the performance of the ALE process. In the following, the impact of ESL on the Si<sub>3</sub>N<sub>4</sub> and SiO<sub>2</sub> ALE process at 25 eV maximum ion energy and 4 Å FC deposition will be discussed. The ESLs tested were 20, 30, 40 and 60 s.

For an ESL longer than 20 s, the ALE process shows a strongly decreasing ER during each etching step, similar to other FC depleted conditions (25 and 30 eV ion energies discussed in section B). With an ESL of 20 s, this time dependent ER reduction is much less than for other conditions. FC film accumulation takes place for 20 s ESL. This suggests that at least 20 s ESL is required to mostly deplete the deposited 4 Å FC film during each ALE cycle when employing 25 eV.

A noticeable time dependent ER was observed for etching step for both SiO<sub>2</sub> and Si<sub>3</sub>N<sub>4</sub>. The ERs during the first and last 3 s of etching step were obtained and are referred to as ER<sub>initial</sub> and ER<sub>final</sub>, respectively. The ERs for both materials were decreasing during the etching step from ER<sub>initial</sub> to ER<sub>final</sub>. This is shown in Fig. 7 (a). It was found that the SiO<sub>2</sub> ER was initially higher than the Si<sub>3</sub>N<sub>4</sub> ER due to the higher FC film consumption for SiO<sub>2</sub>. However, the ER for SiO<sub>2</sub> decreased faster, becoming lower than for Si<sub>3</sub>N<sub>4</sub> at the end of the cycle, caused by the physical sputtering energy threshold difference. This behavior indicates that the ALE process is sensitive to substrate material. It is possible to take advantage of this initial chemical enhanced

etching stage to achieve  $\text{SiO}_2$  to  $\text{Si}_3\text{N}_4$  etching selectivity by shorter ESL. The  $\text{ER}_{\text{initial}}$  is almost unchanged by reducing ESL, since it is the ER of FC on the substrate surface, which mostly depends on maximum ion energy and film thickness. In contrast to the  $\text{ER}_{\text{initial}}$ ,  $\text{ER}_{\text{final}}$  is decreasing with longer ESL due to two reasons. One, for longer etching time, more FC etchant has been used for material removal and less chemical etchant is left on the surface. Second, we observed some surface oxidation at the end of the ion bombardment phase. As the ESL becomes longer, the substrate top surface is slightly oxidized and a silicon oxide-like passivated layer formed, which reduced  $\text{ER}_{\text{final}}$ .

Thicknesses etched per cycle for both  $\text{SiO}_2$  and  $\text{Si}_3\text{N}_4$  are plotted versus ESL in Fig. 3.7 (b). A strong reduction of the thickness removal per cycle is seen for both  $\text{SiO}_2$  and  $\text{Si}_3\text{N}_4$  when the ESL is shorter than 30 s, corresponding to FC accumulated conditions. The ratio of this thickness removal per cycle, i.e.  $\text{SiO}_2$  to  $\text{Si}_3\text{N}_4$  selectivity, was calculated (Fig. 3.7 (c)). Similar to the 20 eV maximum ion energy condition discussed in section B, FC film accumulation condition (20 s ESL) show the highest  $\text{SiO}_2$  to  $\text{Si}_3\text{N}_4$  etching selectivity of about 1.1, while FC depleted conditions seen for longer ESL only show a  $\text{SiO}_2$  to  $\text{Si}_3\text{N}_4$  etching selectivity of about 0.4. The relatively large range of values for 20 s ESL is due to the fact that the etched  $\text{Si}_3\text{N}_4$  thickness variation is relatively large for very small and decreasing  $\text{Si}_3\text{N}_4$  etched thickness per cycle. A shorter ESL weighs more the chemically enhanced etching mechanism for short times and reflects more of the substrate material dependence of the chemically enhanced etch rate, ultimately increasing selectivity. For longer ESL physical sputter rates are emphasized. This result is consistent with the report by Hudson *et al.*<sup>3.23</sup>

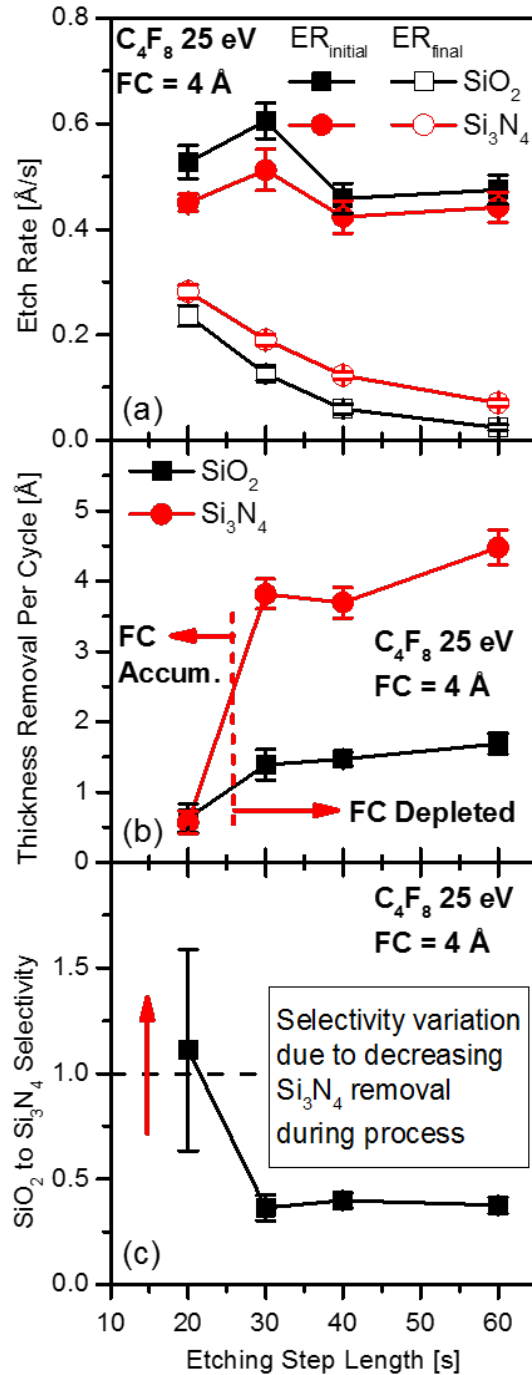


FIG. 3.7 (Color online) Etching step length impact on SiO<sub>2</sub> and Si<sub>3</sub>N<sub>4</sub> ALE using 25 eV maximum ion energy and 4 Å FC deposited per cycle by C<sub>4</sub>F<sub>8</sub>. The dependence of etching step length on (a) initial and final etch rates during one cycle, (b) thickness etched per cycle, and (c) SiO<sub>2</sub> to Si<sub>3</sub>N<sub>4</sub> selectivity, calculated by the thickness etched ratio in one cycle, is shown.

### 3.3.3.3 FC film thickness impact on SiO<sub>2</sub> to Si<sub>3</sub>N<sub>4</sub> selectivity

Further ALE process optimization was conducted with 20 s ESL and a maximum ion energy of 35 eV. This high maximum ion energy accelerates the etching process, and allows to study the impact of FC film thickness over a wider range.

The ER for each condition was evaluated (Fig. 3.8 (a)). It is shown that the ER<sub>initial</sub> is reduced for thicker deposited FC films. This observation suggests that there is a substrate-FC interaction at the beginning of the etching step, accelerating etching. A thicker FC film blocks this interaction and the substrate assisted etching, thus reducing the initial ER. Because of a lower carbon consumption of Si<sub>3</sub>N<sub>4</sub>, this ER reduction is stronger for Si<sub>3</sub>N<sub>4</sub> than SiO<sub>2</sub>. At a FC thickness of about 11 Å, the ER for Si<sub>3</sub>N<sub>4</sub> is fairly constant during a cycle and initially lower than SiO<sub>2</sub>. The thickness removal per cycle (Fig. 3.8 (b)) shows a strong reduction for Si<sub>3</sub>N<sub>4</sub> for FC films thicker than 8 Å. The deposited FC layer cannot be fully removed and is accumulated on the surface, reducing substrate etching. In this FC accumulation condition, the SiO<sub>2</sub> to Si<sub>3</sub>N<sub>4</sub> etching selectivity increased dramatically from less than one to 15 (Fig. 3.8 (c)).

The ellipsometry raw data for various FC film thicknesses are shown in Fig. 3.9. The Ar/CF<sub>4</sub> CW plasma etching trajectory is shown for reference of a trajectory with no to little FC film. In the case of 11 Å FC deposited per cycle, etching slows down at the SiO<sub>2</sub>-Si<sub>3</sub>N<sub>4</sub> interface and a FC layer starts to accumulate on the surface.

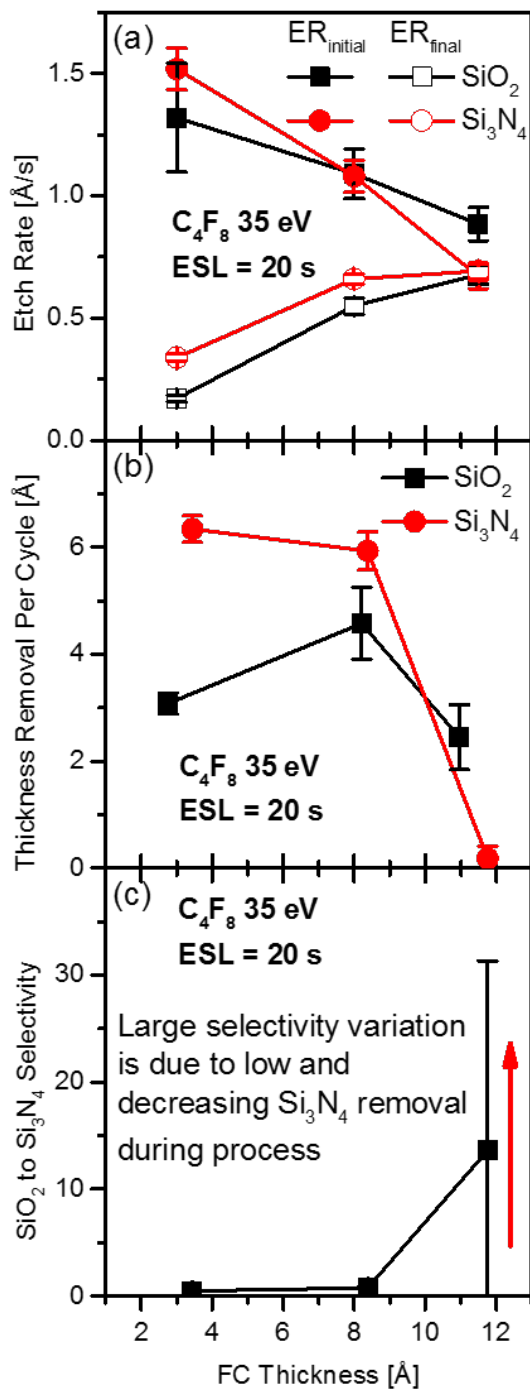


FIG. 3.8 (Color online) FC thickness impact on  $SiO_2$  and  $Si_3N_4$  ALE in the condition of 35 eV maximum ion energy and 20 s ESL using  $C_4F_8$ . (a) Initial and final ERs during one cycle. (b) Thickness etched per cycle. (c)  $SiO_2$  to  $Si_3N_4$  selectivity, calculated by the thickness etched ratio in one cycle.

In summary, SiO<sub>2</sub> to Si<sub>3</sub>N<sub>4</sub> selectivity using Ar/C<sub>4</sub>F<sub>8</sub> plasma atomic layer etching can be achieved for FC accumulation conditions, which are favored for low maximum ion energy, short ESL, and/or thick FC films. These process parameters need to be tuned and coordinated to each other in order to achieve a balance of the FC layer deposition and etching. High SiO<sub>2</sub> to Si<sub>3</sub>N<sub>4</sub> selectivity can be achieved at a critical condition that accumulates FC on Si<sub>3</sub>N<sub>4</sub>.

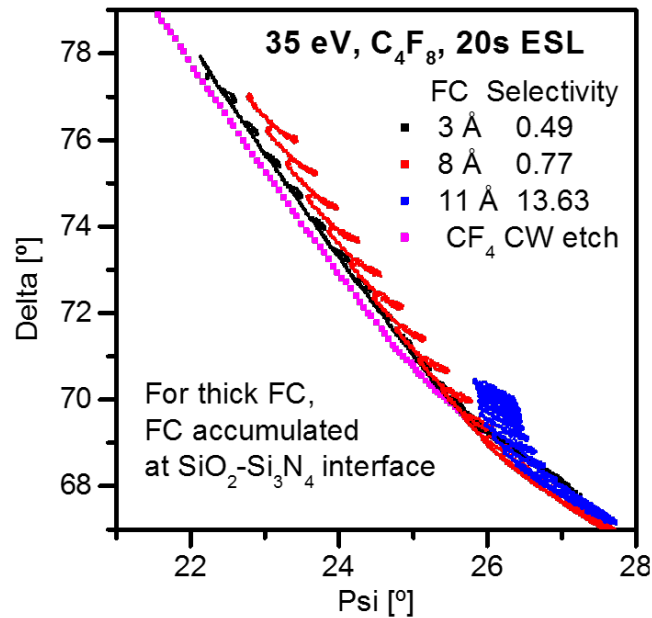


FIG. 3.9 (Color online) *In-situ* ellipsometry trajectory in Delta-Psi space for the condition of 35 eV maximum ion energy and 20 s ESL, with different thicknesses of deposited FC layer achieved by changing the C<sub>4</sub>F<sub>8</sub> pulse time from 1.6 s to 2.3 s. The Ar/CF<sub>4</sub> CW plasma etching trajectory is shown for reference of a sample without FC. In the case of 11.5 Å FC deposited per cycle, etching slows down at the SiO<sub>2</sub>-Si<sub>3</sub>N<sub>4</sub> interface and a FC film starts accumulating.

### 3.3.3.4 Precursor impact on SiO<sub>2</sub> to Si<sub>3</sub>N<sub>4</sub> selectivity

Precursor chemistry allows to directly control surface reactive layer composition and is another important process parameter.<sup>3,24</sup> Next to the conventional

C<sub>4</sub>F<sub>8</sub> precursor gas, SiO<sub>2</sub> and Si<sub>3</sub>N<sub>4</sub> ALE processes were evaluated for CHF<sub>3</sub>. The SiO<sub>2</sub> to Si<sub>3</sub>N<sub>4</sub> etching selectivity for FC depleted and accumulation conditions are shown in Fig. 3.10 for both precursors. For FC depleted conditions, the SiO<sub>2</sub> to Si<sub>3</sub>N<sub>4</sub> etching selectivity achieved by CHF<sub>3</sub> based ALE is lower than for C<sub>4</sub>F<sub>8</sub> based processes (25 and 30 eV maximum ion energy in Fig. 3.10 (a)). This may be related to the deposited reactive layer chemistry. The FC film deposited by CHF<sub>3</sub> at a thickness of about 5 Å provides more available fluorine etchant for substrate etching than C<sub>4</sub>F<sub>8</sub>.<sup>3.16, 3.25</sup> However, a slightly higher SiO<sub>2</sub> to Si<sub>3</sub>N<sub>4</sub> etching selectivity is observed for 20 eV and 40 s ESL FC accumulation conditions for CHF<sub>3</sub> (Fig. 3.10 (a)). Once the FC accumulation is strong enough to stop the Si<sub>3</sub>N<sub>4</sub> etching, the etching selectivity difference between C<sub>4</sub>F<sub>8</sub> and CHF<sub>3</sub> based ALE is negligible (Fig. 3.10 (b)). This observation indicates the thick FC film will protect the Si<sub>3</sub>N<sub>4</sub> layer underneath from etching, and the FC film composition will not be a dominant factor compared to the substrate material chemistry for etching selectivity.

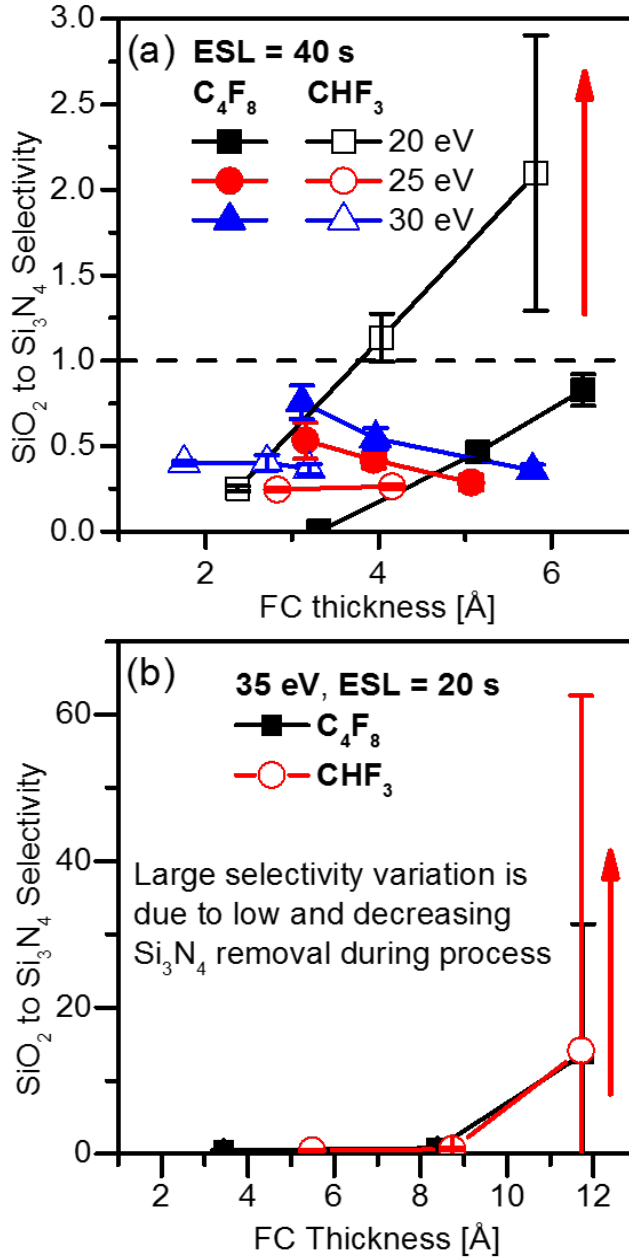


FIG. 3.10 (Color online) C<sub>4</sub>F<sub>8</sub> and CHF<sub>3</sub> comparison on SiO<sub>2</sub> to Si<sub>3</sub>N<sub>4</sub> ALE selectivity for FC depleted conditions and accumulation conditions.

### 3.3.3.5 ALE cycle averaged etch yield calculation

Ion etch yield in tradition CW plasma etching process is defined as the number of substrate atoms removed per incident ion. In the case of cyclic ALE, however, substrate etching is strongly time-dependent. In order to characterize the

process condition impacts on etch yield, the etch yield can be averaged over a cycle and defined as the number of atoms removed per cycle divided by the number of incident ions per cycle. The amount of fluorine per incident ion ( $F/Ar^+$ ) can be calculated from the amount of F in the deposited FC layer per cycle divided by the number of incident ions per cycle. The amount of F in FC layer is calculated by the FC film thickness, F/C ratio measured in XPS, density (estimated by Teflon density), and sample area using Eq. (3.1). Number of incident ion can be calculated by the ion current density (ICD), sample area, ESL and elementary charge. (Eq. (3.2)).

$$F \text{ atom deposited, } n_F = \frac{FC \text{ thickness} \times \text{area} \times \text{density}}{m_F + \frac{m_C}{F/C}} \quad (3.1)$$

$$\text{number of incident ion, } n_{Ar^+} = ICD \times \text{area} \times ESL / e \quad (3.2)$$

Increasing  $F/Ar^+$  ratio corresponds to the increasing chemical reactive etching during an ALE cycle. This ALE cycle averaged etch yield as a function of  $F/Ar^+$  ratio averaged over the same cycle is shown in Figs. 3.11 for (a)  $C_4F_8$  and (b)  $CHF_3$  precursor gases in the condition of 20 to 35 eV ion energies, 20 to 60 s ESLs, and 2 to 11 Å FC film deposition per cycle. Comparing to the etch yields in traditional CW plasma etching<sup>3.26-3.28</sup>, this ALE cycle averaged etch yield shows a much lower value due to no reactive etchant supply during etching step.

For both  $C_4F_8$  and  $CHF_3$  precursors, the cycle averaged etch yields show a similar trend. In the low cycle averaged  $F/Ar^+$  region, the etch yield is limited by the injected reactive etchant, leading to a strong increase in etch yield with higher  $F/Ar^+$ . In this etchant limited region,  $Si_3N_4$  shows a much higher etch yield increase (greater slope) than  $SiO_2$ . This indicates the  $Si_3N_4$  etching is more reactive to fluorine than

SiO<sub>2</sub>. Once the F/Ar<sup>+</sup> ratio increases to a certain value, etch yield will start to saturate and etching is limited by ion bombardment. Additionally, the saturated etch yield is higher for ALE of Si<sub>3</sub>N<sub>4</sub> compared to SiO<sub>2</sub>. This result suggests again that ALE of Si<sub>3</sub>N<sub>4</sub> depends more strongly on the availability of fluorine than SiO<sub>2</sub>, while the limiting factor for etching of SiO<sub>2</sub> is the ion bombardment due to its lower physical sputtering yield.<sup>3.13, 3.22</sup> Since F is deposited to the substrate surface in the form of FC, as the F/Ar<sup>+</sup> ratio increases to a critical value, ion bombardment will be insufficient to remove all the deposited FC. As a result, FC start to accumulate on surface and reduce the etch yield. The x-axis for FC accumulated condition is no longer the F reacted with substrate surface, rather than the amount of F deposited on the surface during an ALE cycle. Higher ion energy enables more FC removal with a given amount of ion bombardment, as a result, the transition point from FC depleted condition to FC accumulation condition shows a higher cycle averaged F/Ar<sup>+</sup> value for higher ion energy conditions. Due to the carbon consumption difference, this transition point varies for different substrate materials. The F/Ar<sup>+</sup> value for Si<sub>3</sub>N<sub>4</sub> transition point is smaller than for SiO<sub>2</sub>, which enables ALE selectivity of SiO<sub>2</sub> over Si<sub>3</sub>N<sub>4</sub>. Compared to C<sub>4</sub>F<sub>8</sub>, CHF<sub>3</sub>-based ALE shows an overall higher etch yield for both materials.

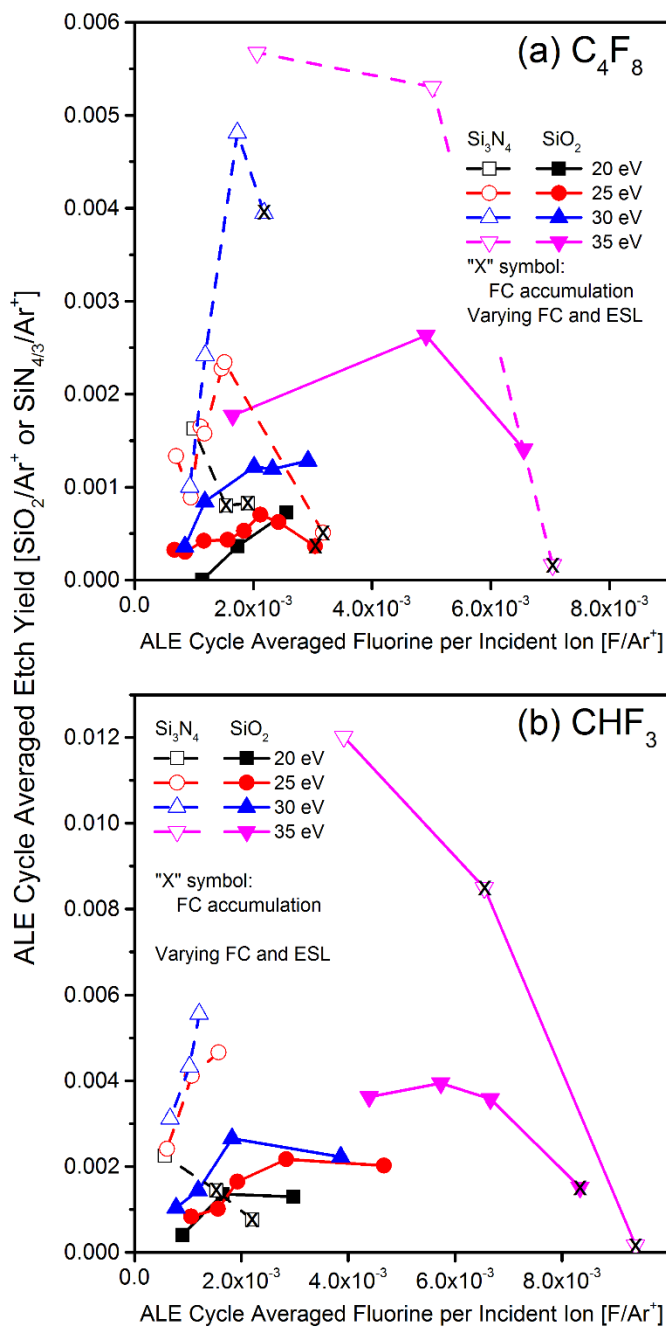


Fig. 3.11 (Color online) ALE cycle averaged etch yield as a function of fluorine per incident ion averaged over the same cycle for (a) C<sub>4</sub>F<sub>8</sub> and (b) CHF<sub>3</sub> precursor gases in the condition of 20 to 35 eV ion energies, 20 to 60 s ESLs, and 2 to 11 Å FC film thicknesses. FC accumulation conditions are marked, and shown with a low cycle averaged etch yield in high F/Ar<sup>+</sup> region.

### 3.3.4 Surface chemistry evaluation

To gain insight on surface chemical changes, selected samples were transferred after Si<sub>3</sub>N<sub>4</sub> ALE processes under vacuum to a Vacuum Generators ESCALAB MK II surface analysis system for X-ray Photoelectron Spectroscopy (XPS) measurements. High resolution spectra of the Si2p, C1s, O1s, N1s and F1s were obtained at 20 eV pass energy at an electron take-off angle of 90° and 20° with respect to the sample surface. In this section, the FC depleted conditions will be discussed first, followed by accumulation conditions.

#### 3.3.4.1 Surface chemistry evolution during a ALE cycle in FC depleted condition

A representative FC depleted condition, which is 25 eV maximum ion energy, 4 Å FC deposited, and 40 s ESL for C<sub>4</sub>F<sub>8</sub> and CHF<sub>3</sub>, was used to study the surface chemistry evolution on Si<sub>3</sub>N<sub>4</sub> surfaces. A series of ALE processes were stopped at different time points during the etching step, *i.e.* 0, 5, 20, and 40 s after completion of a deposition step. The spectra scanned at 90° probe angle for C<sub>4</sub>F<sub>8</sub> after deposition step are shown in Fig. 3.12. The intensities from each spectrum shown is calibrated using the following relative sensitivity factors: Si2p: 0.27, C1s: 0.25, N1s: 0.42, O1s: 0.66, F1s: 1.<sup>3.29</sup>

The Si2p spectra were fitted with two major peaks separated by 1.8 eV,<sup>3.19</sup> corresponding to fluorinated silicon nitride (SiNF) and fluorinated silicon oxide (SiOF). The binding energies were 103 and 104.8 eV, which are shifted from the pristine Si<sub>3</sub>N<sub>4</sub> and SiO<sub>2</sub> binding energy value due to fluorination. The oxygen related silicon peak might originate from remaining top SiO<sub>2</sub> after etching and/or surface Si<sub>3</sub>N<sub>4</sub> oxidation.

The C1s spectra were decomposed in five different peaks corresponding to different chemical carbon bonds<sup>17</sup> (C-C/C-H, C-CF<sub>x</sub>, C-F/C-O, C-F<sub>2</sub>, and C-F<sub>3</sub>). The binding energy of reacted C are fixed at +1.85, +4.05, +6.3, +8.6 eV in relation to C-C, based on analysis of deposited FC films using C<sub>4</sub>F<sub>8</sub>.

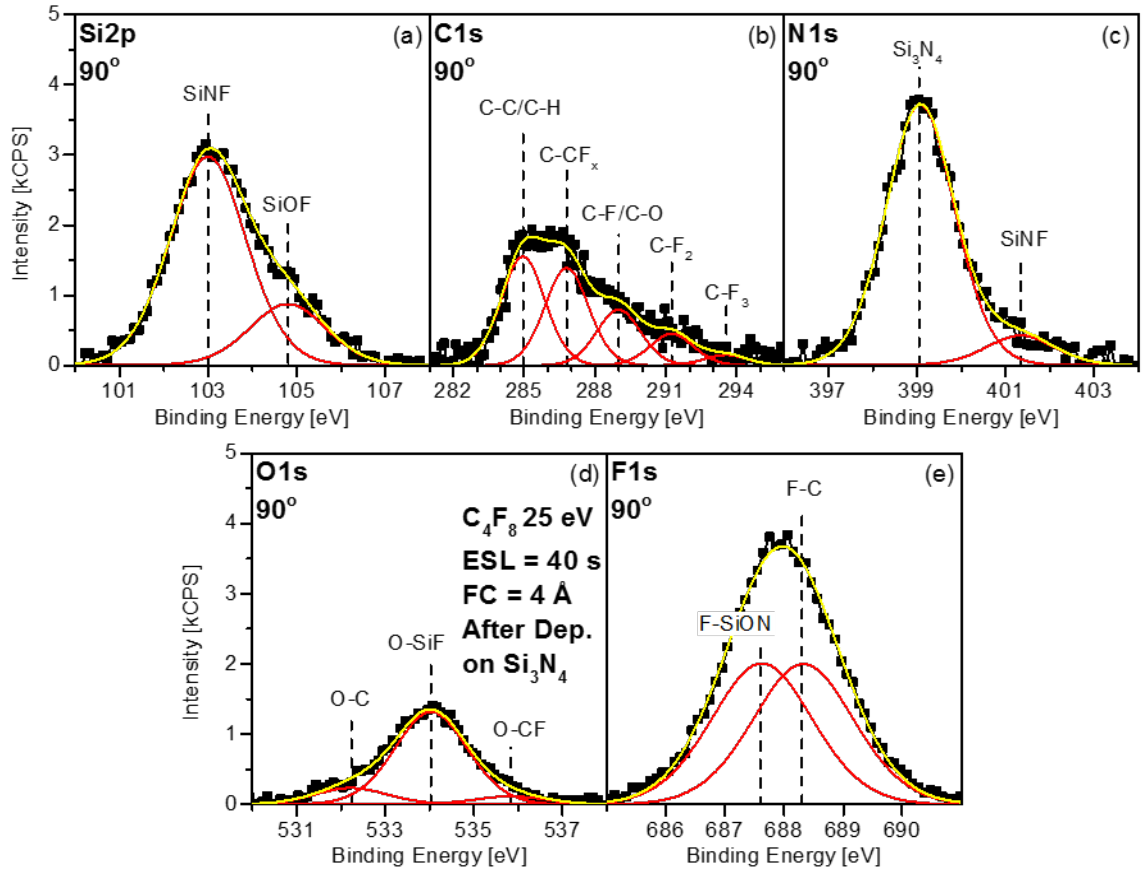


FIG. 3.12. (Color online) 90° Si<sub>3</sub>N<sub>4</sub> XPS of Si2p (a), C1s (b), N1s (c), O1s (d) and F1s (e) spectra scanned at the end of deposition step with 25 eV maximum ion energy, 40 s ESL and 4 Å FC deposited per cycle by C<sub>4</sub>F<sub>8</sub>. The deconvolution is shown for each spectrum. The areas for each moiety are kept consistent across all spectra.

The N1s spectra were fitted to Si<sub>3</sub>N<sub>4</sub> and fluorinated Si<sub>3</sub>N<sub>4</sub> (SiNF) peaks. The Si<sub>3</sub>N<sub>4</sub> peak binding energy is measured at 399 eV, which is higher than pristine Si<sub>3</sub>N<sub>4</sub> binding energy. The authors believe this binding energy shift is caused by the fluorine rich environment. The binding energy shifts of SiNF were fixed at +2.27 eV from

Si<sub>3</sub>N<sub>4</sub> peak according to the fitting of measured data, which agrees with prior result.

<sup>3.19</sup> This binding energy shift assumes that F was bonded to the Si which is bonded to a N atom. This assumption will be tested and discussed in the following section.

The O1s spectra were fitted with three peaks. Other than the known SiOF and CO peaks, a small peak located at a higher binding energy is believed to be COF. It is shifted to higher binding energy due to fluorine bonding. Binding energy shifts of -1.8 and +1.8 eV from SiOF peak<sup>3.30, 3.31</sup> were used to fit these carbon-related peaks. Since the binding energies of CO<sub>x</sub> peaks are overlapping with CF<sub>x</sub> peaks in the C1s spectra, the surface FC intensity is calculated by subtracting the CO<sub>x</sub> peak intensities from CF<sub>x</sub> peak intensities. If we assume that the C to O ratio is one for CO and COF peaks, the surface FC intensity can be calculated by:

$$FC = CF(C1s) + 2 \times CF_2(C1s) + 3 \times CF_3(C1s) - CO(O1s) - COF(O1s) \quad (3.3)$$

With the consideration of all chemical bonds from other spectra, F1s spectra should be deconvolved into two peaks, F-SiON and F-C. The area of F-C peak has been constrained to be the intensity calculated according to Eq. (3.3) after sensitivity factor correction. This constrain ensured the FC intensity is consistent across all spectra. Because of lack of available references on the binding energy of F-SiON, an approximation was made which assumed that nitrogen bonding causes a similar shift to that introduced by oxygen, i.e F-SiON have the same binding energies as F-SiO. The O and N next to Si is only indicating the chemical environment. The chemical stoichiometry of Si:O:N or Si:O ratio is not limited to 1:1:1 or 1:1. The binding energy shifts were fixed at -1.2 eV from F-C peak for F-SiON.<sup>3.30, 3.32-3.34</sup>

This fitting method suggests that the sample surface contains two major components, a C containing layer and Si containing layer. Due to the difficulty of distinguishing SiNF and SiOF in F1s, Si<sub>3</sub>N<sub>4</sub> and SiNF in Si2p, the Si containing materials can be treated as a layer with an overall composition of SiO<sub>a</sub>N<sub>b</sub>F<sub>y</sub>. The composition of SiO<sub>a</sub>N<sub>b</sub>F<sub>y</sub>, i.e. a, b, and y values, can be calculated by the ratio of the corresponding peak area ratios. (Eq. 3.4-3.6)

$$a = \frac{\text{SiOF area in O1s}}{\text{total area of Si2p}} \quad (3.4)$$

$$b = \frac{(\text{SiNF} + \text{Si}_3\text{N}_4) \text{ area in N1s}}{\text{total area of Si2p}} \quad (3.5)$$

$$y = \frac{\text{SiONF area in F1s}}{\text{total area of Si2p}} \quad (3.6)$$

$$\text{total negative valence number} = 2 \times a + 3 \times b + y \quad (3.7)$$

The total negative valence number of this layer can be calculated by Eq. (3.7). This total negative valence number of all the examined conditions shows a value of 4, and corresponds to the positive valence number on the Si atom (Fig. 3.13). This charge neutrality result indicates that the O, N, F atoms are bonded directly to Si atoms, and mixed bonds, i.e. F-N, F-O or O-N bonds, are minimal in the surface layer. This adds support to the assumptions used for the fitting methods.

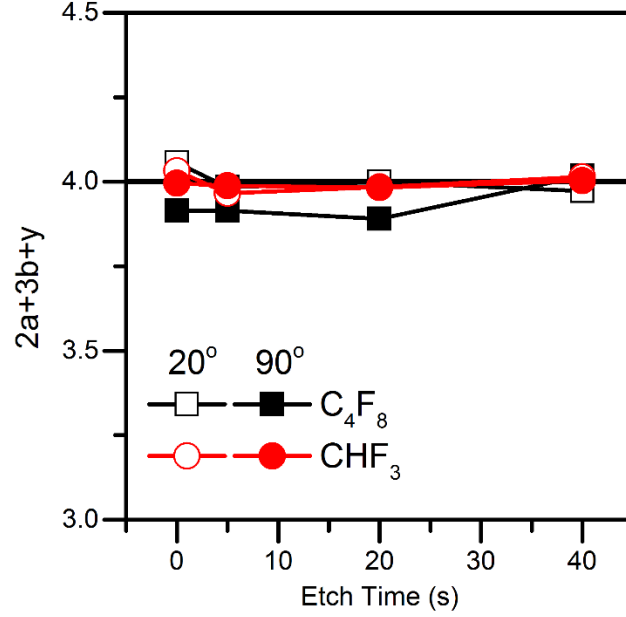


FIG. 3.13 (Color online) Total negative valence number ( $2a+3b+y$ ) evolution of  $\text{SiO}_a\text{N}_b\text{F}_y$  layer during one ALE cycle for both  $\text{C}_4\text{F}_8$  and  $\text{CHF}_3$  based FC depleted conditions in two probing angle.

The FC layer thickness on top of  $\text{Si}_3\text{N}_4$  was calculated employing angle-resolved XPS (AR-XPS) data using the signal attenuation of Si2p intensities obtained at two different electron probing angles ( $90^\circ$  and  $20^\circ$ ). The photon-electron escape depth for the probe angle of  $90^\circ$  is deeper than that of  $20^\circ$ , which leads to the  $20^\circ$  scans being more surface sensitive. The top layer covering the Si containing material, i.e. FC, attenuates the Si2p signal. The FC layer thickness can be calculated by<sup>3,35</sup>

$$d_{FC} = \lambda \left[ \frac{\cos \phi \cos \phi'}{(\cos \phi - \cos \phi')} \right] \ln \left( \frac{I_{\text{Si}2p}}{I'_{\text{Si}2p}} \right) \quad (8)$$

where  $\lambda$  was taken to be 3.2 nm for the electron inelastic mean free path (IMFP) in FC films (estimated by electron IMFP in  $\text{SiO}_2$  layer, due to its similar density and structure to FC)<sup>3,36</sup>,  $I_{\text{Si}2p}$  and  $I'_{\text{Si}2p}$  were Si2p total area for corresponding scans with

$\phi = 0^\circ$  and  $\phi' = 70^\circ$ . These angles are the electron probing angles relative to the normal of the sample surface.

Comparing  $20^\circ$  and  $90^\circ$  scans, SiNF peak intensity is higher at  $90^\circ$  while the SiOF peak intensity is not. This indicates that an oxygen containing layer (SiONF, since nitrogen might be linked to this layer) is located on top of SiNF. The thickness of the material covering SiNF (i.e. FC and SiONF) can be calculated by the attenuation of SiNF intensities:

$$d_{FC+SiONF} = \lambda \left[ \frac{\cos \phi \cos \phi'}{(\cos \phi - \cos \phi')} \right] \ln \left( \frac{I_{SiNF}}{I'_{SiNF}} \right) \quad (3.9)$$

The thickness difference of the two AR-XPS calculations from Eq. (3.8) and Eq. (3.9) is the thickness of the SiONF layer, located in between the FC film and the SiNF film. The thickness evolution during one ALE cycle of FC and SiONF as calculated by AR-XPS is shown in Fig. 3.14 (a) for  $C_4F_8$  and  $CHF_3$  precursors. A decrease of FC thickness and a relatively stable SiONF thickness are seen during the ALE etching step. The source of the oxygen may either be the remaining  $SiO_2$  from the top  $SiO_2$  layer etching, or the chamber coupling quartz window. Comparing  $CHF_3$  to  $C_4F_8$ , a thinner oxygen containing layer has been observed, which may be related to the hydrogen or higher fluorine concentration in  $CHF_3$ .

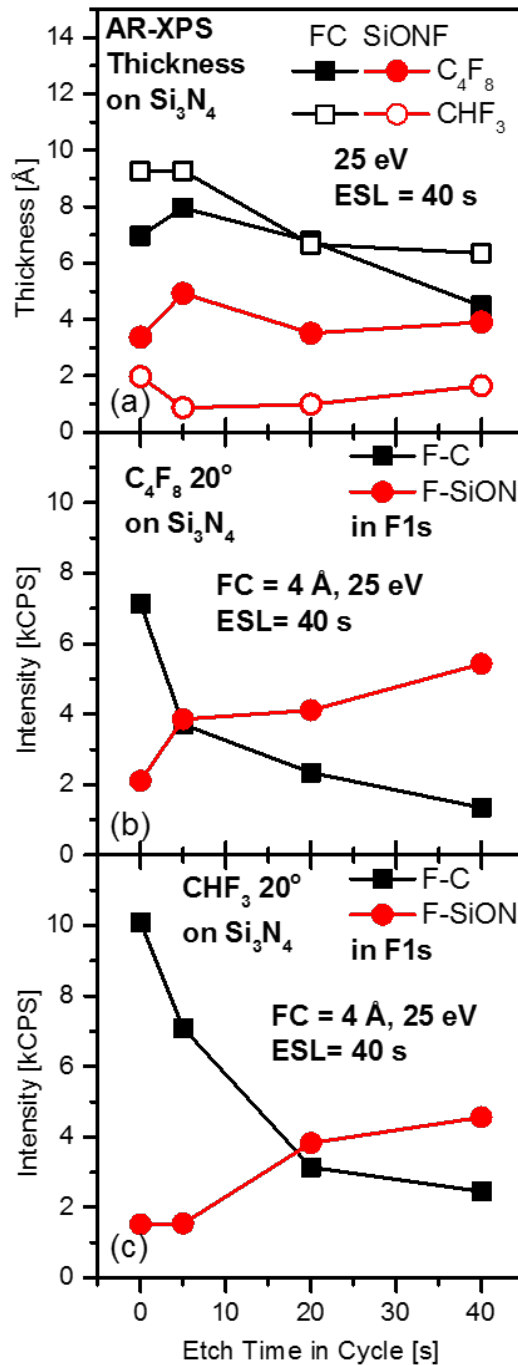


FIG. 3.14. (Color online) Surface chemistry evolution of  $\text{Si}_3\text{N}_4$  surfaces during one ALE cycle for FC depleted conditions. (a) AR-XPS FC film thickness evolution, as calculated by  $\text{Si}2p$  signal attenuation for  $90^\circ$  and  $20^\circ$  electron take-off angles. The individual decomposed peak intensities of F1s spectra are shown for (b)  $\text{C}_4\text{F}_8$  and (c)  $\text{CHF}_3$ . The surface fluorine is transferred from a FC film into the substrate.

The substrate fluorination (F-SiON intensity in the F1s spectra) is shown in Fig. 3.14 (b) and (c) along with the F-C intensity in F1s for both  $C_4F_8$  and  $CHF_3$ . During the ALE etching step, a decreasing F-C intensity and increasing F-SiON intensity have been observed, indicating that fluorine was transferred from the FC layer to the silicon nitride substrate.

After deposition step, a FC film was deposited on the substrate surface. The thickness of this deposition can be directly measured by the AR-XPS FC thickness change, and the ellipsometric overlayer (FC+SiONF+ $Si_3N_4$ ) thickness change. The deposition thicknesses obtained from the two methods are consistent with each other (Fig. 3.15). After etching step, the AR-XPS FC thickness goes back to the initial value, while the overlayer thickness drops about 4 Å lower than the initial value indicating substrate material etching.

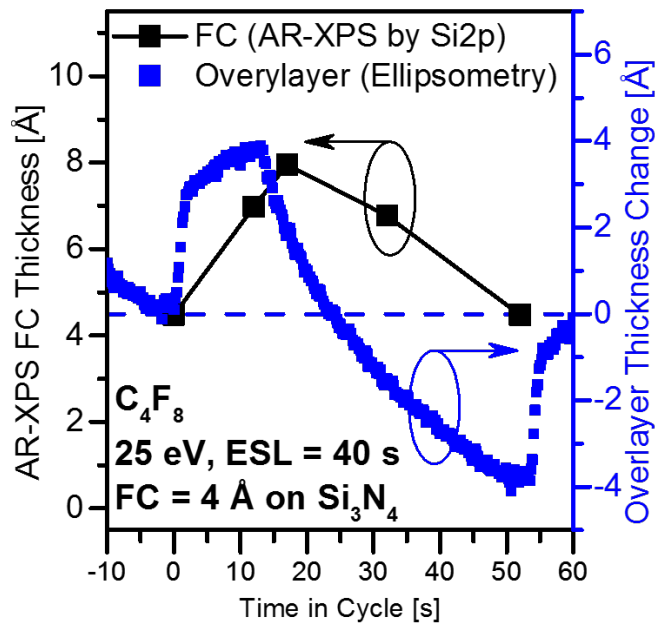


FIG. 3.15. (Color online) Comparison of FC thickness determined by AR-XPS calculation and overlayer thickness change determined by ellipsometry. Thickness

increases after precursor injection obtained by these two methods are consistent with each other. After etching step, the AR-XPS FC thickness goes back to the initial value, while the overlayer thickness drops about 4 Å lower than the initial value indicating substrate material etching.

### **3.3.4.2 Surface chemistry difference for FC depleted condition and FC accumulation condition**

The 20° C1s spectra on Si<sub>3</sub>N<sub>4</sub> surfaces are shown in Fig. 3.16 for FC depleted ((a) 40 s ESL) and accumulation ((b) 20 s ESL) conditions. These spectra were scanned at the end of an etching step with 25 eV maximum ion energy and 4 Å FC deposited per cycle by C<sub>4</sub>F<sub>8</sub>. The intensities of fluorine related carbon peaks were much higher for 20 s ESL than for 40 s ESL. This indicates that there was remaining FC on the Si<sub>3</sub>N<sub>4</sub> surface. For FC depleted conditions, fluorine was mostly reacted or transferred to the substrate after each etching step, as discussed above. The FC thicknesses on Si<sub>3</sub>N<sub>4</sub> surfaces calculated by AR-XPS analysis at the end of the etching step as a function of ESL are shown in Fig. 3.17 with 25 eV maximum ion energy and 4 Å FC deposited per cycle by C<sub>4</sub>F<sub>8</sub>. Each data point in Fig. 3.17 represents one experiment with a specific ESL at the end of etching step on Si<sub>3</sub>N<sub>4</sub>. When the ESL was reduced to 20 s, a thicker FC layer was observed on the substrate surface, which agrees with the ellipsometry measurement, indicating an accumulation of FC.

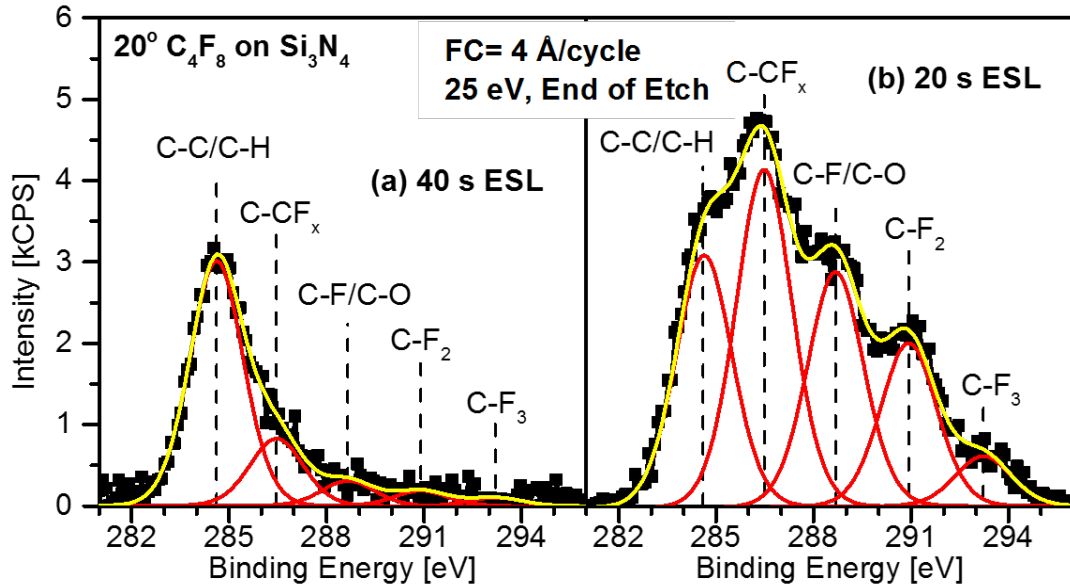


FIG. 3.16. (Color online) 20° C1s spectra of Si<sub>3</sub>N<sub>4</sub> surfaces scanned at the end of etching step with the condition of 25 eV maximum ion energy and 4 Å FC per cycle deposited by C<sub>4</sub>F<sub>8</sub>. Etching step lengths (ESL) of (a) 40 s and (b) 20 s are shown, representing FC depleted and accumulation conditions, respectively.

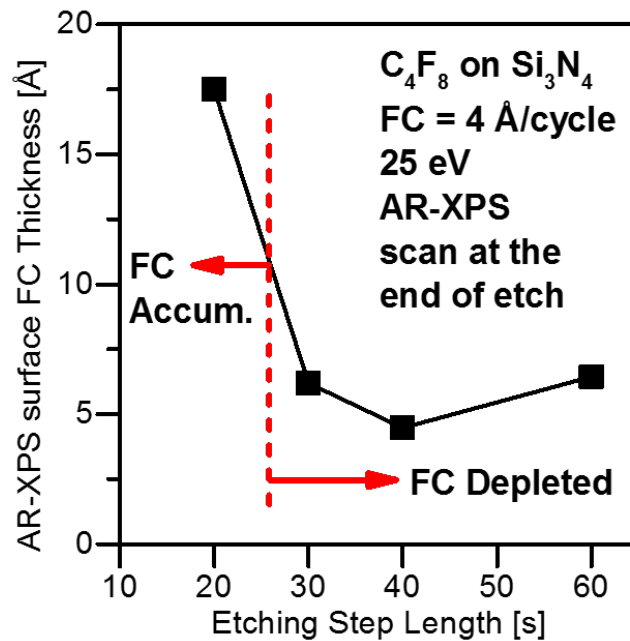


FIG. 3.17. (Color online) AR-XPS FC thickness at the end of etching step as a function of ESL on Si<sub>3</sub>N<sub>4</sub> surface with the condition of 25 eV maximum ion energy and 4 Å FC per cycle deposited by C<sub>4</sub>F<sub>8</sub>. Each data point represents one experiment with a specific ESL at the end of etching step on Si<sub>3</sub>N<sub>4</sub>. 20 s ESL shows an accumulation of FC on the Si<sub>3</sub>N<sub>4</sub> surface.

### 3.4 SUMMARY AND CONCLUSIONS

In this work, conditions enabling the achievement of Si<sub>3</sub>N<sub>4</sub> to SiO<sub>2</sub> and SiO<sub>2</sub> to Si<sub>3</sub>N<sub>4</sub> etching selectivity during ALE have been studied. Si<sub>3</sub>N<sub>4</sub> to SiO<sub>2</sub> etching selectivity has been observed for FC depleted conditions, and can be explained by a lower physical sputtering energy threshold for Si<sub>3</sub>N<sub>4</sub> relative to SiO<sub>2</sub>. In order to obtain SiO<sub>2</sub> to Si<sub>3</sub>N<sub>4</sub> etching selectivity, FC accumulation conditions, i.e. process conditions for which increasingly thicker FC films are produced on Si<sub>3</sub>N<sub>4</sub> due to a lower carbon consumption relative to SiO<sub>2</sub>, were employed. These conditions are possible because of the lower reaction rate of the FC film on a Si<sub>3</sub>N<sub>4</sub> surface relative to a SiO<sub>2</sub> surface and can be achieved by using low ion energies, short ESLs, and/or high FC film deposition per cycle. Using these methods, the ALE process can be optimized to favor the substrate dependent interaction, leading to a high SiO<sub>2</sub> to Si<sub>3</sub>N<sub>4</sub> selectivity. The comparison of C<sub>4</sub>F<sub>8</sub> and CHF<sub>3</sub> showed a difference in etching selectivity for FC depleted conditions. For FC accumulation conditions, precursor chemistry has less impact on etching selectivity. The surface chemistry analysis showed that surface fluorination and FC reduction take place during an ALE cycle for FC depleted conditions. A fluorine rich carbon layer was observed on the surface after ALE processes for which FC accumulation takes place. The AR-XPS thickness calculations confirmed the ellipsometric observations in all cases.

## **ACKNOWLEDGMENTS**

The authors gratefully acknowledge the financial support of this work by the National Science Foundation (CBET-1134273), US Department of Energy (DE-SC0001939), Lam Research Foundation, and Semiconductor Research Corporation (Task 2603.001). The authors thank Dr. E. Bartis, A. Knoll, P. Luan, A. Pranda and H. Wang for helpful discussions and collaboration. They also thank M. Danek and A. Dulkan from Lam Research, and C. Labelle, A. P. Labonte, C. Park, and G. Beique from GLOBALFOUNDRIES for helpful discussions.

## **Chapter 4: Hollow Cathode Plasma Electron Beam Secondary Plasma Production and Etching of Si<sub>3</sub>N<sub>4</sub> and Polycrystalline Si**

C. Li, V. Godyak, T. Hofmann, K. Edinger and G. S. Oehrlein

### **ABSTRACT**

A material etching system was developed and evaluated that is founded on an Ar-based direct current (DC) hollow-cathode (HC) electron beam source and electron-beam injection into the downstream reactive environment of a remote CF<sub>4</sub>/O<sub>2</sub> plasma. The primary electron beam energy is controlled by the extraction voltage relative to the HC discharge. For an extraction voltage greater than the ionization potential of Ar, the extracted primary electrons can produce a secondary plasma in the process chamber. We have characterized the properties of the secondary plasma and surface etching of Si<sub>3</sub>N<sub>4</sub> and poly-crystalline Si (poly-Si) as a function of process parameters such as the extraction voltage (0-70 V), discharge current of the HC discharge (1-2 A), pressure (2-100 mTorr), source to substrate distance (2.5 to 5 cm), and feed gas composition (with or without CF<sub>4</sub>/O<sub>2</sub>). The electron energy probability function (EEPF) measured by a Langmuir probe 2.5 cm below the extraction ring suggests two major components for this situation: a primary electron beam with an energy which varies as the extraction voltage is varied and low energy electrons produced by ionization of the Ar gas atoms in the chamber into which the electron beam is injected. When combining the HC Ar EB with a remote CF<sub>4</sub>/O<sub>2</sub> electron cyclotron wave resonance (ECWR) plasma, both the low energy plasma electron and beam electron components decreased in the EEPF. An

electron-neutral synergy etching effect has been observed for  $\text{Si}_3\text{N}_4$  and polycrystalline silicon etching. No/little remote plasma spontaneous etching was observed for the conditions used in this study, and the etching is confined to an area covered by the injected electron beam. The electron beam etched  $\text{Si}_3\text{N}_4$  surface etching rate profile distribution is confined within a  $\sim 30$  mm diameter circle, which is slightly broader than the area for which poly-Si etching is seen, and coincides closely with the location for which the Langmuir probe measurements indicated beam electrons. The magnitude of poly-Si etching rate is also by a factor of two times smaller than the  $\text{Si}_3\text{N}_4$  etching rate. A possible explanation is that increased negative surface charging for the  $\text{Si}_3\text{N}_4$  surface introduces additional energy input to the surface, e.g. by ion bombardment of the  $\text{Si}_3\text{N}_4$  surface.

## 4.1 INTRODUCTION

Angstrom level precision etching processes are essential to scale down semiconductor devices to several nm critical dimension.<sup>4.1-4.4</sup> Traditional plasma-based dry etching techniques utilize ion bombardment to achieve material removal either physically<sup>4.5</sup> or by synergistic interactions with added reactive chemical species<sup>4.6, 4.7</sup>. Recently, a new ion-based etching technique called atomic layer etching (ALE)<sup>4.8, 4.9</sup> has been developed for use in semiconductor fabrication<sup>4.10</sup>, which is based on temporal separation of chemical reactant supply and ion bombardment induced etching that takes place in two sequential steps. The ion bombardment energy is set to a low level (in between the chemical enhanced etching energy threshold and physical sputtering energy threshold) to ensure a self-limited etching stop. This ALE ion energy is much lower than the traditional continuous wave (CW) plasma etching ion energy, which reduces the substrate damage and enables high materials etching selectivity.<sup>4.11- 4.14</sup> However, this ALE method still faces difficulty when etching material with low physical sputtering threshold, e.g. Si or SiGe, due to plasma potential limiting the lowest possible ion energy<sup>4.15</sup> and/or plasma chamber wall interactions<sup>4.16</sup>. The momentum transfer of ions causes damage and surface roughness to the etched material surface.<sup>4.17, 4.18</sup> Moreover, the minimum ion bombardment energy is limited by the sheath potential (typically 15-20 eV for inductively couple plasma<sup>4.9</sup>), causing difficulties with respect to achieving material etching selectivity for materials with a low energy threshold for etching, such as Si or SiGe<sup>4.15</sup>.

Electron-beam (EB) induced etching is a potential approach for low damage selective etching applications.<sup>4.7, 4.19-4.21</sup> Similar to ion assisted etching, electron assisted gas surface interaction has also been discussed by Coburn and Winters as early as 1979 using XeF<sub>2</sub> to etch Si<sub>3</sub>N<sub>4</sub>, SiO<sub>2</sub> and SiC surfaces<sup>4.7</sup>. They suggested three possible mechanisms for electron enhanced etching of materials: (1) enhanced dissociative chemisorption at defects produced by electron bombardment; (2) electron-enhancement of precursor dissociation near the surface; (3) electron-induced removal of the reacted surface layer. Focused electron beam (FEB) assisted etching was reported later using XeF<sub>2</sub> precursor to etch Si, SiO<sub>2</sub>, Si<sub>3</sub>N<sub>4</sub>, TaN, and AlGaAs<sup>4.21-4.23</sup>. However, for FEB research electron energies are typically above 1keV. At these energies, the interaction of primary electrons with surface atoms is weak. Most surface reactions are induced by secondary electrons near the surface in the energy range below 100 eV. Furthermore, FEB electron sources are normally based on thermionic electron emission and require very low background pressure for stable operation. However, higher pressure exposures are preferred to ensure high working throughput when doing the chemical exposure. For the above reasons, an alternate electron beam source operating at low electron energy and high working gas pressure is preferred for this application.

Hollow cathode (HC) electron beam sources<sup>4.24-4.32</sup> allow to inject electron beams into a fairly high pressure gas (up to 100s of mTorr), and cover an area is being treated that can be fairly large (~cm<sup>2</sup>). Gershman and Raitses<sup>4.33</sup> performed studies of hollow cathode and anode EB plasma sources for which they demonstrated the presence of ~15 eV beam electrons by Langmuir probe and optical emission

spectroscopy measurements. They stated, “These electrons become available for surface modification and radical production outside of the source” which “opens exciting opportunities for future exploration.”

Recently, material etching using a HC EB plasma was reported by Walton and Boris *et al.* from Naval Research Laboratory<sup>4.20, 4.34-4.37</sup>, and Rauf and Dorf *et al.* from Applied Materials, Inc.<sup>4.19, 4.38-4.40</sup>. In their work, the EB is parallel to the substrate surface and a beam dump is used for the electrons after having passed through the plasma volume. Surface processing is controlled via radio frequency biasing of the substrate by adjusting the energy of the low energy ions produced by the EB plasma. The potential of utilizing plasma-produced EBs injected into process chambers for direct control of surface processes has hardly been studied. This contrasts with work in the focused electron-beam community for which surface reactions are stimulated by energetic electrons in non-plasma environments.

In this work the authors have used a HC EB source with low and adjustable electron energy that allows electron beam injection into a relatively high pressure (~mTorr) environment, thus allowing combination with a remote plasma source. The latter provides reactive radicals and the combination of these sources was being evaluated for the purpose of achieving electron enhanced chemical etching.

This article is organized as follows: in the first part, the authors discuss the development and characterization of the Ar hollow-cathode electron beam source by measuring electrical current at the sample position and optical emission from the secondary plasma region. In the second part, the electron beam and the secondary plasma generated were characterized by Langmuir probe measurement in both pure

Ar and when combining with the effluent from a CF<sub>4</sub>/O<sub>2</sub> remote plasma used for substrate etching. In the final part, the authors study electron enhanced chemical surface etching of Si<sub>3</sub>N<sub>4</sub> and poly-crystalline Si for the conditions where the HC electron beam source is combined with the effluent of the CF<sub>4</sub>/O<sub>2</sub> remote plasma source.

## 4.2 EXPERIMENTAL

The experiments were performed in an electron beam etching system, consisting of a hollow cathode (HC) EB source on top of a reaction chamber and an electron cyclotron wave resonance (ECWR) remote plasma source on the side (Fig. 1(a)). The base pressure achieved before processing was in the  $1 \times 10^{-6}$  Torr range. The pressure in the HC source (Torr level) is significantly higher than the chamber pressure below because of a choked flow connection. The reaction chamber pressure was kept at 2-100 mTorr during processing using a butterfly valve in the pumping line. The ECWR remote plasma source consists of a COPRA DN160 ECWR plasma beam source running at 13.56 MHz radio frequency with a modified neutralization plate<sup>41</sup>. This neutralization plate consists of an electrically grounded aluminum plate covered by Kapton tape and a quartz plate to protect the plate from plasma erosion. Direct exposure of the substrate and reaction chamber to the ECWR plasma is prevented by this plate, and only neutral chemical radicals can diffuse from the ECWR chamber to the processing chamber, creating a remote plasma process condition<sup>4.42-4.44</sup>. The ECWR effect requires an additional static magnetic field to utilize interaction of an electromagnetic wave with a plasma.<sup>4.41</sup> A 400 W source

power level and 1.8 mT static magnetic fields were applied to the ECWR system for all experiments requiring chemical radicals.<sup>4,41</sup> As shown in Fig. 1 (a), the EB source, consists of a 1.57 mm diameter direct current (DC) HC tube, a 34.35 mm diameter discharge tube, an anode plate with a hole in it, a separation mesh and an electron acceleration plate. The latter is located below the HC source and inside the vacuum chamber above a water cooled (10 °C) and electrically grounded stainless steel (S. S.) substrate. The electrons are extracted from the HC plasma through a 1.57 mm diameter hole in the anode. A S. S. mesh with high transmission is attached to the anode plate, and prevents the extraction electric field to penetrate into the HC plasma region. This kind of HC electron beam setup is well developed and characterized, and we refer the reader to descriptions and applications where similar setups have been employed.<sup>4.24-4.32</sup>

Argon gas was admitted to the HC discharge using a mass flow controller. The EB source to substrate distance can be varied with an adjustable bellows tube over a range of **70 mm**. A DC power supply providing constant discharge current ( $I_D$ ) was used to generate the main HC plasma discharge between the cathode and the source anode. A second DC power supply provided an extraction voltage ( $V_E$ ) to the anode plate to accelerate a beam of electrons through the center hole of the grounded acceleration plate toward the grounded substrate. The acceleration plate to HC anode plate distance is 10 mm.

The equivalent circuit diagram is shown in Fig. 1 (b). The arrows depict the direction in which electrons move, and is opposite to the conventional current direction. The HC discharge provides an electron current  $I_D$ . Typical EB source

operating conditions are 10 sccm Ar carrier gas flow for a constant 1.5 A discharge current ( $I_D$ ). Part of  $I_D$  flows through the HC anode back to the discharge power supply ( $I_a$ ). The extraction current  $I_E$  penetrates through the central hole of the HC anode and moves towards the acceleration plate. With a positive bias voltage on the acceleration plate, electrons are accelerated, and then move toward the substrate after having gained additional energy. A portion of the extraction current flows back to the power supply through the acceleration plate ( $I_A$ ), while the rest of the electrons are transmitted through the aperture. These primary beam electrons move towards the substrate and, if sufficiently energetic, cause additional ionization as they move through the Ar gas in the main chamber. The net DC current measured at the grounded substrate is denoted with  $I_B$ .

A photograph of the EB plasma is shown in Fig. 1 (c). The top bright region is the Ar plasma discharge located between the hollow cathode anode and the acceleration plate. An energetic electron beam is extracted through the center aperture of the acceleration plate, reaching the grounded S. S. substrate. The cone shaped beam shown underneath the acceleration plate is due to a lens focusing effect of the acceleration aperture. By adjusting the acceleration plate to EB source distance and the aperture opening size, the focus point can be optimized.

The electron beam and the secondary plasma generated have been characterized using a Langmuir probe (LP). The LP used in this study is designed to collect highly accurate measurements of the electron energy probability function (EEPF), electron density ( $n_e$ ), and electron temperature ( $T_e$ ) by fast sweep speeds, ion bombardment cleaning, and electron heating.<sup>4.45-4.47</sup> The probe tip and reference

probe were located in the center below the acceleration plate and above the substrate electrode. The cylindrical tungsten probe tip was 4.8 mm long with a 0.025 mm radius, and for these measurements was located 25 mm beneath the acceleration plate. We should mention that the interpretation of the LP data for this situation is complex owing to the fact that typical assumptions used for interpretation of LP data, e.g. isotropic distribution of electron energies, are not justified for the present situation. Nevertheless, these measurements provide a qualitative overview of the behavior of beam electrons and their influence on secondary plasma production and interactions.

In addition, an optical emission spectrometer (OES) setup is attached to the chamber and allows to measure plasma optical emission intensity and gas phase chemical composition in real time. The Ar I and Ar II emissions at wavelengths of 750.39 nm and 472.69 nm, respectively, were measured as the energy of the extracted EB was varied. For conditions when CF<sub>4</sub>/O<sub>2</sub> reactive processing gases were used, F and O emissions were monitored at wavelengths of 685.60 nm and 777.19 nm, respectively.

Sample surface etching and modification was monitored in real time with an *in situ* ellipsometer setup that used a HeNe laser ( $\lambda = 632.8$  nm). The ellipsometer is an automated rotating compensator ellipsometer working in the polarizer-compensator-sample-analyzer (PCSA) configuration at an incident angle of  $\approx 73.5^\circ$ .

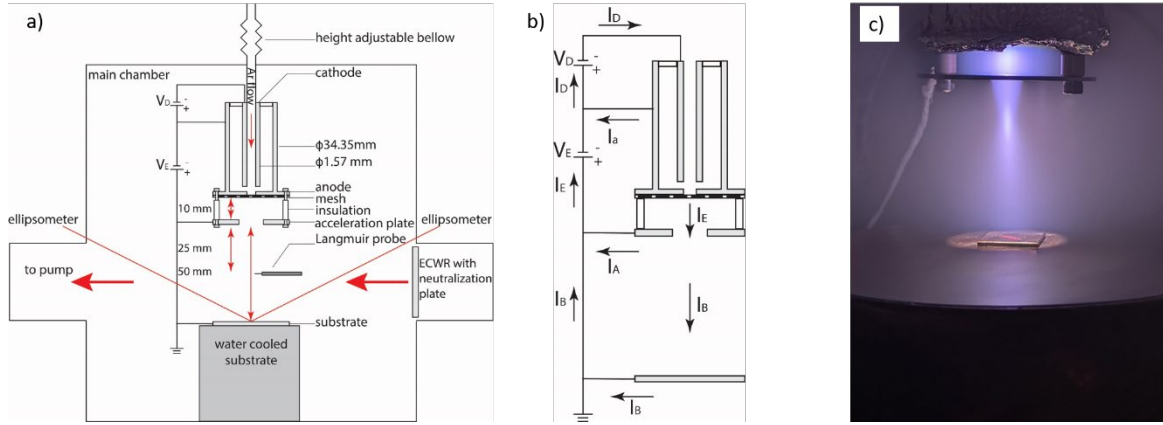


FIG. 4.1 (Color online) (a) Schematic overview of the experimental layout of the multi-chamber tool and (b) notations of currents and voltages of the electrical setup. In (c) a photograph of the setup when used with an Ar EB is shown.

## 4.3 RESULTS AND DISCUSSION

### 4.3.1 Parametric studies of hollow cathode EB source

In order to utilize the HC EB source for etching studies, characterizing the electron source behavior, such as electron-gas interaction, EB induced secondary plasma production, electron energy control and other aspects is essential. For these HC EB source characterization experiments, only the EB HC source and the Ar gas flow into the main chamber were used. No  $\text{Si}_3\text{N}_4$  or poly-Si samples were present on the S. S. substrate electrode and the ECWR chamber/additional  $\text{CF}_4/\text{O}_2$  gas flows were also not used. Electrons passing through the hole in the anode were accelerated by the extraction voltage.<sup>4,27</sup> It is well known that high-energy electrons can be scattered by gas molecules through elastic or inelastic collisions. When the energy of electron is higher than gas excitation/ionization threshold, inelastic collision will take place with a certain cross section and this additional ionization can produce plasma discharge in the main chamber in the present situation. As a direct way to characterize

the EB and the secondary plasma discharge produced, the electrical current at the substrate electrode and optical emission characterization of the EB were studied for varying extraction voltages,  $V_E$ . This is shown in Fig. 4.2 for operating conditions of 10 sccm Ar flow rate, 2 mTorr main chamber pressure, 1.5 A discharge current  $I_D$  in the HC source, and 5 cm acceleration plate to substrate distance.

When  $V_E$  is greater than 20 V, the electron energy is greater than the Ar ionization energy threshold (15.76 eV). Consistent with this, a strong increase of all measured currents is shown in Fig. 4.2, along with a significant rise of both Ar I (neutral Ar) and Ar II emission (from excited  $\text{Ar}^+$  ions). This current/emission increase saturates at  $V_E$  of about 50 V, and is limited by the total discharge current  $I_D$  in the HC setup and the setup geometry. As shown in Fig. 4.2(a), measurement of the emission current  $I_E$ , the acceleration plate current  $I_A$  and the net measured substrate current  $I_B$  increase with extraction voltage  $V_E$ . The sum of  $I_A+I_B$  is shown in Fig. 4.2(a) and equals the measured extraction current  $I_E$ . This matched current indicates that electrons leaving the HC or produced by additional ionization in the main chamber are mostly collected by the anode, acceleration plate and the substrate. Electron loss to the chamber walls or other grounded surfaces is limited, consistent with a strong degree of directionality towards the substrate electrode. The measured currents provide an estimate of the net electron current, and the influence of the ion current to these surfaces, e.g. the substrate electrode surface, is not known. A contribution of the latter appears unavoidable since these surfaces are in contact with a plasma discharge region.

The behavior of the optical emission intensity of Ar I and Ar II reflects the atomic Ar and Ar<sup>+</sup> ion, respectively<sup>4.30</sup>. The production rate of excited atomic and ionized Ar<sup>+</sup> are proportional to the excitation and ionization cross sections, respectively. Comparing the emission intensities of Ar I (750.39 nm) and Ar II (472.69 nm) in Fig 4.2(b), the Ar II emission (ionized Ar) peaks at a higher energy than Ar I (atomic Ar), which agrees with the electron impact ionization and excitation cross section trends.<sup>4.28</sup>

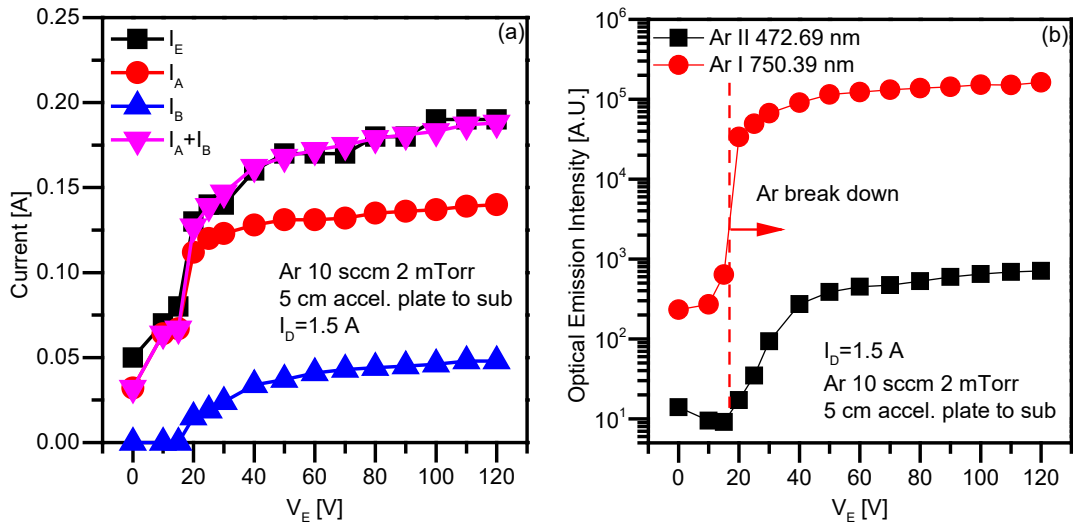


FIG. 4.2 (Color online) Electrical current and optical emission characterization of the EB source/main chamber setup are shown as a function of extraction voltage,  $V_E$ . (a) Measurement of emission current  $I_E$ , acceleration plate current  $I_A$  and net measured substrate current  $I_B$  with varying extraction voltage  $V_E$ . (b) Corresponding behavior of optical emission intensity of Ar I (750.39 nm) and Ar II (472.69 nm) versus  $V_E$ .

To further understand the behavior of EB, the electrical current response at 50 V extraction voltage was evaluated for the other EB source parameters, i.e. discharge current ( $I_D$ ), pressure in the process chamber, and acceleration plate to substrate distance. The variation of emission current  $I_E$ , acceleration plate current  $I_A$  and net

measured substrate current  $I_B$  as a function of these parameters is shown in Figs. 4.3 (a) through 4.3(c), respectively. With increased discharge current  $I_D$  (Fig. 4.3 (a)) all other currents increase linearly. This indicates that  $I_D$  controls the total EB current, consistent with the expectations.

With increased chamber pressure, the ionization in the main chamber increases and both emission current and acceleration plate current to increase. This indicates that a portion of the low energy electrons created in the proximity of these electrodes are collected. On the other hand, the net measured substrate current  $I_B$  decreases with pressure. This indicates that more electron-neutral collisions reduces the number of accelerated electrons from reaching the substrate electrode, leading to a reduced  $I_B$ .

As the distance between the extraction electrode and substrate electrode is varied, the relative importance of electron interactions with gas phase species or surface species changes. By changing this distance (Fig. 4.3 (c)),  $I_A$  stays the same due to an unchanged discharge condition between the EB source anode and the acceleration plate. However, the net measured substrate current  $I_B$  and emission current  $I_E$  drop slightly when increasing the distance. This reduction of current is caused by more electron-neutral collisions taking place along the path towards the collecting substrate electrode, and thus preventing those electrons to reach the substrate electrode. This current reduction is more pronounced at higher pressure (10 mTorr)

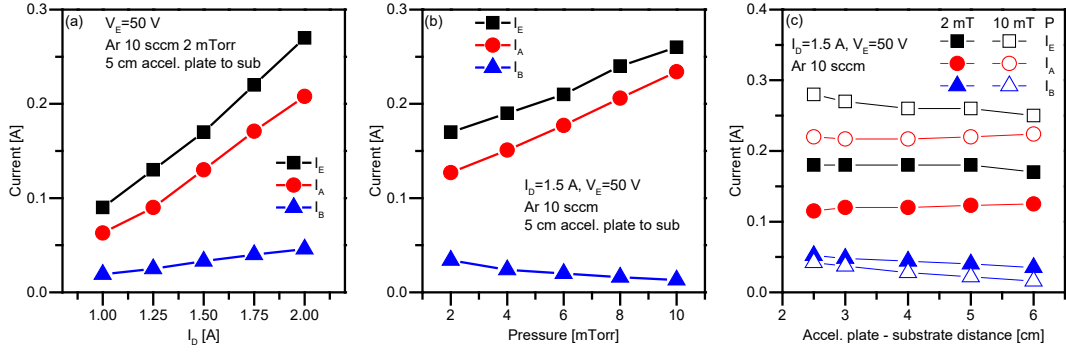


FIG. 4.3 (Color online) Measurement of extraction current  $I_E$ , acceleration plate current  $I_A$  and net measured substrate current  $I_B$  with varying (a) discharge current  $I_D$ , (b) process chamber pressure and (c) distance at 2 mTorr (solid) and 10 mTorr (open) at 50 V extraction voltage.

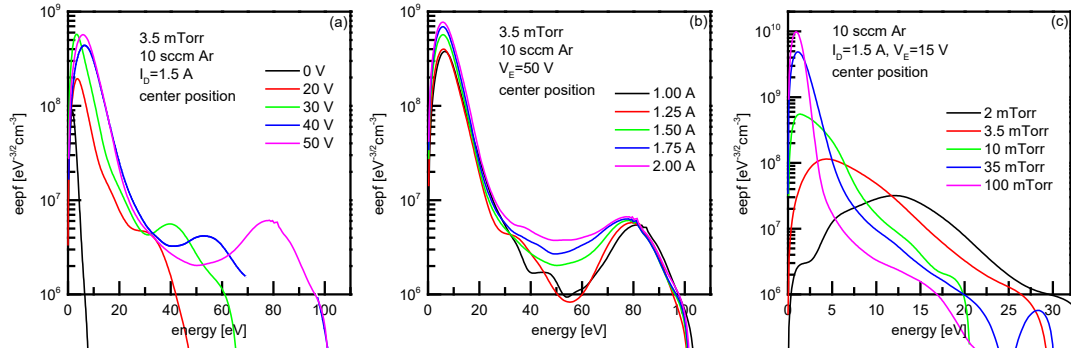


FIG. 4.4 (Color online) Electron energy probability function (EPPF) measured by Langmuir probe for Ar EB with varying (a) extraction voltage  $V_E$ , (b) discharge current  $I_D$ , and (c) pressure. The EPPF of EB generated plasma consists with two major peaks separated by energy.

### 4.3.2 Langmuir probe measurement of hollow cathode EB

The electron beam and its generated secondary plasma have been characterized using a Langmuir probe (LP). The LP used in this study is designed to collect highly accurate measurements of the electron energy probability function (EPPF), electron density ( $n_e$ ), and electron temperature ( $T_e$ ) by fast sweep speeds, ion bombardment cleaning, and electron heating.<sup>4.45-4.47</sup> We should mention that the

interpretation of the LP data for the current situation is complex owing to the fact that typical assumptions, e.g. isotropic distribution of electron energies, used for interpretation of LP data are not justified for the present situation. Nevertheless, the current measurements provide a qualitative overview of the behavior of beam electrons and their influence on secondary plasma production and interactions with the gas and sample surface. The LP measurements of HC electrons in most other publications focus on the low electron energy portion of the EEPF, which is the final electron energy state of the fast beam electron after many in-elastic collisions.<sup>4.25, 4.35, 4.48</sup> The anisotropic beam electron EEPF has recently been measured and discussed by Gershman, Kraus and Raitses for their HC plasma source with a beam electron energy of about 15 eV.<sup>4.33, 4.49</sup>

In this section, EEPF measurements performed with pure Ar HC EB are described first. The change of EB EEPF as CF<sub>4</sub>/O<sub>2</sub> is added follows this description.

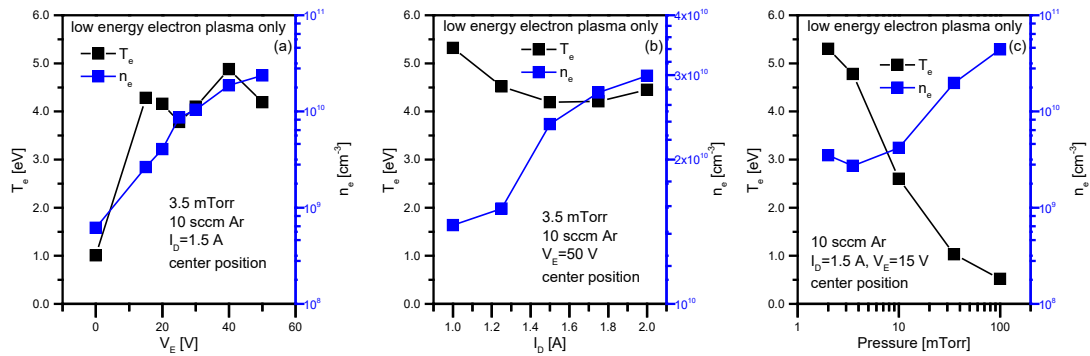


FIG. 4.5 (Color online) Electron temperature ( $T_e$ ) and electron density ( $n_e$ ) calculated for the low electron energy portion of EEPF measured by Langmuir probe for Ar EB with varying (a) extraction voltage  $V_E$ , (b) discharge current  $I_D$ , and (c) pressure.

The results of the Langmuir probe measurements demonstrate the impact of the beam electrons injected from the hollow cathode (HC) source into the process chamber and are shown in Fig. 4.4. The standard HC operating conditions were fixed at 10 sccm Ar, 5 cm operation distance, 3.5 mTorr main chamber pressure, 1.5 A discharge current, and 50 V extraction voltage. The following experiments were studied by varying one of the above parameters. The measured electron energy probability function (EPPF) is shown versus extraction voltage  $V_E$  in Fig. 4.4(a), discharge current  $I_D$  in Fig. 4.4(b) and pressure in the process chamber in Fig. 4.4(c).

In Fig. 4.4 (a), the pressure in the process chamber was held constant at 3.5 mTorr. For an extraction voltage of 0V, the measured EPPF indicates some electrons leaked from the hole in the anode and the center hole of the acceleration plate to the position of the LP. They are characterized by a very low electron energy and density  $N_e$ . A strong increase in electron density is seen as the extraction voltage is increased, and can be explained by beam electrons in the reaction chamber and ionization of the Ar gas by beam electrons. For example, for an extraction voltage of 30 V the data show that the Ar EB EPPF contains two major peaks for a pressure of 3.5 mTorr. A possible explanation is that the peak at  $\sim 10$  eV is due to electrons that have lost energy by in-elastic scattering with gas molecules. This low electron energy peak may be the isotropic HC EB induced plasma peak, which was reported widely in other publications.<sup>4.25, 4.35, 4.48</sup> A second peak at  $\sim 30$  eV and higher – with the position depending on extraction voltage - likely represents the primary beam electrons that have not lost energy in inelastic collisions. Figure 4.4(b) shows the EPPF with increasing discharge current ( $I_D$ ). Higher  $I_D$  will increase electron densities for all

energies with unchanged primary EB peak energy. At high  $I_D$  conditions, an additional electron distribution is shown in between the two major peaks (in about 30-60 eV). This mid-energy range electron distribution relates to either insufficient acceleration from the extraction plate or the final state of beam electrons after several collisions. The impact of pressure in the main chamber on EEPF has also been evaluated and is shown in Fig. 4.4(c). As the pressure in the main chamber is varied, strong changes in EEPF have been observed. These changes are consistent with the qualitatively expected behavior considering the electron inelastic mean free path and energy dependence of the Ar ionization cross section. Since the beam electron component disappeared with increased pressure, we only focused on the low energy plasma peak in the EEPF. Due to a greater number of inelastic collisions between gas and electrons for high-pressure operating conditions, high-energy electrons will lose their energies by exciting/ionizing Ar atoms, leaving a sharper EEPF peak in the lower energy region and no more primary beam electrons.

When applying a regular Maxwellian distribution model for an isotropic plasma to the low energy portion of the EEPF, the corresponding electron temperature and density can be calculated and is shown in Fig. 4.5(a-c) for varying  $V_E$ ,  $I_D$  and pressure respectively. The electron temperature is unchanged at 4-5 eV for various extraction voltages. The electron density increases initially and saturates at high  $V_E$ . The discharge current  $I_D$  controls the total available electrons for extraction and acceleration. For the same extraction voltage,  $n_e$  increases with  $I_D$ . Due to more collisions with more available electrons,  $T_e$  drops with  $I_D$ . As discussed above, the

higher collision rate with increased pressure will reduce the electron temperature  $T_e$  and result in a higher electron density  $n_e$ .

The beam-electron peak energy is plotted versus extraction voltage in Fig 4.6(a) with two reference energy lines ( $V_E$  and  $V_E+V_D$ ). The beam electron peak energy is higher than the extraction voltage and indicates that the electrons may gain some additional energy from the top discharge (voltage between HC and anode,  $V_D$ ). This may be due to less effective decoupling of the extraction electrode from the HC source as the extraction voltage is increased to very high values. With an increased extraction voltage, the lower energy peak is almost unchanged, but the higher energy peak moves linearly with extraction voltage. The peak area of EB plasma and the primary beam peaks are shown in Fig. 4.6(b) with varying  $V_E$ . Both peak areas show saturation when  $V_E$  is greater than 30 V, indicating that after a certain extraction voltage, electron density and electron energy can be controlled separately.

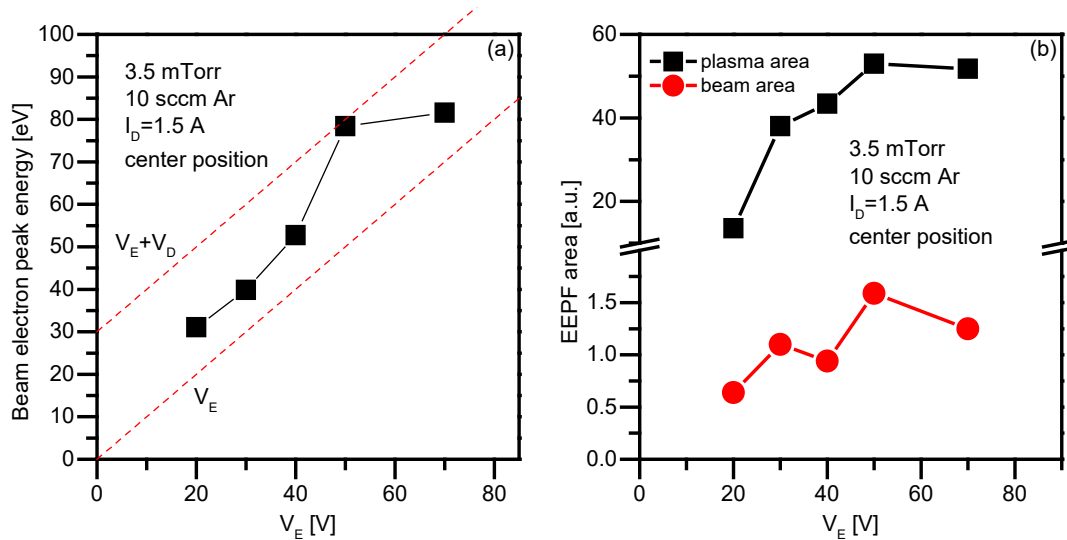


FIG. 4.6. (Color online) Beam electron peak energy vs extraction voltage  $V_E$  with reference to  $V_E$  and  $V_E+V_D$  (a). The EEPF areas for both peaks vs extraction voltage  $V_E$  (b)

The EEPF areas for three different energy ranges are calculated and shown in Fig. 4.7 (a) with  $I_D$ . The electrons in all three energy ranges increase linearly with  $I_D$ . With linear fittings, the slopes are calculated and shown in Fig. 4.7(b). This slope indicates the electron production efficiency in the specific energy range. Like the EEPF, EB plasma region (0-30 eV) shows the highest slope. This indicates that the majority of the additional electrons from  $I_D$  lose energy as a result of multiple inelastic collisions (the energy loss for an electron colliding with Ar atoms is characteristic and give rise to a specific energy loss depending on the Ar energy states corresponding to the excitation/ionization). The electrons in the middle energy range (30-60 eV) represent electron experiencing insufficient collisions and only losing some energy. The increase of EEPF in this middle energy range provides some indirect evidence for the assumption that the primary EB is anisotropic if it experiences no inelastic collisions with the Ar gas in the main chamber.

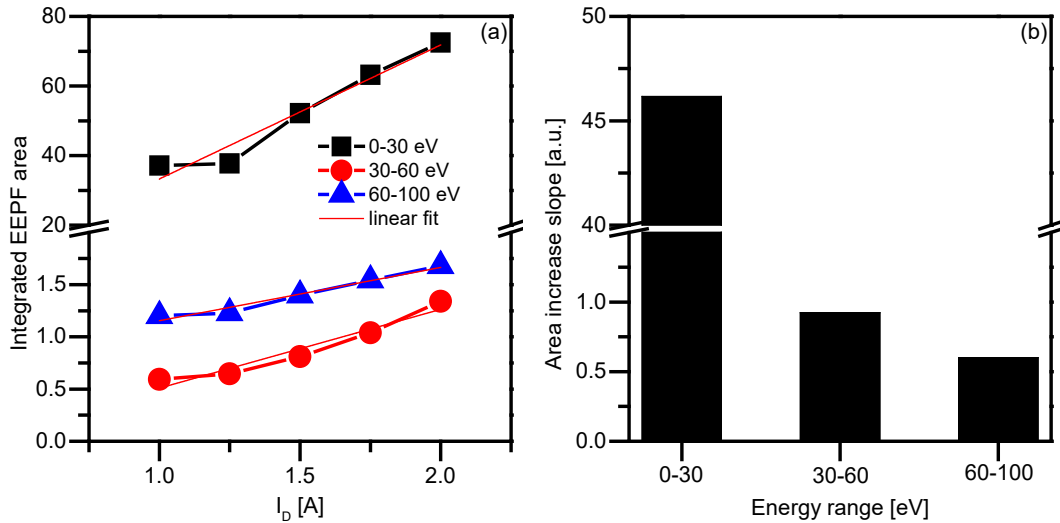


FIG. 4.7. (Color online) The EEPF area for three energy ranges vs  $I_D$  (a) and area slope of increase for three energy ranges (b)

The combination of a HC EB source with a remote plasma radical source was used to investigate EB related surface processes. Before describing these results, we briefly review related Langmuir probe measurements. In Fig. 4.8, the results of Langmuir probe measurements are shown for this combination, demonstrating the impact of beam electrons injected from the HC source into the process chamber. The HC operating conditions were fixed at 10 sccm Ar, 3.5 mTorr with 1.5 A discharge current and 50 V acceleration voltage. A processing gas mixture of CF<sub>4</sub>/O<sub>2</sub> (1:4) was injected into the ECWR remote plasma source using different gas flow rates relative to the Ar flow from the HC EB source. The CF<sub>4</sub>/O<sub>2</sub> ratio was chosen so that spontaneous etching of Si<sub>3</sub>N<sub>4</sub> or poly-Si under remote plasma operating conditions was negligible.<sup>4.50, 4.51</sup>

Figure 4.8 shows the measured electron energy probability function versus processing gas flow rate for this situation. The data are characterized by a higher noise level than the pure Ar data (no ECWR source) which may be due to electrons from the ECWR leaking into the main chamber and interacting with the HC EB. Only qualitative analysis of these data will be discussed here. As discussed, for the EEPF of pure Ar operating conditions we observed two major peaks in the EEPF representing plasma electrons and beam electrons. With a small admixture of the CF<sub>4</sub>/O<sub>2</sub> processing gases, both peaks drop dramatically due to the reduction in the overall plasma density from the injection of the electronegative processing gases. This indicates that the low energy electrons are attached to electronegative gas species. When the processing gas flow rate is at 2 sccm and greater, the EEPFs distributions remain fairly similar. An increase in the higher energy peak was

observed and the low energy peak remains at the same height. This may relate to more processing gas interacting with the HC source and changing the plasma. Since the ionization cross section of  $\text{CF}_4/\text{O}_2$  is different from that of Ar, the high-energy beam electron peak position varies. For this reason, the processing gas flow rate was fixed to 10 sccm for further tests.

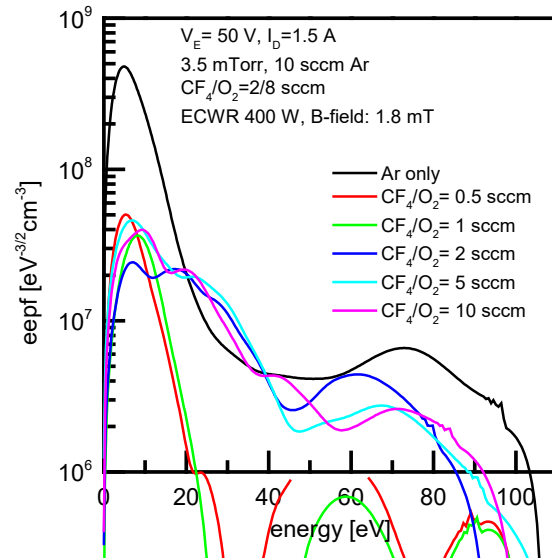


Fig. 4.8 (Color online) Electron energy probability function (EPPF) measured by Langmuir probe for different processing gas to Ar ratio at condition of 10 sccm Ar,  $\text{CF}_4/\text{O}_2$  (1/4 ratio), 1.5 A discharge current, 50 V extraction voltage, 3.5 mTorr processing pressure, 400 W ECWR source power, and 1.8 mT ECWR B-field.

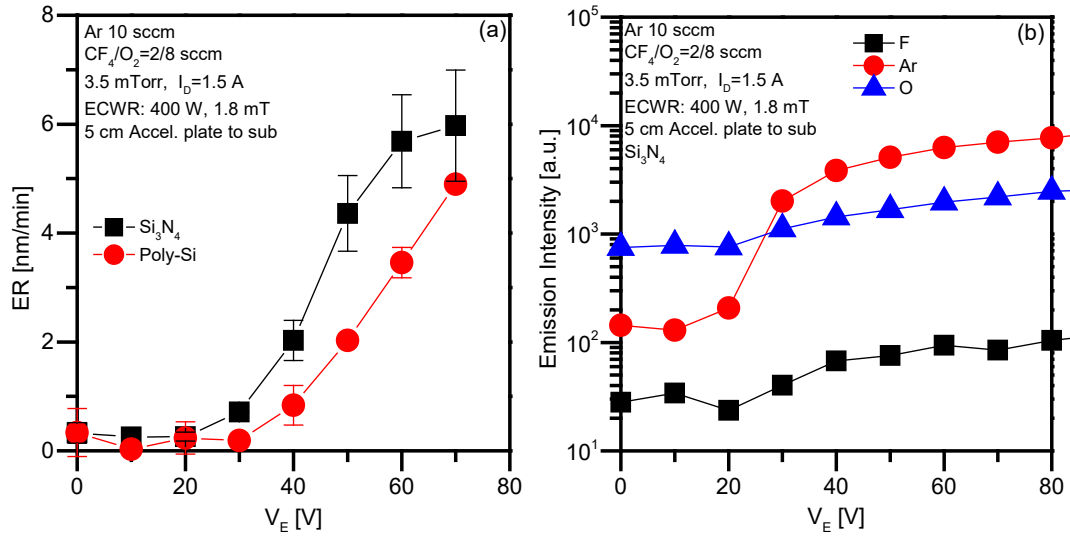


Fig. 4.9 (Color online) EB activated Si<sub>3</sub>N<sub>4</sub> / poly-Si surface etching with CF<sub>4</sub>/O<sub>2</sub> remote plasma: (a) ER vs  $V_E$  (b) optical emission of F, Ar, O intensities

### 4.3.3 Characterization of the combination of remote plasma radical source together with hollow cathode electron beam source

To explore the electron-radical synergy effect using this EB source at surfaces, Si<sub>3</sub>N<sub>4</sub> and poly-Si samples were exposed to the EB and fluxes of F and O radicals generated by the ECWR CF<sub>4</sub>/O<sub>2</sub> remote plasma. As described above, a neutralization plate made of electrically grounded aluminum plate covered with Kapton tape and a quartz plate to protect the plate from erosion allows only neutral radicals to diffuse from the ECWR plasma into the main chamber.<sup>4.42-4.44</sup> A 400 W source power level and 1.8 mT static magnetic field was applied for all ECWR experiments. In previous work, remote plasma etching, or chemical dry etching (CDE) of Si<sub>3</sub>N<sub>4</sub> and poly-Si etching using CF<sub>4</sub>/O<sub>2</sub> chemistries were studied.<sup>4.42-4.44</sup> Atomic oxygen oxidizes the CF<sub>4</sub> precursor to provide F radicals as an etchant in the downstream chamber. On the other hand, the oxygen will also oxidize the Si<sub>3</sub>N<sub>4</sub> and

poly-Si surfaces and slow down the etching of these materials, giving smaller etching rates (ER). The amount of oxygen relative to CF<sub>4</sub> is the key to control the substrate ER for the remote plasma operating conditions. When about 20% O<sub>2</sub> is used, the F radical generation rate is maximized and enables the highest ER of these materials. On the other hand, for O<sub>2</sub>-rich operating conditions like 80%O<sub>2</sub>/20%CF<sub>4</sub>, both the Si<sub>3</sub>N<sub>4</sub> and poly-Si ER can be suppressed by surface oxidation. This suppressed ER is preferred for the present EB enhanced etching study since it is desirable to reduce spontaneous Si<sub>3</sub>N<sub>4</sub> and poly-Si etching without EB irradiation. In the following tests, 2/8 sccm CF<sub>4</sub>/O<sub>2</sub> gas flows were used to generate remote radicals in the ECWR remote plasma source.

When the HC EB source extraction voltage,  $V_E$ , is increased, discharge-related optical emission along with material etching is observed. The Si<sub>3</sub>N<sub>4</sub> and poly-Si ER results are shown in Fig. 4.9 (a). Figure 4.9 (a) shows that Si<sub>3</sub>N<sub>4</sub> and poly-Si can be etched by EB in a remote CF<sub>4</sub>/O<sub>2</sub> plasma environment. The F (685.60 nm), Ar (750.39 nm), and O (777.19 nm) emission intensities measured by OES are shown in Fig. 4.9 (b). When the extraction energy is high enough to ionize the Ar/O<sub>2</sub>/CF<sub>4</sub> gas mixture (about  $V_E = 20$  V for Ar), secondary plasma emission can be observed with a relatively stable F and O concentration. However, the increase in ER with  $V_E$  in the 40-70 V range indicates that the etching behavior is not controlled by the radical density. At these conditions, arrival of beam electrons at the substrate surface appear to be the limiting factor for observing substrate etching due to an electron-neutral synergy effect.

The  $\text{Si}_3\text{N}_4$  surface is expected to be at floating potential, and for the same conditions, the poly-Si surface was grounded. A higher ER is seen for  $\text{Si}_3\text{N}_4$  than for poly-Si. It is possible that this is related to surface charging differences by electron induced negative charge accumulation for the  $\text{Si}_3\text{N}_4$  material. The increased negative surface charge for the  $\text{Si}_3\text{N}_4$  may enhance positive  $\text{Ar}^+$  ion bombardment from the EB plasma region, and induce more significant etching of the  $\text{Si}_3\text{N}_4$ . Some ion bombardment is unavoidable even at grounded conducting surfaces for this setup, since Ar ions of the electron-beam generated plasma are accelerated toward the sample surface by the sheath potential. The sheath potential should be controlled by the fairly high electron temperature  $T_e$  of the secondary plasma ( $\sim 5$  eV), beam electrons and surface electrical properties.

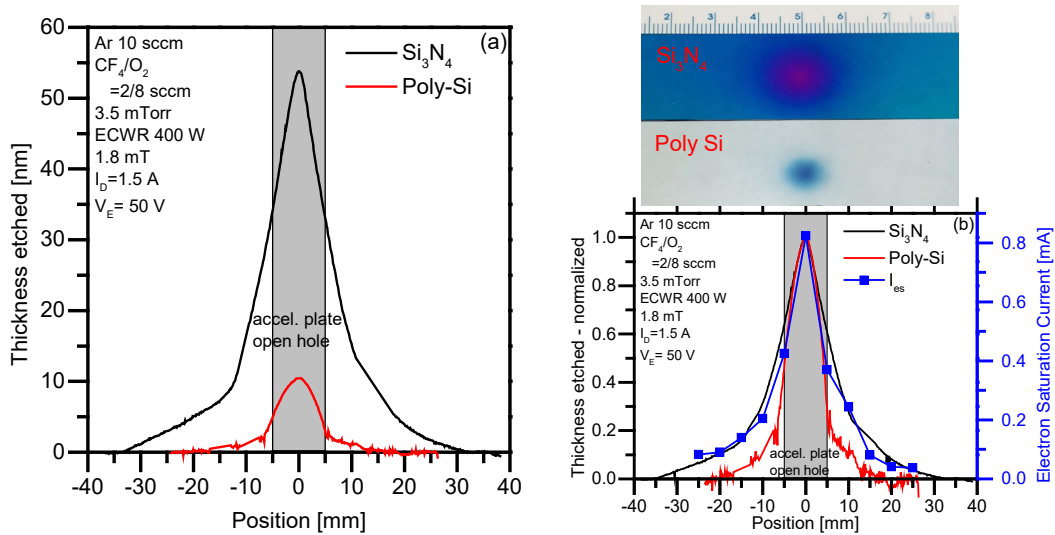


Fig. 4.10 (Color online) (a) Lateral etched thickness profiles of  $\text{Si}_3\text{N}_4$  and Poly-Si due to EB induced surface etching versus position. The etching times are 7 min for  $\text{Si}_3\text{N}_4$  and 2 min for Poly-Si. (b) Normalized etched thickness distribution and electron saturation current measured with a Langmuir probe setup versus position. Optical

photographs of etched sample surfaces showing etched thickness distribution by optical interference are shown on top.

In order to study the root cause of the EB induced etching, we scanned the etched thickness profiles across the  $\text{Si}_3\text{N}_4$  and poly-Si samples after etching using spatially resolved ellipsometry (Fig. 4.10 (a)). The experimental conditions used were the same as used for the LP measurements with a 2.5 cm source to sample distance, 3.5 mTorr main chamber pressure using  $\text{CF}_4/\text{O}_2$  at 2/8 sccm flow rates, 1.5 A discharge current and 50 V extraction voltage. The normalized ERs and the electron saturation current measured for the same lateral position obtained using the Langmuir probe are shown in Fig. 4.10(b). A circular etched shape is seen for both  $\text{Si}_3\text{N}_4$  and poly-Si surfaces. The center of the spot shows the highest electron saturation current intensity and corresponds to the highest surface ER. The ER located away from the EB (e.g. at 30 mm) is negligible. This suggests that the observed etching behavior is an electron beam controlled localized phenomenon and no spontaneous etching is seen for the oxygen-rich radical flux for the remote plasma operating conditions used here. The normalized etch depth of  $\text{Si}_3\text{N}_4$  in Fig. 4.10(b) shows a broader lateral profile than obtained with poly-Si. It is possible that this is related to surface charging differences, with increased surface charge accumulation for  $\text{Si}_3\text{N}_4$  repelling electrons from the center and increasing positive ion bombardment. The thickness etched is in the case of poly-Si only 10 nm, and it is possible that this limits the sensitivity of the ER measurement in this case away from the center. Figure 4.10 (b) shows that for most of the profile normalized EB current and etch depth are within a 30 mm diameter range and agree very well with each other.

#### 4.4 SUMMARY AND CONCLUSIONS

In this work, an EB etching system is developed that is based on Ar-based direct current (DC) hollow-cathode (HC) electron beam source and electron-beam injection into the downstream reactive environment of a remote  $\text{CF}_4/\text{O}_2$  plasma. The extraction voltage provides electron acceleration toward substrate, and can be used to independently control the primary electron beam energy. An EB induced secondary plasma can be excited when the primary electron beam energy is greater than the Ar ionization energy threshold. We have characterized the properties of the secondary plasma and surface etching of  $\text{Si}_3\text{N}_4$  and poly-crystalline Si (poly-Si) as a function of typical process parameters, including extraction voltage (0-70 V), discharge current of the HC discharge (1-2 A), pressure (2-100 mTorr), source to substrate distance (2.5 to 5 cm), and feed gas composition (with or without additional  $\text{CF}_4/\text{O}_2$  remote plasma). The electron energy probability function (EEPF) measured by Langmuir probe suggests two major components for this situation: a primary beam electron and low energy electrons produced by ionization of the Ar in the chamber. After combining the HC Ar EB with a  $\text{CF}_4/\text{O}_2$  ECWR remote plasma, both the low energy plasma electron and beam electron components decreased in the EEPF. An electron-neutral synergy etching effect has been observed for  $\text{Si}_3\text{N}_4$  and poly-crystalline silicon. The etching is confined to an area directly below the injected electron beam within a  $\sim 30$  mm diameter circle. This etched circular area is slightly broader for  $\text{Si}_3\text{N}_4$  than for poly-Si. No/little remote plasma spontaneous etching was observed outside the circular area coinciding with the location of beam electrons. The etching rate for poly-Si is smaller than that for  $\text{Si}_3\text{N}_4$ . This may be explained by additional ion

bombardment caused by the accumulation of a negative surface charge for the  $\text{Si}_3\text{N}_4$  surface, which is reduced for poly-Si.

## **ACKNOWLEDGMENTS**

The authors gratefully acknowledge the financial support of this work by Carl Zeiss SMS, and additional support by US Department of Energy (DE-SC0001939). The authors thank Dr. A. Knoll, Dr. P. Luan, A. Pranda, K.Y. Lin and A. Perruccio for helpful discussions and collaboration. They also thank Dr. Y. Raitses from Princeton Plasma Physics Laboratory for helpful discussions.

## **Chapter 5: Investigation of Hollow Cathode Plasma Electron Beam Etching of Si<sub>3</sub>N<sub>4</sub>**

C. Li, V. Godyak, T. Hofmann, K. Edinger and G. S. Oehrlein

### **ABSTRACT**

An etching system that employs an electron beam (EB) source based a direct current (DC) hollow-cathode (HC) Ar plasma to inject an electron-beam into the downstream reactive environment created by a remote CF<sub>4</sub>/O<sub>2</sub> plasma was developed and evaluated. This approach allows to deliver energy to a reactive surface by controlling the properties of the injected electron beam, and initiate surface etching. The primary electron beam energy is controlled by the extraction voltage relative to the HC discharge. For an extraction voltage greater than the ionization potential of Ar and/or process gas species, the energetic primary electrons can produce a secondary plasma in the process chamber. We have characterized the properties of the secondary plasma and also surface etching of Si<sub>3</sub>N<sub>4</sub> as a function of process parameters, including extraction voltage (0-80 V), discharge current of the HC discharge (1-2 A), pressure (3.5-20 mTorr), source to substrate distance (1.5 to 5 cm), and feed gas composition (20% and 80% O<sub>2</sub> in CF<sub>4</sub>/O<sub>2</sub>). The electron energy probability function (EETF) measured with a Langmuir probe about 2.5 cm below the extraction ring suggests several major components for this situation, in particular primary beam electrons with an energy which varies as the extraction voltage is changed and low energy electrons produced by ionization of the Ar gas in the process chamber into which the electron beam is injected. When a remote CF<sub>4</sub>/O<sub>2</sub> plasma is additionally coupled to the process chamber, Si<sub>3</sub>N<sub>4</sub> etching can take place. For conditions without EB injection, the remote

plasma etching rate of  $\text{Si}_3\text{N}_4$  depends strongly on the  $\text{O}_2$  concentration in the  $\text{CF}_4/\text{O}_2$  processing gas mixture and can be suppressed for  $\text{O}_2$ -rich process conditions. A  $\text{SiONF}$  passivation layer is formed in this case on the  $\text{Si}_3\text{N}_4$  surface, which reduces the  $\text{Si}_3\text{N}_4$  ER. Combining the HC EB source with the remote plasma (EB-RP) makes it possible to induce  $\text{Si}_3\text{N}_4$  etching for the  $\text{O}_2$ -rich remote plasma conditions where remote plasma by itself produces negligible  $\text{Si}_3\text{N}_4$  etching. A strong dependence on  $\text{O}_2/\text{CF}_4$  mixing ratio is also observed for EB enhanced etching. The ratio of gas phase F and O densities as estimated from optical emission is in this case only controlled by the gas mixing ratio and independent of EB operating conditions. For the EB-RP, the extraction voltage can be used to control the beam electron energy and is shown to be an effective method to control surface etching of  $\text{Si}_3\text{N}_4$ . For the conditions evaluated, the discharge current is not the limiting factor for  $\text{Si}_3\text{N}_4$  etching. The main chamber pressure will affect the EB plasma density. High pressure can cause more ion-bombardment etching or even metal deposition by Ar sputtering of the anode plate. Over the range investigated, the EB source to sample distance has little impact on the plasma discharge. For low EB source-sample separation electron losses to surrounding surfaces are minimized and leads to a high  $\text{Si}_3\text{N}_4$  ER. After optimization of all parameters, EB controlled  $\text{Si}_3\text{N}_4$  etching has been established without spontaneous etching.

## 5.1 INTRODUCTION

Angstrom level precision etching processes are essential for fabrication of semiconductor devices with nm critical dimensions.<sup>5.1-5.4</sup> Traditional plasma-based dry etching techniques utilize ion bombardment to achieve material removal either physically<sup>5.5</sup> or by synergistic interactions with added reactive chemical species<sup>5.6-5.15</sup>. Recently, a new electron-based etching technique utilizing a hollow cathode (HC) plasma discharge for electron beam (EB) extraction with low and adjustable electron energy for surface etching has been developed, which is based on an argon HC discharge with additional extraction voltage to accelerate electron beam onto the material surface in a reactive remote plasma environment. This HC EB etching system enables operation in a relatively high pressure (~mTorr) reactive gas environment created by a remote plasma source that provides reactive radicals for achieving electron enhanced chemical etching. In the present article, we describe a more systematic parametric study required for an improved understanding of this system.

This article is organized as follows: in the first part, the authors discuss the precursor composition impact of Si<sub>3</sub>N<sub>4</sub> etching in a CF<sub>4</sub>/O<sub>2</sub> remote plasma etching environment and identify process conditions for which the Si<sub>3</sub>N<sub>4</sub> etching rate can be minimized. Additionally, EB enhanced etching of Si<sub>3</sub>N<sub>4</sub> with varying extraction voltages is studied. In the second part, the authors study electron enhanced chemical surface etching of Si<sub>3</sub>N<sub>4</sub> for the conditions where the HC electron beam source is combined with the effluent of the CF<sub>4</sub>/O<sub>2</sub> remote plasma source. The impacts of varying extraction voltage, discharge current, main chamber pressure and operation

distance are examined using optical emission for discharge characterization and ellipsometry for surface etching. In the last part, the authors report optimized process conditions and demonstrate EB controlled Si<sub>3</sub>N<sub>4</sub> etching.

## 5.2 EXPERIMENTAL

The experiments were performed in an electron beam etching system, consisting of a hollow cathode (HC) EB source on top of a reaction chamber connected to an electron cyclotron wave resonance (ECWR) remote plasma source on the side (Fig. 5.1(a)) that has been previously described in Chapter 4. For convenience, part of this description has been duplicated here. The base pressure achieved before processing was in the  $1 \times 10^{-6}$  Torr range. The pressure in the HC source ( $\sim$ Torr level) is significantly higher than the chamber pressure below because of a choked flow connection. The pressure in the reaction chamber during processing was kept at 2-100 mTorr using a butterfly valve in the pumping line. The ECWR remote plasma source consists of a COPRA DN160 ECWR plasma beam source running at 13.56 MHz radio frequency with a modified neutralization plate<sup>16</sup>. A 400 W source power level and 1.8 mT static magnetic fields were applied in the ECWR work for all experiments requiring the injection of reactive radicals.<sup>5,16</sup> The CF<sub>4</sub>/O<sub>2</sub> remote plasma is a well-developed method to generate reactive neutral radicals (F radical) for Si<sub>3</sub>N<sub>4</sub> etching.<sup>5,17</sup>

Argon gas was admitted to the HC discharge using a mass flow controller. The EB source to substrate distance can be controlled with an adjustable bellows tube over a range of 70 mm. A DC power supply providing constant discharge current ( $I_D$ ) was used to generate the main HC plasma discharge between the cathode and the

source anode. A second DC power supply provided an extraction voltage ( $V_E$ ) to the anode plate to accelerate a beam of electrons through the center hole (10 mm diameter) of the grounded acceleration plate toward the grounded substrate. The acceleration plate to HC anode plate distance is 10 mm.

The equivalent circuit diagram is shown in Fig. 5.1 (b). The arrows depict the direction in which electrons move and is opposite to the conventional current direction. The HC discharge provides an electron current  $I_D$ . Typical EB source operating conditions are 10 sccm Ar carrier gas flow for a constant 1.5 A discharge current ( $I_D$ ). The net DC current measured at the grounded substrate is denoted with  $I_B$ .

The electron beam and the secondary plasma generated have been characterized using a Langmuir probe (LP). The LP used in this study is designed to collect highly accurate measurements of the electron energy probability function (EPPF), electron density ( $n_e$ ), and electron temperature ( $T_e$ ) by fast sweep speeds, ion bombardment cleaning, and electron heating.<sup>5.29-5.31</sup>

The Ar emission at wavelengths of 750.39 nm was measured by optical emission spectrometer (OES) as the energy of the extracted EB was varied. F and O emissions were also monitored at wavelengths of 685.60 nm and 777.19 nm, respectively.

Sample surface etching and modification were monitored in real time with an *in situ* ellipsometer setup that used a HeNe laser ( $\lambda = 632.8$  nm).

After processing, selected samples were transferred under vacuum to a Vacuum Generators ESCALAB MK II surface analysis system for X-ray Photoelectron Spectroscopy (XPS) measurements. High-resolution scans of the Si2p, C1s, O1s, N1s, and F1s binding energy regions were obtained at 20 eV pass energy at an electron take-off angle of 90° and 20° with respect to the sample surface. The spectra were fitted using least-squares fitting routines with 70/30 % Gaussian/Lorentzian line shapes at fixed full width at half maximum (FWHM) for each spectrum after Shirley background subtraction.<sup>5.9, 5.12, 5.14</sup>

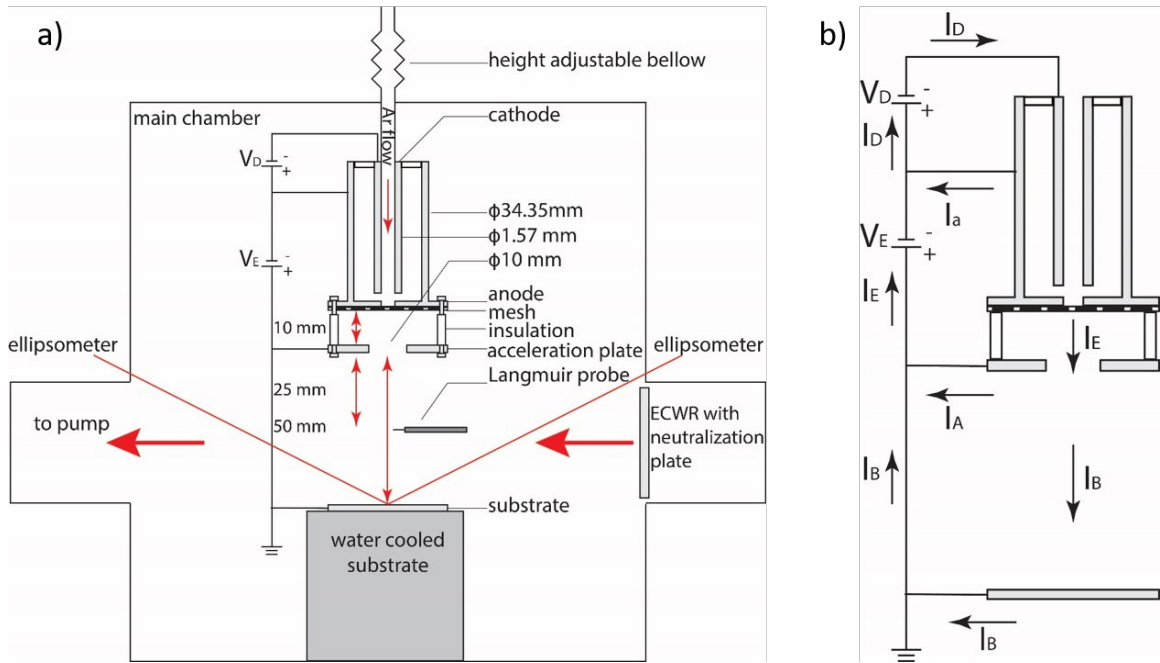


FIG. 5.1 (Color online) (a) Schematic overview of the experimental layout of the multi-chamber tool and (b) notations of currents and voltages of the electrical setup.

## 5.3 RESULTS AND DISCUSSION

### 5.3.1 Impact of precursor composition on remote plasma etching

As a basis of studying the EB enhanced chemical etching, the remote plasma environment characterization with surface responses is required as a first step.

Remote plasma etching results for  $\text{Si}_3\text{N}_4$  as a function of varying  $\text{CF}_4/\text{O}_2$  gas flow ratio are shown in Fig. 5.2. Operating conditions were variable  $\text{CF}_4/\text{O}_2$  gas mixtures with a total gas flow rate of 50 sccm into the ECWR chamber, a source power of 400 W and 1.8 mT DC magnetic fields. Simultaneously, 60 sccm Ar gas flowed through the HC EB system, which protected the HC system from the reactive radicals generated by the remote plasma, and also provided consistent conditions in the main chamber relative to EB operation. The main chamber pressure is held at 20 mTorr, which is higher than the pressure used for EB etching (3.5 mTorr) and enhances the etching rates due to the remote plasma only. The  $\text{Si}_3\text{N}_4$  etching rate (ER) is converted into reacted F using the  $\text{Si}_3\text{N}_4$  density with the assumption that one Si atom consumes four F atom for volatilization. Figure 5.2 shows that the surface reacted F initially increases with precursor  $\text{O}_2$  concentration added to  $\text{CF}_4/\text{O}_2$  and peaks at 20%  $\text{O}_2$ . This classic effect is due to oxidation of the  $\text{CF}_4$  gas, which provides more F atoms for material removal. With more  $\text{O}_2$  in the precursor gas mixture, the F will be diluted and the surface reacted F will drop.<sup>5.19</sup> Gas phase F and O densities were evaluated using optical emission spectroscopy. For this F and O emission intensities were normalized relative to Ar emission under the same conditions. The O emission increases with  $\text{O}_2$  flow, whereas the F emission shows a peak at 20%  $\text{O}_2$  concentration, which is consistent with the surface reacted F trend. However, at 40%  $\text{O}_2$  concentration the surface reacted F rate drops faster than gas phase F, indicating that a passivation or oxidation layer on the surface suppresses the etching of  $\text{Si}_3\text{N}_4$ . At 80%  $\text{O}_2$  concentration, the  $\text{Si}_3\text{N}_4$  etching rate has dropped to the baseline level even though there is still available gas phase F indicated by the OES measurements. The

lack of  $\text{Si}_3\text{N}_4$  etching can be explained by oxygen-related surface passivation. This is the optimal condition to study for EB enhanced etching, since for this situation spontaneous etching due to reactive radicals produced by the remote plasma has become negligible, whereas the EB can be used to activate surface etching with residual F atoms still available.

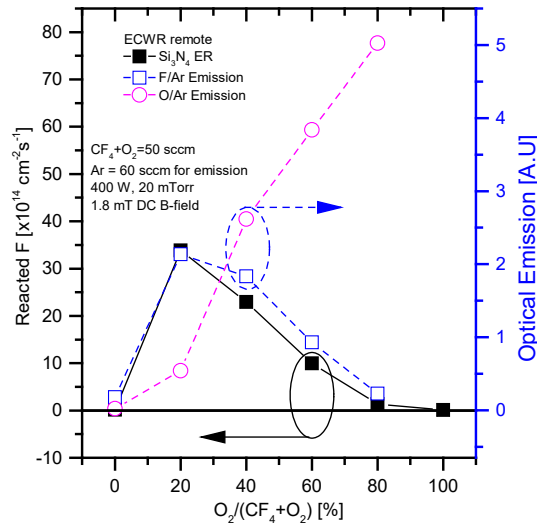


FIG. 5.2 (Color online) ECWR remote plasma etching characterized by converting  $\text{Si}_3\text{N}_4$  etching rate into surface reacted F as a function of  $\text{O}_2$  to  $\text{CF}_4+\text{O}_2$  flow ratio. Ar emission (751 nm) is used to normalize optical emission intensities of F (703 nm) and O (777 nm) and these ratios are also shown. When  $\text{O}_2$  concentration is greater than 20%, surface passivation/oxidation suppressed the  $\text{Si}_3\text{N}_4$  surface reaction. At 80%  $\text{O}_2$  concentration,  $\text{Si}_3\text{N}_4$  etching has ceased even though there is still a small amount of gas phase F shown by the OES measurements.

To further confirm surface passivation,  $\text{Si}_3\text{N}_4$  samples after remote plasma etching using different  $\text{O}_2/\text{O}_2+\text{CF}_4$  processing gas ratios were transferred under vacuum into a surface analysis system and analyzed by XPS. Figure 5.3 shows several important  $\text{Si}_3\text{N}_4$  surface chemistry data obtained by XPS analysis of  $\text{Si}_3\text{N}_4$

processed using different O<sub>2</sub> concentrations in the remote CF<sub>4</sub>/O<sub>2</sub> plasma. A comparison with data obtained with a pristine Si<sub>3</sub>N<sub>4</sub> sample is also shown. The electron emission angle is 20 degrees relative to the sample surface, which enables an analysis of the top 2-3 nm from the surface. With the addition of O<sub>2</sub> in plasma, there is no surface carbon contamination shown in C1s spectra. A SiOF layer was observed in Si2p spectra, which is the oxidation passivation layer as we discussed above.

By applying an attenuation model to SiN intensities in Si2p spectra with two different probe angles, the thickness of the surface SiONF layer can be obtained.<sup>5.32</sup> The Si<sub>3</sub>N<sub>4</sub> ERs are plotted versus angle-resolved XPS (AR-XPS) passivation layer thicknesses (Fig. 5.4). The data show that as the passivation layer thickness increased, the Si<sub>3</sub>N<sub>4</sub> ER is reduced. Again, the 80% O<sub>2</sub> concentration condition for CF<sub>4</sub>/O<sub>2</sub> shows baseline level etching with sufficient SiONF passivation layer thickness. This fairly thick passivation layer which still contains F atoms is a promising basis of applying the EB to induce a surface reaction. The F atoms in this layer are expected to react and produce surface etching as energy is delivered to this surface upon electron beam injection into the gas above the sample.

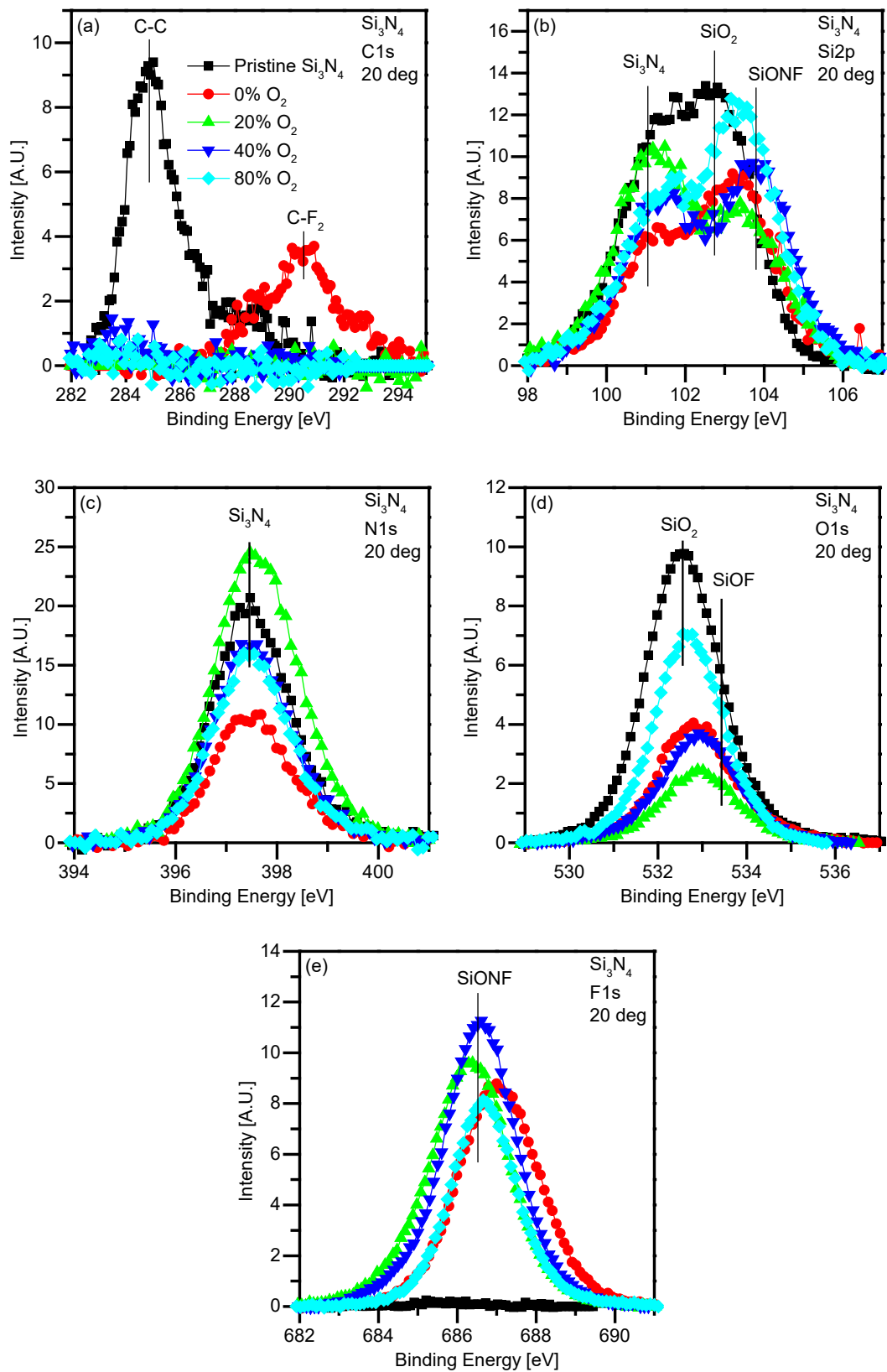


FIG. 5.3 (Color online)  $\text{Si}_3\text{N}_4$  surface XPS data after processing using different  $\text{O}_2$  concentrations in the  $\text{CF}_4/\text{O}_2$  remote plasma. Data obtained with a pristine  $\text{Si}_3\text{N}_4$  surface with native oxide is also compared in 20-degree probe angle XPS spectra of (a) C1s (b) Si2p (c) N1s (d) O1s (e) F1s. With the addition of  $\text{O}_2$  in plasma, there is no surface carbon contamination. A SiOF layer was observed on top of  $\text{Si}_3\text{N}_4$  surface.

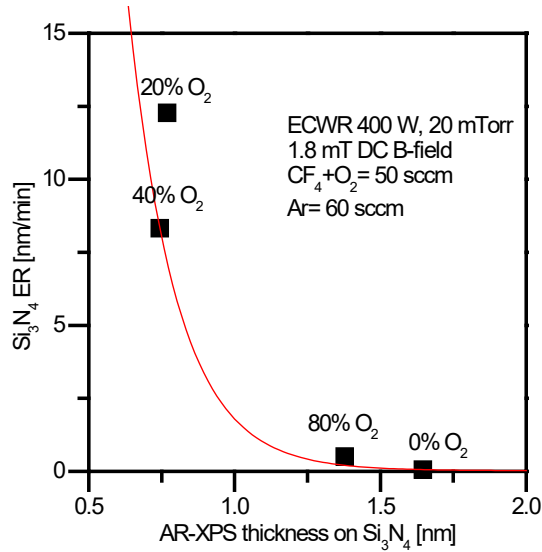


FIG. 5.4 (Color online)  $\text{Si}_3\text{N}_4$  remote plasma etch rate vs passivation layer thickness determined by angle resolved XPS.

### 5.3.2 Hollow cathode plasma-electron beam induced etching

Based on the background remote plasma results, two representative  $\text{CF}_4/\text{O}_2$  gas flow ratios were studied in HC EB enhanced etching conditions. The EB etching condition is the standard condition for most cases reported in Chapter 4. To reduce the interaction of the EB with the gas atoms and molecules, for this work the pressure in the main chamber was reduced to 3.5 mTorr, which required to reduce both the Ar and  $\text{CF}_4/\text{O}_2$  flows accordingly. The Ar flow rate in the HC is 10 sccm with a discharge current of 1.5 A. The source to sample distance is 5 cm. The  $\text{CF}_4/\text{O}_2$  gas mixture with a total gas flow rate of 10 sccm is injected into ECWR chamber with a

source power of 400 W and a DC magnetic field of 1.8 mT. The main chamber pressure was held at 3.5 mTorr for all experiments.

Fig. 5.5 (a) shows the ER results by varying the extraction voltage for two  $\text{CF}_4/\text{O}_2$  gas mixtures using either 20% or 80%  $\text{O}_2$ . As described in Chapter 4, when  $V_E$  is greater than the gas ionization threshold, plasma-related emission can be observed along with an enhancement of the substrate etching rate. For the 20%  $\text{O}_2$  concentration case, the  $\text{Si}_3\text{N}_4$  ER is over 5 times greater than for 80%  $\text{O}_2$  with some spontaneous etching without  $V_E$ . This enhanced ER indicates that for the 80%  $\text{O}_2$  condition, the F etchant density is the limiting factor for surface etching. By increasing the F radical concentration, we could dramatically increase the  $\text{Si}_3\text{N}_4$  ER. The F and O emission intensities normalized by the Ar emission in the EB secondary plasma conditions are shown in Fig. 5.5 (b). For the same gas composition, the F and O emissions are unchanged with  $V_E$ . Only the gas composition can change the radical density in the chamber environment.

As discussed in Chapter 4, while the exact surface interaction mechanism by which the injected electrons initiate substrate etching is unclear at this time, e.g. the role of beam electrons versus energetic ion bombardment from the secondary plasma, it is clear that the root cause of the observed etching is the injection and acceleration of the electron beam.

In the following studies, we only focus on the F deficient condition (80%  $\text{O}_2$  concentration) for which spontaneous etching becomes negligible. We use Ar emission to characterize the plasma density.

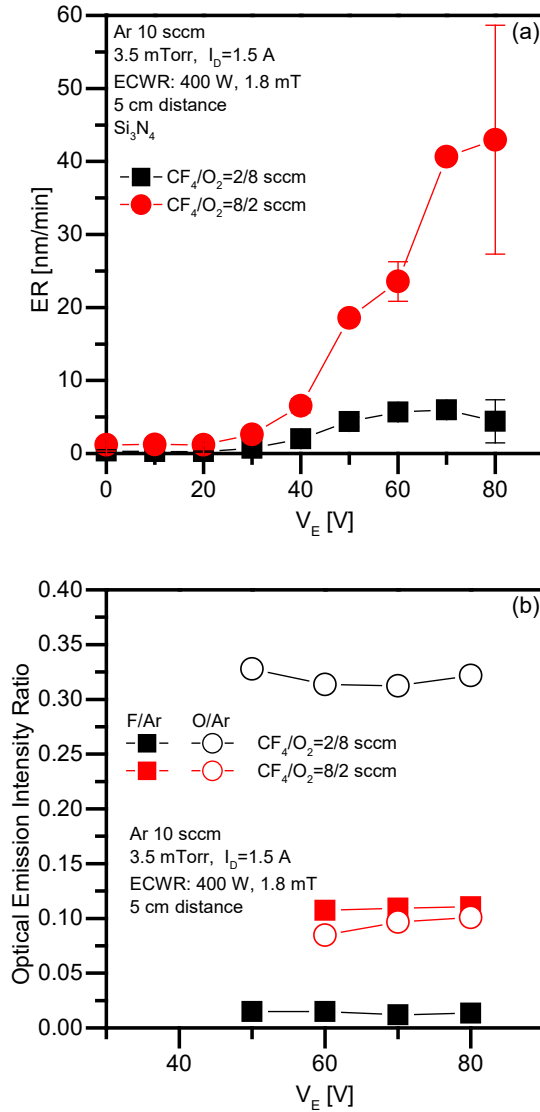


FIG. 5.5 (Color online) Electron-beam activated  $\text{Si}_3\text{N}_4$  surface etching with  $\text{CF}_4/\text{O}_2$  remote plasma in two different gas ratios: (a) ER vs  $V_E$ . (b) Optical emission of Ar normalized F and O intensities.

The corresponding EEPF in 80%  $\text{O}_2$  concentration condition with varying  $V_E$  measured by Langmuir probe (LP) is shown in Fig.6. As discussed in Chapter 4, the LP EEPF result for EB condition consists of two major peaks: one peak located at lower energy represents electrons due to the EB induced plasma with fairly low average electron temperature; the peak at a high electron energy that shifts strongly

with  $V_E$  and corresponds to the anisotropic primary beam electron with low to no inelastic collisions. The beam electron peak energy is proportional to the extraction voltage  $V_E$ . In figure 5.6, the corresponding beam electron energy increases with  $V_E$  from 40-80 V with a similar peak area. This finding agrees with the results reported for the Ar EB in Chapter 4.

By comparing the LP data with the ER data shown in Fig. 5.5(a) at  $V_E$  in 60-80 V range, we note that the ER for the  $\text{CF}_4/80\% \text{O}_2$  case has reached a saturation value and does not increase further even though the beam electron energy increases. This confirms the conclusion above, that the etching rate in that extraction voltage range (60-80 V) is limited by the F etchant. Conversely, for the  $\text{CF}_4/20\% \text{O}_2$  case which is characterized by a high gas phase F density, the  $\text{Si}_3\text{N}_4$  ER continues to increase. In the following sections, the other EB parameters will be studied in the same fashion with varying extraction voltage.

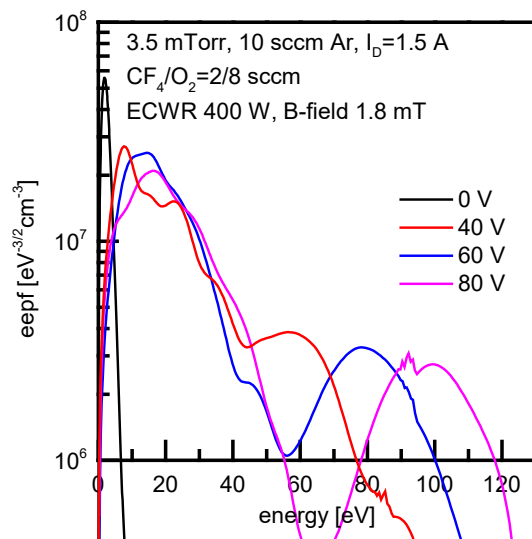


FIG. 5.6 (Color online) Electron energy probability function (EPPF) measured by Langmuir probe for Ar EB in  $\text{CF}_4/\text{O}_2$  remote plasma condition with varying

extraction voltage  $V_E$ . The EEPF of EB generated plasma consists of two major peaks, one of which changes strongly with  $V_E$ .

### 5.3.3 Discharge current, pressure, distance impacts on HC EB enhanced $\text{Si}_3\text{N}_4$ etching

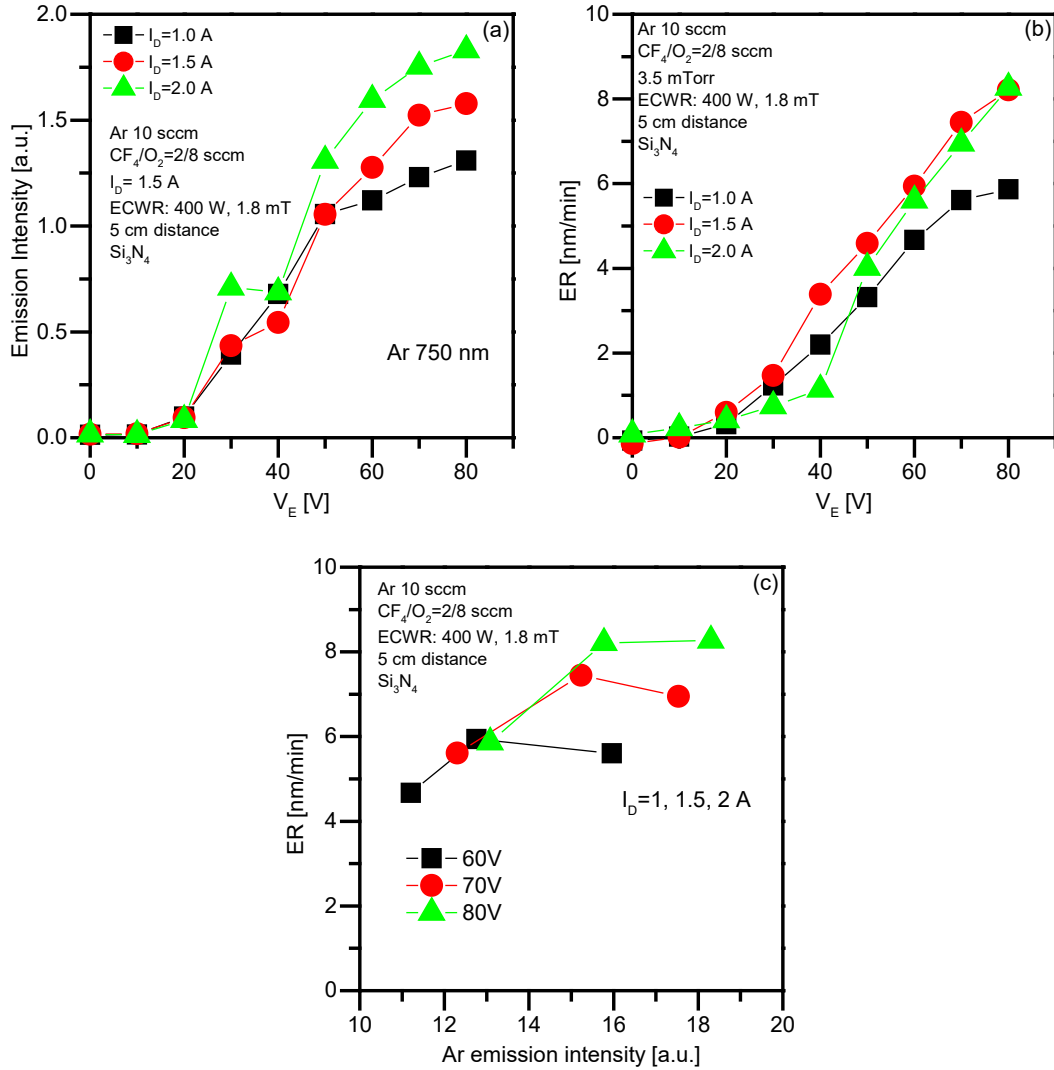


FIG. 5.7 (Color online) (a) Ar emission intensity and (b) Si<sub>3</sub>N<sub>4</sub> ER vs extraction voltage for different discharge current. (c) The corresponding ER vs Ar emission for selected  $V_E$ .

To further characterize the behavior of EB enhanced etching, the Ar emission intensity and Si<sub>3</sub>N<sub>4</sub> ER at various extraction voltages were evaluated for the other EB source parameters, i.e. discharge current ( $I_D$ ), pressure in the main chamber, and acceleration plate to substrate distance. The Ar emission intensity characterizes excited Ar atoms and Chapter 4 shows that this behaves very similar to EB induced plasma density. The variation of Ar emission intensity and Si<sub>3</sub>N<sub>4</sub> ER as a function of extraction voltage ( $V_E$ ) with three different discharge currents ( $I_D$ ) are shown in Figs. 7 (a) and 7 (b), respectively. With increased discharge current  $I_D$  (Fig. 5.7 (a)) Ar emission intensity increases for all acceleration voltages. This indicates that the EB induced secondary plasma density is proportional to the total EB current controlled by  $I_D$ , consistent with the expectations. In contrast to the Ar emission intensity, the Si<sub>3</sub>N<sub>4</sub> ER increases  $I_D$  was changed from 1 A to 1.5 A at same  $V_E$ , but then stays the same when  $I_D$  is increased further to 2 A. To further investigate this phenomenon, Si<sub>3</sub>N<sub>4</sub> ER is plotted versus Ar emission intensity at three different  $V_E$  (Fig. 5.7(c)). It clearly shows that the Si<sub>3</sub>N<sub>4</sub> ER at same  $V_E$  increases initially with Ar emission (or plasma density) and saturate at 2 A discharge current. This plot suggests that the ER depends on both  $V_E$  and plasma density, but that ultimately both plasma density and  $V_E$  are no longer limiting the etching rate for these conditions. This regime likely corresponds to a limitation by the arrival of F radicals at the surface, and corresponds to neutral limited etching. Fig. 5.7(c) strongly suggests that the delivery of both energy and reactive F neutrals to the surface are required. The fact that the Si<sub>3</sub>N<sub>4</sub> ER increases with  $V_E$  at those three extraction voltage conditions at 1.5 A, suggests that for these

conditions, independent of EB plasma density, beam electron energy has a direct impact and is the root cause of  $\text{Si}_3\text{N}_4$  etching.

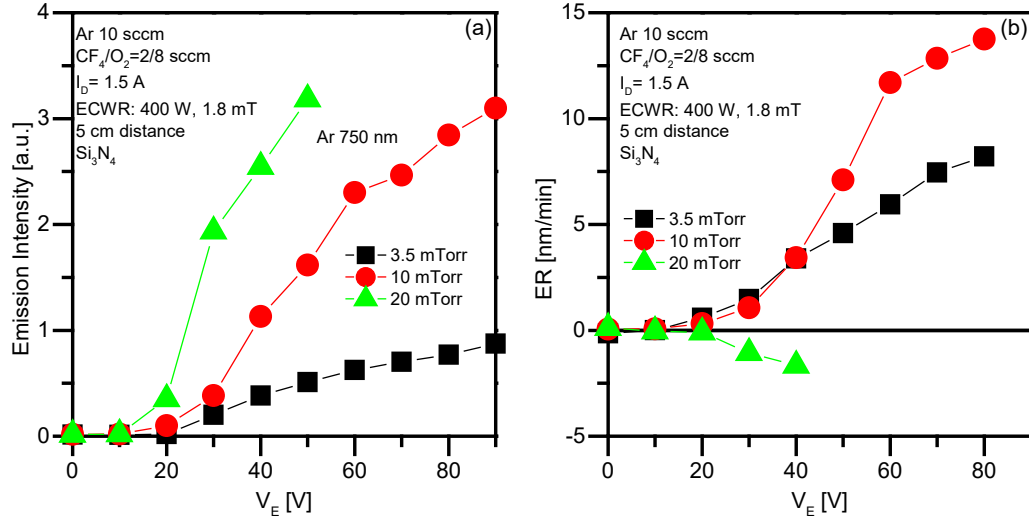


FIG. 5.8 (Color online) (a) Ar emission intensity and (b)  $\text{Si}_3\text{N}_4$  ER vs extraction voltage for different pressure.

The variation of Ar emission intensity and  $\text{Si}_3\text{N}_4$  ER as a function of extraction voltage ( $V_E$ ) with three different main chamber pressures are shown in Figs. 8 (a) and 8 (b), respectively. With increased chamber pressure, the ionization in the main chamber increases and leads to an increase of Ar emission. The EEPF data obtained by LP measurements show an increase of the low energy EB plasma electrons along with a drop of the high energy beam electrons. Since low energy EB plasma electron density and Ar emission intensity are both representing the EB plasma density, the increase of the low energy electron distribution is consistent with the increase of the Ar emission intensity at high main chamber pressure condition. For the same  $V_E$ , the  $\text{Si}_3\text{N}_4$  ER increases with pressure up to 10 mTorr, and may be explained by the increase in plasma density which causes more energy delivery to the  $\text{Si}_3\text{N}_4$  surface, e.g. in the form of more low ion bombardment of the negatively

charged dielectric substrate surface. At 20 mTorr an increase of the  $\text{Si}_3\text{N}_4$  thickness is seen which could be related to re-deposition. When the main chamber pressure increases to 20 mTorr, the high density of EB plasma will sputter the EB source metal and causes metal deposition on the surface. Both of these high-pressure effects are unwanted for EB enhanced etching.

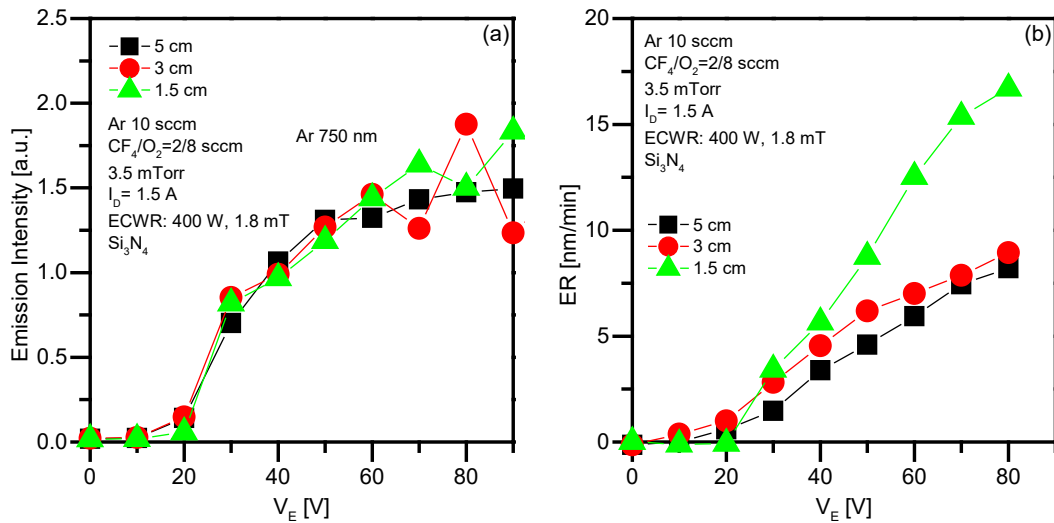


FIG. 5.9 (Color online) (a) Ar emission intensity and (b)  $\text{Si}_3\text{N}_4$  ER vs extraction voltage for different EB source to sample distances.

As the distance between the extraction electrode and the substrate electrode is varied, the relative importance of electron interactions with gas phase species or surface species changes. However, with the  $\text{CF}_4/\text{O}_2$  processing gas, this change is relatively small, which may be due in part to electron attachment to the electronegative gas species from the  $\text{CF}_4/\text{O}_2$  mixture. The electrons are more likely to be attached to the processing gas and will lead to a relatively shorter electron mean free path, which makes it difficult to detect the discharge difference in this 5 cm range. For this reason, when changing this distance from 5 cm to 1.5 cm (Fig. 5.9 (a)) the Ar emission stays the same. However, the  $\text{Si}_3\text{N}_4$  ER increases dramatically when

the distance is as short as 1.5 cm (Fig. 5.9 (b)). In that case, the sample surface will collect more electrons and higher ER results.

#### 5.4 Process conditions suitable for EB controlled Si<sub>3</sub>N<sub>4</sub> etching

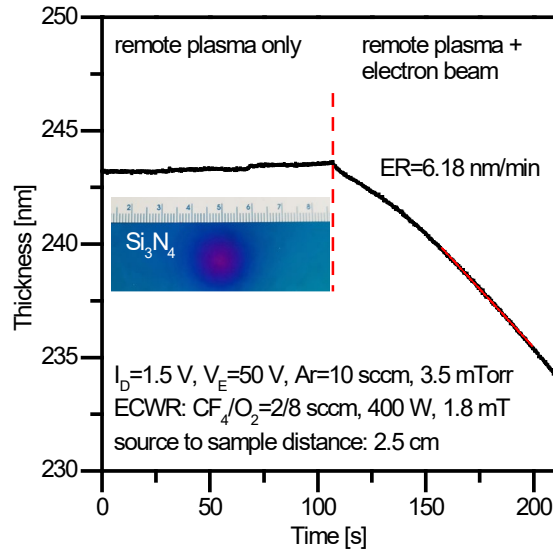


FIG. 5.10 (Color online) Si<sub>3</sub>N<sub>4</sub> thickness time evolution before and after electron beam injection. No spontaneous etching is observed without electron beam. After applying an extraction voltage  $V_E=50$  V, Si<sub>3</sub>N<sub>4</sub> is etched by electron chemical synergy effect with a etch rate of 6.18 nm/min. In the inset, an optical micrograph is shown that was obtained after extended etching and shows the localized etching effect.

After investigating the impact of the precursor chemistry composition, extraction voltage, discharge current, main chamber pressure and the operation distance, suitable conditions for EB enhanced etching were identified. To avoid spontaneous etching from background remote plasma, a high oxygen concentration in the CF<sub>4</sub>/O<sub>2</sub> mixture is required to form a SiONF passivation layer on the Si<sub>3</sub>N<sub>4</sub> surface. As the key parameter of ER control, the extraction voltage needs to form an energetic electron beam with energy delivery to the reacted surface that is high enough to lead to observable surface etching. The discharge current is desired in the

saturation region and enables sufficient energy delivery to the surface so that material etching is limited by other factors. In order to minimize secondary plasma production and ion bombardment impact from plasma, the main chamber pressure is preferred to be low but high enough so that the reactive radical delivery is sufficient. A small source to sample distance can minimize the electron loss to surrounding walls and enhance the electron beam etching efficiency. With the above considerations, suitable Si<sub>3</sub>N<sub>4</sub> EB etching conditions can be realized using 80% O<sub>2</sub> in CF<sub>4</sub>/O<sub>2</sub> mixture, 50 V extraction voltage, 1.5 A discharge current, 3.5 mTorr main chamber pressure, and 2.5 cm source to sample distance. An exemplary Si<sub>3</sub>N<sub>4</sub> thickness time evolution at this condition is shown in Fig. 5.10 before and after EB injection. No spontaneous etching is observed without energizing the electrons from the HC electron source. After applying an extraction voltage  $V_E=50$  V, Si<sub>3</sub>N<sub>4</sub> is etched at a steady level by electron-beam-reactive radial synergy effect with an etch rate of 6.18 nm/min.

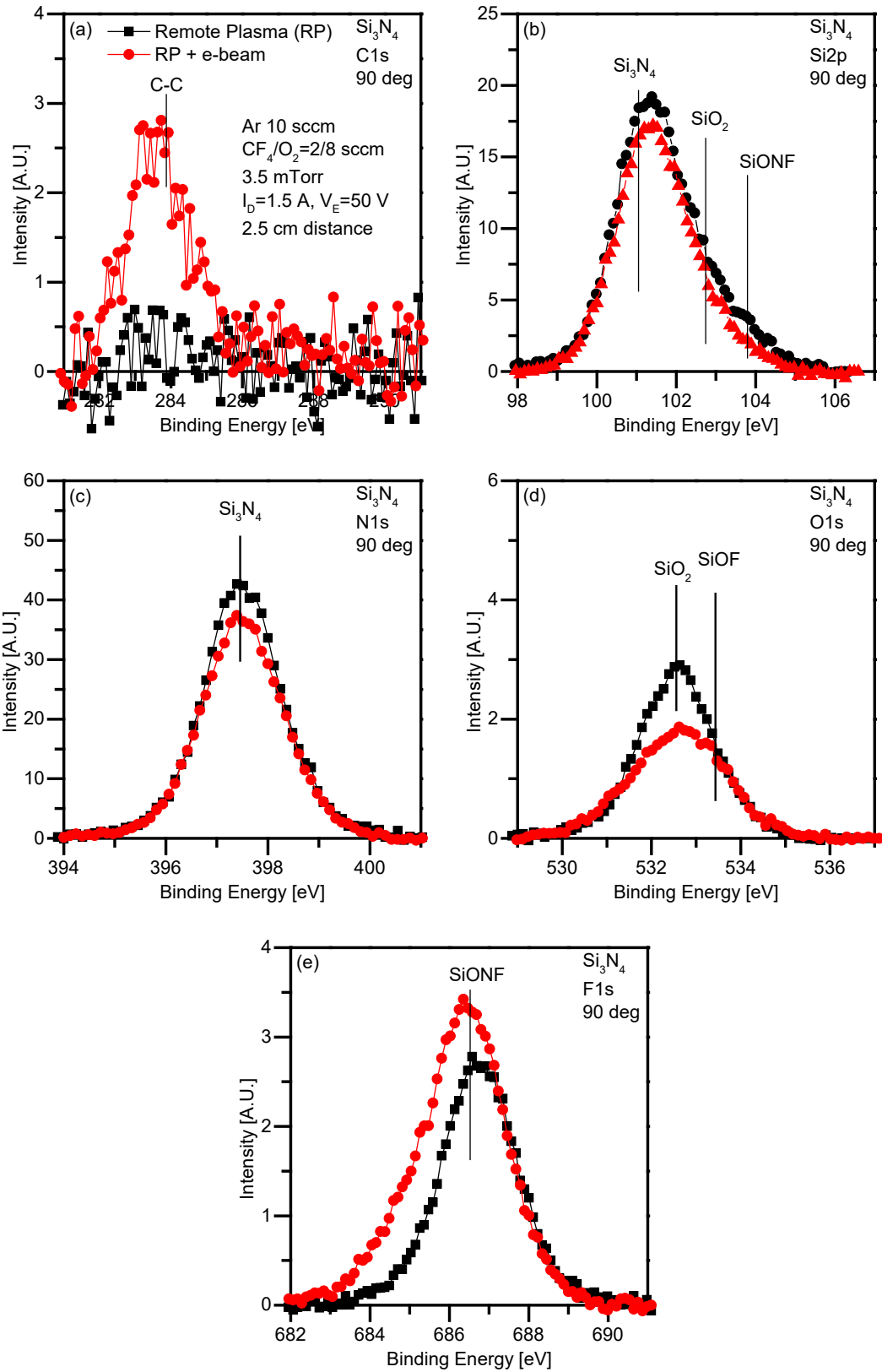


FIG. 5.11 (Color online)  $\text{Si}_3\text{N}_4$  surface chemistry scanned by XPS under 80%  $\text{O}_2$  concentration in  $\text{CF}_4/\text{O}_2$  remote plasma with (red) and without (black) EB activation. The geometry was 90-degree emission angle for photoelectrons. XPS spectra of (a) C1s (b) Si2p (c) N1s (d) O1s (e) F1s are shown.

The surface chemistry of  $\text{Si}_3\text{N}_4$  samples for optimistic etching conditions with and without EB activation has been investigated and selected results are shown in Fig. 5.11. Since the etched surface is not a uniform distribution, we only used the 90-degree photoelectron probe angle to minimize the area being analyzed. For the  $\text{Si}_3\text{N}_4$  etching conditions used, the remote plasma chemistry effect has been reduced due to lower chamber pressure. The low EB source to sample distance generates locally a higher Ar partial pressure and dilutes the radical density near the sample surface. As a result, a traceable amount of carbon is shown in the C1s spectra relative to remote plasma only. The EB etched  $\text{Si}_3\text{N}_4$  sample surface also shows a decreased XPS intensity of Si2p, N1s and O1s and a stronger intensity in F1s relative to the remote plasma etched  $\text{Si}_3\text{N}_4$ . This surface chemistry change may indicate an electron-stimulated removal of the nitrogen and oxygen from the SiONF passivation layer with precursor attachment. It is consistent with the two-step etching mechanism reported in FEB etching of  $\text{SiO}_2$  that involves electron-stimulated desorption of oxygen from the  $\text{SiO}_2$  matrix followed by the precursor-mediated removal of elemental silicon<sup>5,33</sup>.

## 5.5 SUMMARY AND CONCLUSIONS

In this work, a systematic investigation of the parameter space available for an etching approach based on beam electron controlled  $\text{Si}_3\text{N}_4$  etching has been performed by characterizing the combination of an HC EB for energetic beam electron generation with a remote plasma source for reactive radical. The  $\text{O}_2$

concentration of the  $\text{CF}_4/\text{O}_2$  processing gas mixture strongly impacts the remote plasma etching rate of  $\text{Si}_3\text{N}_4$ . A SiONF passivation layer is formed on the surface for  $\text{O}_2$  rich conditions, which reduces the  $\text{Si}_3\text{N}_4$  ER. Combining the HC EB source with the remote plasma, a strong precursor dependence has been observed in EB enhanced etching. The gas phase F and O densities are controlled by the gas mixing ratio and remote plasma operating conditions and independent of EB operating conditions. Similar to pure Ar EB, the extraction voltage will control the beam electron energy, and provides an effective method to control surface etching. Other parameters, such as discharge current, process chamber pressure, and EB source to sample distance were studied by evaluating Ar optical emission and ER for various extraction voltages. For the conditions evaluated, the discharge current is not the limiting factor for  $\text{Si}_3\text{N}_4$  etching. The main chamber pressure affects the EB induced plasma density. Higher pressure operation causes more etching, but ultimately leads to undesirable redeposition phenomena, possibly due to metal deposition by Ar sputtering of the anode plate. The EB source to sample distance has little impact on the plasma discharge but the use of short distances reduces electron losses to the surrounding volume and leads to a high  $\text{Si}_3\text{N}_4$  ER. After combining a suitable set of process parameters, EB controlled  $\text{Si}_3\text{N}_4$  etching without spontaneous etching has been demonstrated.

## **ACKNOWLEDGMENTS**

The authors gratefully acknowledge the financial support of this work by Carl Zeiss SMS, and additional support by US Department of Energy (DE-SC0001939). The

authors thank Dr. A. Knoll, Dr. P. Luan, A. Pranda, K.Y. Lin and A. Perruccio for helpful discussions and collaboration.

## Chapter 6: Conclusions and Future work

The main goal of this PhD thesis was to increase understanding and develop new techniques of fluorocarbon precursor based plasma etching of electronic material etchings by exploiting precursor molecule chemical structure, increased parameter space in ion-based atomic layer etching and direct injection of electron beam in a reactive gas for activation of surface etching.

In Chapter 2, we report a systematic study aimed at evaluating the impact of molecular structure parameters of hydrofluorocarbon (HFC) precursors on plasma deposition of fluorocarbon (FC) films and etching performance of a representative ultra-low-k (ULK) material, along with amorphous carbon. The  $\text{CF}_2$  fraction determines the  $\text{CF}_2$  optical emission intensity of the plasma. The  $\text{CF}_2$  optical emission, however, is not the dominant factor that determines HFC film deposition rates. Rather, HFC film deposition rates are determined by the number of weak bonds in the precursor molecule, which include a ring structure,  $\text{C}=\text{C}$ ,  $\text{C}\equiv\text{C}$ , and  $\text{C}-\text{H}$  bonds. These bonds are broken preferentially in the plasma, and/or at the surface and fragments arriving at the substrate surface presumably provide dangling bonds that efficiently bond to the substrate or other fragments. Highly polymerizing gases show decreased substrate etching rates. The FC films deposited using hydrogen-containing precursors show higher degrees of crosslinking and lower F/C ratios and exhibit a lower etch rate of substrate material. It is shown that highly polymerizing precursors with a degree of unsaturation (DU) of two enable protection of low-k sidewalls during plasma exposure from oxygen-related damage by protective film deposition. Dielectric film modifications are seen for precursors with a lower DU.

Beyond the precursor chemistry, a second way to improve the electronic materials etching fidelity and selectivity is to optimize the ion-based plasma etching process. In Chapter 3, we describe controlled etching of  $\text{Si}_3\text{N}_4$  and  $\text{SiO}_2$  layers of one to several Angstroms using this cyclic ALE approach.  $\text{Si}_3\text{N}_4$  etching and etching selectivity of  $\text{SiO}_2$  over  $\text{Si}_3\text{N}_4$  were studied and evaluated with regard to the dependence on maximum ion energy, etching step length (ESL), FC surface coverage, and precursor selection. Since  $\text{Si}_3\text{N}_4$  has a lower physical sputtering energy threshold than  $\text{SiO}_2$ ,  $\text{Si}_3\text{N}_4$  physical sputtering can take place after removal of chemical etchant at the end of each cycle for relatively high ion energies.  $\text{Si}_3\text{N}_4$  to  $\text{SiO}_2$  ALE etching selectivity was observed for these FC depleted conditions. By optimization of the ALE process parameters, e.g. low ion energies, short ESLs, and/or high FC film deposition per cycle, highly selective  $\text{SiO}_2$  to  $\text{Si}_3\text{N}_4$  etching can be achieved for FC accumulation conditions, where FC can be selectively accumulated on  $\text{Si}_3\text{N}_4$  surfaces. This highly selective etching is explained by a lower carbon consumption of  $\text{Si}_3\text{N}_4$  as compared to  $\text{SiO}_2$ . Based on the knowledge of Chapter 2, we compared  $\text{C}_4\text{F}_8$  and  $\text{CHF}_3$  in this ALE application, and it only showed a difference in etching selectivity for FC depleted conditions. For FC accumulation conditions, precursor chemistry has a weak impact on etching selectivity. Surface chemistry analysis shows that surface fluorination and FC reduction take place during a single ALE cycle for FC depleted conditions. A fluorine rich carbon layer was observed on the  $\text{Si}_3\text{N}_4$  surface after ALE processes for which FC accumulation takes place. The angle resolved (AR)-XPS thickness calculations confirmed the results of the ellipsometry measurements in all cases.

To further develop and overcome the intrinsic limitation of the ion-based plasma etching, an electron-based etching system is developed and evaluated in Chapter 4. The electron beam (EB) etching system that is based on an Ar-based direct current (DC) hollow-cathode (HC) electron beam source and electron-beam injection into the downstream reactive environment of a remote  $\text{CF}_4/\text{O}_2$  plasma. The primary electron beam energy is controlled by the extraction voltage relative to the HC discharge. For an extraction voltage greater than the ionization potential of Ar, the extracted primary electrons can produce a secondary plasma in the process chamber. We have characterized the properties of the secondary plasma and surface etching of  $\text{Si}_3\text{N}_4$  and poly-crystalline Si (poly-Si) as parameters such as the extraction voltage (0-70 V), discharge current of the HC discharge (1-2 A), pressure (2-100 mTorr), source to substrate distance (2.5 to 5 cm), and feed gas composition (with or without  $\text{CF}_4/\text{O}_2$ ) were varied. The electron energy probability function (EEPF) measured by Langmuir probe about 2.5 cm below the extraction ring suggests two major components for this situation: a primary electron beam the energy of which varies as the extraction voltage is varied and low energy electrons produced by ionization of the Ar in the chamber into which the electron beam is injected. When combining the HC Ar EB with a  $\text{CF}_4/\text{O}_2$  electron cyclotron wave resonance (ECWR) remote plasma, both the low energy plasma electron and beam electron components decreased in the EEPF. An electron-neutral synergy etching effect has been observed for  $\text{Si}_3\text{N}_4$  and poly-crystalline silicon etching. No/little remote plasma spontaneous etching was observed for the conditions used in this study, and the etching is confined to an area directly below the injected electron beam. The electron beam etched  $\text{Si}_3\text{N}_4$  surface

etching rate profile distribution is confined within a ~30 mm diameter circle, which is slightly broader than the area for which poly-Si etching is seen. The magnitude of poly-Si etching rate is also by a factor of 2x smaller than the Si<sub>3</sub>N<sub>4</sub> etching rate. A possible explanation is that increased negative surface charging for the Si<sub>3</sub>N<sub>4</sub> surface introduces additional ion bombardment of the Si<sub>3</sub>N<sub>4</sub> surface.

In Chapter 5, we further investigated this electron beam enhanced etching approach with a systematic survey of the full parameter space. Further discovered the fundamental impact of etch mechanism. The parameters studied in this chapters are precursor gas composition, extraction voltage, discharge current, pressure and source to sample distance.

Overall, this work showcases the electronic materials etching by three major components in plasma, chemistry radicals, ion, and electrons. We found that there are dramatic surface responses by emphasizing one of these three elements. Electron enhanced surface etching is the most promising technique for current semiconductor industry etching technology. Going the next steps, we would like to combine the ALE method with this electron beam enhanced etching to further reduce the chemical induced material loss/modification to the surface. Additionally, by improving the electron beam setup with a differential pumping system, could further reduce the electron beam plasma and its ion impact in surface etching. Applying new knowledge about electron beam enhanced etching to the industrial semiconductor processing could improve current and future generation etch technology.

## References

### Chapter 1:

- 1.1. G. S. Oehrlein and S. Hamaguchi, *Plasma Sources Science and Technology* **27** (2), 023001 (2018).
- 1.2. V. M. Donnelly and A. Kornblit, *Journal of Vacuum Science & Technology A* **31** (5), 050825 (2013).
- 1.3. G. S. Oehrlein, D. Metzler and C. Li, *ECS J. Solid State Sci. Technol.* **4** (6), N5041-N5053 (2015).
- 1.4. K.-Y. Lin, C. Li, S. Engelmann, R. L. Bruce, E. A. Joseph, D. Metzler and G. S. Oehrlein, *Journal of Vacuum Science & Technology A: Vacuum, Surfaces, and Films* **36** (4), 040601 (2018).
- 1.5. D. Metzler, R. L. Bruce, S. Engelmann, E. A. Joseph and G. S. Oehrlein, *Journal of Vacuum Science & Technology A* **32** (2), 020603 (2014).
- 1.6. E. Vogli, D. Metzler and G. S. Oehrlein, *Applied Physics Letters* **102** (25), 253105 (2013).
- 1.7. K. J. Kanarik, T. Lill, E. A. Hudson, S. Sriraman, S. Tan, J. Marks, V. Vahedi and R. A. Gottscho, *Journal of Vacuum Science & Technology A* **33** (2), 020802 (2015).
- 1.8. D. Metzler, C. Li, C. S. Lai, E. A. Hudson and G. S. Oehrlein, *J. Phys. D: Appl. Phys* **50** (254006), 254006 (2017).
- 1.9. M. Kawakami, D. Metzler, C. Li and G. S. Oehrlein, *Journal of Vacuum Science & Technology A: Vacuum, Surfaces, and Films* **34** (4), 040603 (2016).
- 1.10. G. S. Oehrlein, *Materials Science and Engineering B-Solid State Materials for Advanced Technology* **4** (1-4), 441-450 (1989).

- 1.11. D. J. Mazey, R. S. Nelson and R. S. Barnes, *The Philosophical Magazine: A Journal of Theoretical Experimental and Applied Physics* **17** (150), 1145-1161 (1968).
- 1.12. A. Pranda, S. A. Gutierrez Razo, J. T. Fourkas and G. S. Oehrlein, *Plasma Processes and Polymers* **0** (0), e1900026.
- 1.13. D. Metzler, R. L. Bruce, S. Engelmann, E. A. Joseph and G. S. Oehrlein, *Journal of Vacuum Science & Technology A* **32** (2), 020603 (2014).
- 1.14. J. W. Coburn and H. F. Winters, *Journal of Applied Physics* **50** (5), 3189-3196 (1979).
- 1.15. V. Burdovitsin and E. Oks, *Review of Scientific Instruments* **70** (7), 2975-2978 (1999).
- 1.16. L. Ling, X. Hua, L. Zheng, G. Oehrlein, E. Hudson and P. Jiang, *Journal of Vacuum Science & Technology B: Microelectronics and Nanometer Structures Processing, Measurement, and Phenomena* **26** (1), 11-22 (2008).
- 1.17. R. Hippler, J. Kredl and V. Vartolomei, *Vacuum* **83** (4), 732-737 (2008).
- 1.18. V. M. Donnelly, *Journal of Vacuum Science & Technology a-Vacuum Surfaces and Films* **14** (3), 1076-1087 (1996).
- 1.19. V. Godyak and V. Demidov, *Journal of Physics D: Applied Physics* **44** (23), 233001 (2011).

## Chapter 2:

- 2.1 M. Schaepkens and G. S. Oehrlein, *J. Electrochem. Soc.* 148, C211 (2001).
- 2.2 G. S. Oehrlein, D. Metzler and C. Li, *ECS J. Solid State Sci. Technol.* 4, N5041 (2015).
- 2.3 D. Metzler, R. L. Bruce, S. Engelmann, E. A. Joseph and G. S. Oehrlein, *J. Vac. Sci. Technol. A* 32, 020603 (2014).
- 2.4 M. S. Kuo, X. F. Hua, G. S. Oehrlein, A. Ali, P. Jiang, P. Lazzeri and M. Anderle, *J. Vac. Sci. Technol. B* 28, 284 (2010).
- 2.5 D. L. Keil, B. A. Helmer and S. Lassig, *J. Vac. Sci. Technol. B* 21, 1969 (2003).
- 2.6 N. Posseme, T. Chevolleau, O. Joubert and L. Vallier, *J. Vac. Sci. Technol. B* 21, 2432 (2003).
- 2.7 M. Sekine, *Appl. Surf. Sci.* 192, 270 (2002).
- 2.8 D. Metzler, K. Uppireddi, R. L. Bruce, H. Miyazoe, Y. Zhu, W. Price, E. S. Sikorski, C. Li, S. U. Engelmann, E. A. Joseph and G. S. Oehrlein, *J. Vac. Sci. Technol. A* 34, 01B102 (2016).
- 2.9 X. Li, X. F. Hua, L. Ling, G. S. Oehrlein, M. Barela and H. M. Anderson, *J. Vac. Sci. Technol. A* 20, 2052 (2002).
- 2.10 K. Takahashi, A. Itoh, T. Nakamura and K. Tachibana, *Thin Solid Films* 374, 303 (2000).
- 2.11 Y. Miyawaki, E. Shibata, Y. Kondo, K. Takeda, H. Kondo, K. Ishikawa, H. Okamoto, M. Sekine and M. Hori, *Jpn. J. Appl. Phys.* 52, 020204 (2013).
- 2.12 Y. Miyawaki, Y. Kondo, M. Sekine, K. Ishikawa, T. Hayashi, K. Takeda, H. Kondo, A. Yamazaki, A. Ito, H. Matsumoto and M. Hori, *Jpn. J. Appl. Phys.* 52, 016201 (2013).
- 2.13 M. F. Cuddy and E. R. Fisher, *ACS Appl. Mater. Interfaces* 4, 1733 (2012).

- 2.14 S. Y. Kang, I. Sawada, Y. Kondo and P. L. G. Ventzek, *Jpn. J. Appl. Phys.* 47, 6843 (2008).
- 2.15 S. U. Engelmann, R. L. Bruce, M. Nakamura, D. Metzler, S. G. Walton and E. A. Joseph, *ECS J. Solid State Sci. Technol.* 4, N5054 (2015).
- 2.16 D. Metzler, C. Li, S. Engelmann, R. L. Bruce, E. A. Joseph and G. S. Oehrlein, *J. Vac. Sci. Technol. A* 34, 01B101 (2016).
- 2.17 S. U. Engelmann, N. P. Marchack and M. Nakamura, U.S. Patent No. 9214355 B2 (15 December 2005).
- 2.18 I. T. Martin and E. R. Fisher, *J. Vac. Sci. Technol. A* 22, 2168 (2004).
- 2.19 G. Cunge and J. P. Booth, *J. Appl. Phys.* 85, 3952 (1999).
- 2.20 A. D. Tserepi, J. Derouard, J. P. Booth and N. Sadeghi, *J. Appl. Phys.* 81, 2124 (1997).
- 2.21 G. Cunge, P. Chabert and J. P. Booth, *J. Appl. Phys.* 89, 7750 (2001).
- 2.22 T. Standaert, C. Hedlund, E. A. Joseph, G. S. Oehrlein and T. J. Dalton, *J. Vac. Sci. Technol. A* 22, 53 (2004).
- 2.23 K. Miyata, M. Hori and T. Goto, *J. Vac. Sci. Technol. A* 14, 2343 (1996).
- 2.24 W. W. Stoffels, E. Stoffels and K. Tachibana, *J. Vac. Sci. Technol. A* 16, 87 (1998).
- 2.25 S. Jain, V. Zubkov, T. Nowak, A. Demos and J. Rocha, *Solid State Technol.* 48, 43 (2005).
- 2.26 P. Lazzeri, X. Hua, G. S. Oehrlein, M. Barozzi, E. Iacob and M. Anderle, *J. Vac. Sci. Technol. B* 23, 1491 (2005).
- 2.27 P. Lazzeri, G. J. Stueber, G. S. Oehrlein, R. McGowan and E. Busch, *J. Vac. Sci. Technol. B* 24, 2695 (2006).
- 2.28 L. Zheng, L. Ling, X. F. Hua, G. S. Oehrlein and E. A. Hudson, *J. Vac. Sci. Technol. A* 23, 634 (2005).
- 2.29 M. S. Kuo and G. S. Oehrlein, *J. Vac. Sci. Technol. B* 28, 1104 (2010).

- 2.30 Ch. Cardinaud, A. Rhounna, G. Turban and B. Grolleau, *Rev. Phys. Appl.* 24, 309 (1989).
- 2.31 L. Reto, D. G. Michael, M. O. René, W. Lothar, S. Holger, H. Sabine and D. R. Buddy, *Fluorinated Surfaces, Coatings, and Films*, edited by D. G. Castner and D. W. Grainger (American Chemical Society, 2001), Vol. 787, pp. 187-202.
- 2.32 Z. Da and M. J. Kushner, *J. Vac. Sci. Technol. A* 18, 2661 (2000).
- 2.33 J. H. Min, S. W. Hwang, G. R. Lee and S. H. Moon, *J. Vac. Sci. Technol. B* 21, 1210 (2003).
- 2.34 M. F. Cuddy and E. R. Fisher, *J. Appl. Phys.* 108, 033303 (2010).
- 2.35 J. W. Moore, C. L. Stanitski, P. C. Jurs, *Principles of Chemistry: The Molecular Science*, (Brooks/Cole, Cengage Learning, 2009), pp. 321-325
- 2.36 M. Schaepkens, T. Standaert, N. R. Rueger, P. G. M. Sebel, G. S. Oehrlein and J. M. Cook, *J. Vac. Sci. Technol. A* 17, 26 (1999).
- 2.37 Ch. Cardinaud and G. Turban, *Appl. Surf. Sci.* 45, 109 (1990).
- 2.38 F. Gaboriau, M.-C. Fernandez-Peignon, G. Cartry and Ch. Cardinaud, *J. Vac. Sci. Technol. A* 23, 226 (2005).
- 2.39 T. Ito, K. Karahashi, M. Fukasawa, T. Tatsumi and S. Hamaguchi, *J. Vac. Sci. Technol. A* 29, 050601 (2011).
- 2.40 X. Li, L. Ling, X. F. Hua, M. Fukasawa, G. S. Oehrlein, M. Barela and H. M. Anderson, *J. Vac. Sci. Technol. A* 21, 284 (2003).
- 2.41 L. Ling, X. Hua, L. Zheng, G. S. Oehrlein, E. A. Hudson and P. Jiang, *J. Vac. Sci. Technol. B* 26, 11 (2008).
- 2.42 J. Bao, H. Shi, H. Huang, P. S. Ho, M. L. McSwiney, M. D. Goodner, M. Moinpour and G. M. Kloster, *J. Vac. Sci. Technol. A* 28, 207 (2010).
- 2.43 M. A. Goldman, D. B. Graves, G. A. Antonelli, S. P. Behera and J. A. Kelber, *J. Appl. Phys.* 106, 013311 (2009).

2.44 P. Atkins and L. Jones, *Chemistry: Molecules, Matter, and Change*, Third Edition (W. H. Freeman and Company, New York, 1997), pp. 318

### Chapter 3:

- 3.1 M. Jeong, B. Doris, J. Kedzierski, K. Rim and M. Yang, *Science* 306, 2057 (2004).
- 3.2 Y. Fu-Liang, L. Di-Hong, C. Hou-Yu, C. Chang-Yun, L. Sheng-Da, H. Cheng-Chuan, C. Tang-Xuan, C. Hung-Wei, H. Chien-Chao, L. Yi-Hsuan, W. Chung-Cheng, C. Chi-Chun, C. Shih-Chang, C. Ying-Tsung, C. Ying-Ho, C. Chih-Jian, C. Bor-Wen, H. Peng-Fu, S. Jyu-Horng, T. Han-Jan, Y. Yee-Chia, L. Yiming, L. Jam-Wem, C. Pu, L. Mong-Song and H. Chenming, *Symposium on VLSI Technology Digest of Technical Papers*, 196 (2004)
- 3.3 M. M. M. M. Waldrop, *Nature* 530, 144 (2016).
- 3.4 T. Suntola and J. Antson, U.S. patent No. 4,058,430A (14 November 1977).
- 3.5 S. M. George, *Chem. Rev.* 110, 111 (2010).
- 3.6 S. E. Potts and W. M. M. Kessels, *Coordin. Chem. Rev.* 257, 3254 (2013).
- 3.7 R. L. Puurunen, *J. Appl. Phys.* 97, 121301 (2005).
- 3.8 M. Leskelä and M. Ritala, *Thin Solid Films* 409, 138 (2002).
- 3.9 G. S. Oehrlein, D. Metzler and C. Li, *ECS J. Solid State Sci. and Technol.* 4, N5041 (2015).
- 3.10 S. U. Engelmann, R. L. Bruce, M. Nakamura, D. Metzler, S. G. Walton and E. A. Joseph, *ECS J. Solid State Sci. and Technol.* 4, N5054 (2015).
- 3.11 K. J. Kanarik, T. Lill, E. A. Hudson, S. Sriraman, S. Tan, J. Marks, V. Vahedi and R. A. Gottscho, *J. Vac. Sci. Technol. A* 33, 020802 (2015).
- 3.12 S. Rauf, T. Sparks, P. L. G. Ventzek, V. V. Smirnov, A. V. Stengach, K. G. Gaynullin and V. A. Pavlovsky, *J. Appl. Phys.* 101, 033308 (2007).
- 3.13 A. Agarwal and M. J. Kushner, *J. Vac. Sci. Technol. A* 27, 37 (2009).
- 3.14 D. Metzler, G. S. Oehrlein, R. L. Bruce, S. Engelmann and E. A. Joseph, *AVS 60th International Symposium & Exhibition* (2013), available at [http://www2.avs.org/symposium2013/Papers/Paper\\_PS-WeM1.html](http://www2.avs.org/symposium2013/Papers/Paper_PS-WeM1.html)

- 3.15 D. Metzler, R. L. Bruce, S. Engelmann, E. A. Joseph and G. S. Oehrlein, J. Vac. Sci. Technol. A 32, 020603 (2014).
- 3.16 D. Metzler, C. Li, S. Engelmann, R. L. Bruce, E. A. Joseph and G. S. Oehrlein, J. Vac. Sci. Technol. A 34, 01B101 (2016).
- 3.17 D. Metzler, K. Uppireddi, R. L. Bruce, H. Miyazoe, Y. Zhu, W. Price, E. S. Sikorski, C. Li, S. U. Engelmann, E. A. Joseph and G. S. Oehrlein, J. Vac. Sci. Technol. A 34, 01B102 (2016).
- 3.18 M. Kawakami, D. Metzler, C. Li, G. S. Oehrlein J. Vac. Sci. Technol. A 34, 031306 (2016)
- 3.19 M. Schaepekens, T. Standaert, N. R. Rueger, P. G. M. Sebel, G. S. Oehrlein and J. M. Cook, J. Vac. Sci. Technol. A 17, 26 (1999).
- 3.20 B. E. E. Kastenmeier, P. J. Matsuo and G. S. Oehrlein, J. Vac. Sci. Technol. A 17, 3179 (1999).
- 3.21 X. Li, L. Ling, X. F. Hua, G. S. Oehrlein, Y. C. Wang and H. M. Anderson, J. Vac. Sci. Technol. A 21, 1955 (2003).
- 3.22 A. P. Prskalo, S. Schmauder, C. Ziebert, J. Ye and S. Ulrich, Surf. Coat. Tech. 204, 2081 (2010).
- 3.23 E. Hudson, V. Vidyarthi, R. Bhowmick, R. Bise, H. J. Shin, G. Delgadino, B. Jariwala, D. Lambert and S. Deshmukh, AVS 61st International Symposium & Exhibition (2014), available at [http://www2.avs.org/symposium2014/Papers/Paper\\_PS2+TF-ThM2.html](http://www2.avs.org/symposium2014/Papers/Paper_PS2+TF-ThM2.html).
- 3.24 C. Li, R. Gupta, V. Pallem, G. S. Oehrlein, J. Vac. Sci. Technol. A 34, 031306 (2016)
- 3.25 D. Metzler, S. U. Engelmann, R. L. Bruce, E. A. Joseph, V. A. Godyak and G. S. Oehrlein, AVS 61st International Symposium & Exhibition (2014) available at [http://www2.avs.org/symposium2014/Papers/Paper\\_PS2+TF-ThM1.html](http://www2.avs.org/symposium2014/Papers/Paper_PS2+TF-ThM1.html).

- 3.26 M. J. Barela, H. M. Anderson and G. S. Oehrlein, *J. Vac. Sci. Technol. A* 23, 408 (2005).
- 3.27 X. Li, X. F. Hua, L. Ling, G. S. Oehrlein, M. Barela and H. M. Anderson, *J. Vac. Sci. Technol. A* 20, 2052 (2002).
- 3.28 M. Schaepkens, N. R. Rueger, J. J. Beulens, X. Li, T. Standaert, P. J. Matsuo and G. S. Oehrlein, *J. Vac. Sci. Technol. A* 17, 3272 (1999).
- 3.29 C. D. Wagner, L. E. Davis, M. V. Zeller, J. A. Taylor, R. H. Raymond and L. H. Gale, *Surf. Interface Anal.* 3, 211 (1981).
- 3.30 S. W. Robey and G. S. Oehrlein, *Surf. Sci.* 210, 429 (1989).
- 3.31 D. T. Clark, W. J. Feast, P. J. Tweedale and H. R. Thomas, *J. Polym. Sci. Pol. Chem.* 18, 1651 (1980).
- 3.32 K. Ninomiya, K. Suzuki, S. Nishimatsu and O. Okada, *J. Appl. Phys.* 58, 1177 (1985).
- 3.33 N. Posseme, T. Chevolleau, O. Joubert and L. Vallier, *J. Vac. Sci. Technol. B* 21, 2432 (2003).
- 3.34 J. L. Vossen, J. H. Thomas, J. S. Maa, O. R. Mesker and G. O. Fowler, *J. Vac. Sci. Technol. A* 1, 1452 (1983).
- 3.35 N. R. Rueger, J. J. Beulens, M. Schaepkens, M. F. Doemling, J. M. Mirza, T. Standaert and G. S. Oehrlein, *J. Vac. Sci. Technol. A* 15, 1881 (1997).
- 3.36 NIST Electron Inelastic-Mean-Free-Path Database Version 1.2, available at <http://www.nist.gov/srd/nist71.cfm>.

#### Chapter 4:

- 4.1. M. Jeong, B. Doris, J. Kedzierski, K. Rim and M. Yang, *Science* 306 (5704), 2057-2060 (2004).
- 4.2. Y. Fu-Liang, L. Di-Hong, C. Hou-Yu, C. Chang-Yun, L. Sheng-Da, H. Cheng-Chuan, C. Tang-Xuan, C. Hung-Wei, H. Chien-Chao, L. Yi-Hsuan, W. Chung-Cheng, C. Chi-Chun, C. Shih-Chang, C. Ying-Tsung, C. Ying-Ho, C. Chih-Jian, C. Bor-Wen, H. Peng-Fu, S. Jyu-Horng, T. Han-Jan, Y. Yee-Chia, L. Yiming, L. Jam-Wem, C. Pu, L. Mong-Song and H. Chenming, presented at the VLSI Technology, 2004. Digest of Technical Papers. 2004 Symposium on, 2004 (unpublished).
- 4.3. M. M. M. M. Waldrop, *Nature* 530 (7589), 144-147 (2016).
- 4.4. G. E. Moore, *Proceedings of the IEEE* 86 (1), 82-85 (1998).
- 4.5. J. Comas and C. B. Cooper, *Journal of Applied Physics* 37 (7), 2820-2822 (1966).
- 4.6. C. Li, R. Gupta, V. Pallem and G. S. Oehrlein, *Journal of Vacuum Science & Technology A: Vacuum, Surfaces, and Films* 34 (3), 031306 (2016).
- 4.7. J. W. Coburn and H. F. Winters, *Journal of Applied Physics* 50 (5), 3189-3196 (1979).
- 4.8. G. S. Oehrlein, D. Metzler and C. Li, *Ecs Journal of Solid State Science and Technology* 4 (6), N5041-N5053 (2015).
- 4.9. D. Metzler, R. L. Bruce, S. Engelmann, E. A. Joseph and G. S. Oehrlein, *Journal of Vacuum Science & Technology A* 32 (2), 020603 (2014).
- 4.10. D. Metzler, K. Uppireddi, R. L. Bruce, H. Miyazoe, Y. Zhu, W. Price, E. S. Sikorski, C. Li, S. U. Engelmann, E. A. Joseph and G. S. Oehrlein, *Journal of Vacuum Science & Technology A* 34 (1), 01B102 (2016).
- 4.11. C. Li, D. Metzler, C. S. Lai, E. A. Hudson and G. S. Oehrlein, *Journal of Vacuum Science & Technology A: Vacuum, Surfaces, and Films* 34 (4), 041307 (2016).

- 4.12. K.-Y. Lin, C. Li, S. Engelmann, R. L. Bruce, E. A. Joseph, D. Metzler and G. S. Oehrlein, *Journal of Vacuum Science & Technology A* 36 (4), 040601 (2018).
- 4.13. D. Metzler, C. Li, S. Engelmann, R. L. Bruce, E. A. Joseph and G. S. Oehrlein, *The Journal of Chemical Physics* 146 (5), 052801 (2017).
- 4.14. D. Metzler, C. Li, S. Engelmann, R. L. Bruce, E. A. Joseph and G. S. Oehrlein, *Journal of Vacuum Science & Technology A* 34 (1), 01B101 (2016).
- 4.15. D. Metzler, C. Li, C. S. Lai, E. A. Hudson and G. S. Oehrlein, *J. Phys. D: Appl. Phys* 50 (254006), 254006 (2017).
- 4.16. M. Kawakami, D. Metzler, C. Li and G. S. Oehrlein, *Journal of Vacuum Science & Technology A: Vacuum, Surfaces, and Films* 34 (4), 040603 (2016).
- 4.17. D. J. Mazey, R. S. Nelson and R. S. Barnes, *The Philosophical Magazine: A Journal of Theoretical Experimental and Applied Physics* 17 (150), 1145-1161 (1968).
- 4.18. A. Pranda, S. A. Gutierrez Razo, J. T. Fourkas and G. S. Oehrlein, *Plasma Processes and Polymers* 0 (0), e1900026.
- 4.19. L. Dorf, J. C. Wang, S. Rauf, G. A. Monroy and Y. Zhang, *Journal of Physics D: Applied Physics* 50 (27) (2017).
- 4.20. D. R. Boris, T. B. Petrova, G. M. Petrov and S. G. Walton, *Journal of Vacuum Science & Technology A* 35 (1), 01A104 (2017).
- 4.21. S. J. Randolph, J. D. Fowlkes and P. D. Rack, *Critical Reviews in Solid State and Materials Sciences* 31 (3), 55-89 (2006).
- 4.22. S. J. Randolph, J. D. Fowlkes and P. D. Rack, *Journal of Applied Physics* 98 (3), 034902 (2005).
- 4.23. S. Matsui and K. Mori, *Applied Physics Letters* 51 (19), 1498-1499 (1987).

- 4.24. M. T. Domonkos, *Evaluation of low-current orificed hollow cathodes*. (University of Michigan, 1999).
- 4.25. V. Burdovitsin, A. Kazakov, A. Medovnik and E. Oks, AIP Conference Proceedings 1772 (1), 040001 (2016).
- 4.26. A. Tyunkov, Y. Yushkov, D. Zolotukhin and E. Oks, AIP Conference Proceedings 1772 (1), 040002 (2016).
- 4.27. V. Burdovitsin, Y. Burachevsky, E. Oks and M. Fedorov, AIP Conference Proceedings 669 (1), 358-360 (2003).
- 4.28. S. Muhl and A. Pérez, Thin Solid Films 579, 174-198 (2015).
- 4.29. J. Xu, X. Tian, C. Gong, C. Li and C. Yang, Vacuum 134, 83-87 (2016).
- 4.30. J. Xu, X. Tian, C. Gong, C. Li, M. Wu, J. Wang and T. Ma, Vacuum 143, 407-411 (2017).
- 4.31. V. Burdovitsin and E. Oks, Review of Scientific Instruments 70 (7), 2975-2978 (1999).
- 4.32. E. M. Oks and P. M. Schanin, Physics of Plasmas 6 (5), 1649-1654 (1999).
- 4.33. S. Gershman and Y. Raitses, Journal of Physics D: Applied Physics 51 (23), 235202 (2018).
- 4.34. D. R. Boris and S. G. Walton, Journal of Vacuum Science & Technology A 36 (6), 060601 (2018).
- 4.35. S. G. Walton, D. R. Boris, S. C. Hernández, E. H. Lock, T. B. Petrova, G. M. Petrov and R. F. Fernsler, ECS Journal of Solid State Science and Technology 4 (6), N5033-N5040 (2015).
- 4.36. S. G. Walton, D. R. Boris, S. C. Hernández, E. H. Lock, T. B. Petrova, G. M. Petrov, A. V. Jagtiani, S. U. Engelmann, H. Miyazoe and E. A. Joseph, Microelectronic Engineering 168, 89-96 (2017).
- 4.37. D. R. Boris, R. F. Fernsler and S. G. Walton, Plasma Sources Science and Technology 24 (2), 025032 (2015).

- 4.38. R. Shahid, B. Ajit, A. Ankur, D. Leonid, C. Kenneth, R. B. David and G. W. Scott, *Plasma Sources Science and Technology* 26 (6), 065006 (2017).
- 4.39. R. Shahid, D. Leonid and C. Kenneth, *Plasma Sources Science and Technology* 27 (7), 075004 (2018).
- 4.40. L. Dorf, J.-C. Wang, S. Rauf, Y. Zhang, A. Agarwal, J. Kenney, K. Ramaswamy and K. Collins, presented at the SPIE Advanced Lithography, 2016 (unpublished).
- 4.41. R. Hippler, J. Kredl and V. Vartolomei, *Vacuum* 83 (4), 732-737 (2008).
- 4.42. B. E. E. Kastenmeier, P. J. Matsuo, J. J. Beulens and G. S. Oehrlein, *Journal of Vacuum Science & Technology A* 14 (5), 2802-2813 (1996).
- 4.43. G. S. Oehrlein, P. J. Matsuo, M. F. Doemling, N. R. Rueger, B. E. E. Kastenmeier, M. Schaepkens, T. Standaert and J. J. Beulens, *Plasma Sources Science & Technology* 5 (2), 193-199 (1996).
- 4.44. P. J. Matsuo, B. E. E. Kastenmeier, J. J. Beulens and G. S. Oehrlein, *J. Vac. Sci. Technol. A-Vac. Surf. Films* 15 (4), 1801-1813 (1997).
- 4.45. V. A. Godyak, *IEEE Transactions on Plasma Science* 34 (3), 755-766 (2006).
- 4.46. V. A. Godyak and V. I. Demidov, *Journal of Physics D: Applied Physics* 44 (23), 233001 (2011).
- 4.47. V. A. Godyak, R. B. Piejak and B. M. Alexandrovich, *Plasma Sources Science and Technology* 1 (1), 36 (1992).
- 4.48. E. H. Lock, R. F. Fernsler and S. G. Walton, *Plasma Sources Science and Technology* 17 (2), 025009 (2008).
- 4.49. B. F. Kraus and Y. Raitses, *Physics of Plasmas* 25 (3), 030701 (2018).
- 4.50. B. E. E. Kastenmeier, P. J. Matsuo, G. S. Oehrlein, R. E. Ellefson and L. C. Frees, *J. Vac. Sci. Technol. A-Vac. Surf. Films* 19 (1), 25-30 (2001).
- 4.51. B. E. E. Kastenmeier, P. J. Matsuo and G. S. Oehrlein, *J. Vac. Sci. Technol. A-Vac. Surf. Films* 17 (6), 3179-3184 (1999).

## Chapter 5

5. 1. M. Jeong, B. Doris, J. Kedzierski, K. Rim and M. Yang, *Science* 306 (5704), 2057-2060 (2004).
5. 2. Y. Fu-Liang, L. Di-Hong, C. Hou-Yu, C. Chang-Yun, L. Sheng-Da, H. Cheng-Chuan, C. Tang-Xuan, C. Hung-Wei, H. Chien-Chao, L. Yi-Hsuan, W. Chung-Cheng, C. Chi-Chun, C. Shih-Chang, C. Ying-Tsung, C. Ying-Ho, C. Chih-Jian, C. Bor-Wen, H. Peng-Fu, S. Jyu-Horng, T. Han-Jan, Y. Yee-Chia, L. Yiming, L. Jam-Wem, C. Pu, L. Mong-Song and H. Chenming, presented at the VLSI Technology, 2004. Digest of Technical Papers. 2004 Symposium on, 2004 (unpublished).
5. 3. M. M. M. M. Waldrop, *Nature* 530 (7589), 144-147 (2016).
5. 4. G. E. Moore, *Proceedings of the IEEE* 86 (1), 82-85 (1998).
5. 5. J. Comas and C. B. Cooper, *Journal of Applied Physics* 37 (7), 2820-2822 (1966).
5. 6. D. Metzler, C. Li, C. S. Lai, E. A. Hudson and G. S. Oehrlein, *J. Phys. D: Appl. Phys* 50 (254006), 254006 (2017).
5. 7. D. Metzler, C. Li, S. Engelmann, R. L. Bruce, E. A. Joseph and G. S. Oehrlein, *Journal of Vacuum Science & Technology A* 34 (1), 01B101 (2016).
5. 8. D. Metzler, K. Uppireddi, R. L. Bruce, H. Miyazoe, Y. Zhu, W. Price, E. S. Sikorski, C. Li, S. U. Engelmann, E. A. Joseph and G. S. Oehrlein, *Journal of Vacuum Science & Technology A* 34 (1), 01B102 (2016).
5. 9. C. Li, D. Metzler, C. S. Lai, E. A. Hudson and G. S. Oehrlein, *Journal of Vacuum Science & Technology A: Vacuum, Surfaces, and Films* 34 (4), 041307 (2016).
5. 10. M. Kawakami, D. Metzler, C. Li and G. S. Oehrlein, *Journal of Vacuum Science & Technology A: Vacuum, Surfaces, and Films* 34 (4), 040603 (2016).

5. 11. G. S. Oehrlein, D. Metzler and C. Li, Ecs Journal of Solid State Science and Technology 4 (6), N5041-N5053 (2015).
5. 12. C. Li, R. Gupta, V. Pallem and G. S. Oehrlein, Journal of Vacuum Science & Technology A: Vacuum, Surfaces, and Films 34 (3), 031306 (2016).
5. 13. J. W. Coburn and H. F. Winters, Journal of Applied Physics 50 (5), 3189-3196 (1979).
5. 14. K.-Y. Lin, C. Li, S. Engelmann, R. L. Bruce, E. A. Joseph, D. Metzler and G. S. Oehrlein, Journal of Vacuum Science & Technology A 36 (4), 040601 (2018).
5. 15. D. Metzler, C. Li, S. Engelmann, R. L. Bruce, E. A. Joseph and G. S. Oehrlein, The Journal of Chemical Physics 146 (5), 052801 (2017).
5. 16. R. Hippler, J. Kredl and V. Vartolomei, Vacuum 83 (4), 732-737 (2008).
5. 17. B. E. E. Kastenmeier, P. J. Matsuo, J. J. Beulens and G. S. Oehrlein, Journal of Vacuum Science & Technology A 14 (5), 2802-2813 (1996).
5. 18. G. S. Oehrlein, P. J. Matsuo, M. F. Doemling, N. R. Rueger, B. E. E. Kastenmeier, M. Schaepkens, T. Standaert and J. J. Beulens, Plasma Sources Science & Technology 5 (2), 193-199 (1996).
5. 19. P. J. Matsuo, B. E. E. Kastenmeier, J. J. Beulens and G. S. Oehrlein, J. Vac. Sci. Technol. A-Vac. Surf. Films 15 (4), 1801-1813 (1997).
5. 20. M. T. Domonkos, *Evaluation of low-current orificed hollow cathodes*. (University of Michigan, 1999).
5. 21. V. Burdovitsin, A. Kazakov, A. Medovnik and E. Oks, AIP Conference Proceedings 1772 (1), 040001 (2016).
5. 22. A. Tyunkov, Y. Yushkov, D. Zolotukhin and E. Oks, AIP Conference Proceedings 1772 (1), 040002 (2016).
5. 23. V. Burdovitsin, Y. Burachevsky, E. Oks and M. Fedorov, AIP Conference Proceedings 669 (1), 358-360 (2003).

5. 24. S. Muhl and A. Pérez, *Thin Solid Films* 579, 174-198 (2015).
5. 25. J. Xu, X. Tian, C. Gong, C. Li and C. Yang, *Vacuum* 134, 83-87 (2016).
5. 26. J. Xu, X. Tian, C. Gong, C. Li, M. Wu, J. Wang and T. Ma, *Vacuum* 143, 407-411 (2017).
5. 27. V. Burdovitsin and E. Oks, *Review of Scientific Instruments* 70 (7), 2975-2978 (1999).
5. 28. E. M. Oks and P. M. Schanin, *Physics of Plasmas* 6 (5), 1649-1654 (1999).
5. 29. V. A. Godyak, *IEEE Transactions on Plasma Science* 34 (3), 755-766 (2006).
5. 30. V. A. Godyak and V. I. Demidov, *Journal of Physics D: Applied Physics* 44 (23), 233001 (2011).
5. 31. V. A. Godyak, R. B. Piejak and B. M. Alexandrovich, *Plasma Sources Science and Technology* 1 (1), 36 (1992).
5. 32. N. R. Rueger, J. J. Beulens, M. Schaepkens, M. F. Doemling, J. M. Mirza, T. Standaert and G. S. Oehrlein, *J. Vac. Sci. Technol. A-Vac. Surf. Films* 15 (4), 1881-1889 (1997).
5. 33. S. J. Randolph, J. D. Fowlkes and P. D. Rack, *Journal of Applied Physics* 98 (3), 034902 (2005).